

Parton Dynamics in Forward Jet Events from Positron-Proton Collisions at HERA

Thesis submitted for the degree of
Candidatus Scientiarum in Physics

by

Rasmus Mackeprang



November 24, 2003

Experimental High Energy Physics Group
Niels Bohr Institute
University of Copenhagen

Contents

1	Introduction	2
I	Theory	5
2	Quantum Chromo Dynamics	6
2.1	The Quark Model	6
2.2	Non-Abelian Yang-Mills Theory	7
2.3	The Classical Lagrangian of Quantum Chromo Dynamics	8
2.3.1	Feynman Rules	10
2.4	Renormalisation and Asymptotic Freedom	12
2.4.1	Running of the Coupling Constant	12
3	Theory of Deep Inelastic Scattering	15
3.1	Kinematics of Deep Inelastic Scattering	15
3.1.1	Reconstruction of Kinematic Variables	17
3.1.2	Frames of Reference	18
3.1.3	Coordinates	20
3.2	The Elastic QED Cross Section	20
3.3	The Inelastic Cross Section to Lowest Order	22
3.3.1	Proton Structure in the Quark Parton Model	22
3.4	DIS to First Order in α_s	25
4	DIS Processes and QCD Evolution Schemes	29
4.1	DGLAP	30
4.2	BFKL	32
4.3	CCFM	32
4.4	CCFM vs. BFKL	34

4.5	The Colour Dipole Model (CDM)	34
5	Monte Carlo Event Generation	37
5.1	RAPGAP	37
5.2	CASCADE	39
5.3	ARIADNE	39
6	Jet Physics	41
6.1	Colour Confinement and the Jet Phenomenon	41
6.2	The Lund String Model	42
6.3	Finding Jets	43
6.4	Choice of Jet-Algorithm	44
6.5	The Inclusive k_t -Algorithm	45
II	The Experimental Facility	49
7	The HERA Collider	50
7.1	The Colliding Beams	50
7.2	Experiments at HERA	51
8	The H1 Experiment	52
8.1	General Design Considerations	53
8.2	Tracking	53
8.2.1	The Central and Backward Silicon Trackers (CST & BST)	55
8.2.2	The Central Jet Chambers (CJC 1 + 2)	57
8.2.3	Z-Chambers (CIZ,COZ)	58
8.2.4	The Backward Drift Chamber (BDC)	58
8.2.5	The Forward Tracking Detector (FTD)	59
8.3	Calorimetry	60
8.3.1	The Liquid Argon Calorimeter (LAr)	60
8.3.2	The Spaghetti Calorimeter (SpaCal)	61
8.4	The Luminosity System	62
8.5	The Time-of-Flight System (ToF)	62
8.6	The Trigger System	62

III	Forward Jet Analysis	65
9	Event Selection and Corrections	66
9.1	Forward Jets and Resummation Schemes	66
9.2	The Need for an Event Selection	67
9.3	Run Selection and Triggers	68
9.4	Detector Cuts	68
9.4.1	Positron Cuts	68
9.4.2	Vertex Cut	70
9.4.3	Final State Object $\sum(E - p_z)$	72
9.5	Kinematic DIS Selection	72
9.6	Forward Jet Selection	73
9.7	Evaluating the Forward Jet Event Selection	76
9.8	Correcting for Detector Effects and QED Radiation	80
9.8.1	Detector Corrections	80
9.8.2	Radiative Corrections	81
9.8.3	Unfolding the Corrections	82
10	The Forward Jet Cross Section Measurement	84
10.1	Detector Level Distributions	84
10.2	Detector Corrections	86
10.3	Treatment of Systematic Errors	86
10.4	The Corrected Differential Cross Section	87
11	Discerning Models Through Event Variables	89
11.1	Transverse Energy Flow	90
11.1.1	Detector Level	90
11.1.2	Corrections	92
11.1.3	Systematics	92
11.1.4	Results	93
11.2	Jet-Profiles	97
11.2.1	Detector Level Jet-Profiles	98
11.2.2	Corrections	99
11.2.3	Treatment of Systematics	99
11.2.4	Comparison to Monte Carlo	101

11.3 The p_t -Spectrum	103
11.3.1 Detector Level Spectrum	103
11.3.2 Corrections	103
11.3.3 Systematics	105
11.3.4 Results	105
12 Conclusions and Outlook	107
12.1 Observations	107
12.2 What Was Learned	108
12.3 Outlook	108
13 Acknowledgements	110
Bibliography	111
Appendix	117
A Some Notes on Representations and Structure Coefficients	117
A.1 Fundamental Concepts	117
A.2 Lie Algebras	117
A.3 Representations of $SU(N)$	118
A.4 $SU(3)$	119

List of Figures

1.1	A parton cascade in DIS	3
2.1	The Feynman rules for QCD	11
2.2	QED charge screening vs properties of QCD	13
3.1	A diagram representing DIS	16
3.2	Definition of the polar angle in H1	18
3.3	Photon-quark collision in the Breit frame	19
3.4	Elastic e-p scattering	21
3.5	Measurements of F_2 from SLAC-MIT, BCDMCS, H1 and ZEUS	23
3.6	Possible forms of F_2	24
3.7	Lowest order DIS-processes	26
4.1	Gluon cascade	31
4.2	CDM-figure	35
4.3	Dipole types in the Colour Dipole Model	35
4.4	Phase space for DIS in CDM	36
5.1	Parton evolutions	38
5.2	QCD radiation in CDM as implemented in ARIADNE	40
6.1	Parton emission	41
6.2	Jet events	42
6.3	Strings in a $q\bar{q}g$ -configuration	43
7.1	An overview of the HERA facilities	50
8.1	An overview of the H1-detector	52
8.2	Longitudinal cut through the H1 detector	54
8.3	The H1 tracking system	55

8.4	The silicon trackers	56
8.5	The BST	56
8.6	An end-on view of the tracking system	57
8.7	The Backward Drift Chamber	58
8.8	The Forward Tracking Detector	59
8.9	The Liquid Argon calorimeter	60
8.10	The Layout and location of the SpaCal	61
9.1	A generic forward jet diagram	67
9.2	The positron cluster radius before and after correction	70
9.3	Beam-gas event	71
9.4	DIS-plots	74
9.5	A forward jet event	75
9.6	Purity, stability, background and acceptance in bins of x_{bj}	77
9.7	Purity, stability, background and acceptance in bins of x_{jet}	77
9.8	Purity, stability, background and acceptance in bins of $P_{t,jet}$	78
9.9	Scatter-plots for migration studies	79
9.10	Scatter-plots of Q^2 and y to study bin migrations	79
9.11	Scatter-plots of E_e and θ_e to study bin migrations	79
9.12	Q^2 -window as a function of reconstructed $P_{t,jet}$	80
9.13	Detector smearing of E_e	81
9.14	Real corrections	81
9.15	Diagrams of virtual corrections	82
10.1	Detector level cross sections	85
10.2	Correction factors for the cross section	86
10.3	Corrected cross sections	88
11.1	Scatter-plot showing $\eta_{\text{forward jet}}$ at detector vs. hadron level	90
11.2	Detector level E_t -flow	91
11.3	Correction factors for the E_t -flow	92
11.4	$E_t(\Delta\eta)$	94
11.5	$E_t(\eta)$	95
11.6	Transverse energy flow in inclusive DIS	96
11.7	Pion E_t -flow	96
11.8	Jet-profiles, detector level	98

11.9 Jet-profiles in bins of $\eta_{\text{forward jet}}$	99
11.10 Correction factors for the jet-profiles	100
11.11 Jet-profiles on detector vs. non-radiative hadron level	100
11.12 The corrected jet-profiles	101
11.13 Corrected jet-profiles in bins of $\eta_{\text{forward jet}}$	102
11.14 Detector level p_t -spectra	103
11.15 Correction factors in the full p_t -range	104
11.16 Correction factors for the p_t -spectra	104
11.17 The corrected p_t -spectra	106

Everything starts somewhere, though many physicists disagree.

[Terry Pratchett, 1948 -]

Chapter 1

Introduction

One of the major achievements for physics in the 20th century has been the advent of the Standard Model of particle physics. Many areas of physics have been united in this theory. Not only have the electromagnetic and the weak force been united, but also the strong interaction has been given a very beautiful description in the formulation of Quantum Chromo Dynamics (QCD). QCD has successfully described such diverse phenomena as the jet phenomenon and the short-distance structure of the proton.

The ultimate test of QCD is the breaking of the so-called Bjorken scaling in deep inelastic lepton-hadron scattering (DIS) predicted by perturbative QCD. This phenomenon has been studied in detail over the last decades and has proven a reliable key to the structure of the proton. Scaling violation is parametrised by the proton structure functions, which describe the contents of the proton in terms of the momentum distribution of the proton constituents, the “partons”, and the scale at which the proton is probed.

This high-energy limit of DIS has been successfully described by the so-called DGLAP equations¹, which will be described in detail in chapter 4. These equations describe the scaling violations in terms of logarithms of the “hardness” of the reaction, $\ln Q^2$, where Q is the momentum transfer between the lepton and the hadron. For DIS a consequence of DGLAP is the prediction that the lepton and the proton interact through a parton cascade, obeying a strong ordering in transverse momentum of the emissions. Figure 1.1 shows such a cascade.

The HERA collider - situated in Hamburg - is an accelerator consisting of two storage rings in which electrons or positrons are brought to collision with protons. The proton is a composite object, while the electron to the best of our knowledge is fundamental and hence is a point-like particle. This contrast enables us to consider HERA to be basically the Worlds largest microscope, using electrons to probe the inner structure of the proton.

A central result of HERA has been the discovery of a steep rise in the proton structure function in the region of low parton momentum relative to the total proton momentum. It seems that the parton density in the proton increases dramatically, as it is probed at lower and lower scales relative to the proton momentum. This behaviour is expected to be described in DIS not by logarithms of Q^2 , but rather by logarithms of $\frac{1}{x_{bj}}$, where x_{bj} is the fractional proton momentum carried by the interacting parton.

In the case of very low x_{bj} , and hence of high values of $\log \frac{1}{x_{bj}}$, the dynamics of the lepton

¹Dokschitzer, Gribov, Lipatov, Altarelli, Parisi

proton interaction are expected to be described by the so-called BFKL equations. They will also be described in chapter 4. The BFKL equations dictate that the parton cascade be ordered, not in transverse momentum, but in the *total energy* of the emitted particles. It turns out, however, that the BFKL equations suffer from complications that inhibit their predictive power. A solution to this problem has recently been offered, as it has been shown that the so-called CCFM equations are able to reproduce the p_t -ordering of DGLAP in the high- Q^2 limit as well as the energy ordering of BFKL in the low- x_{bj} limit. The CCFM equations are based on principles of colour coherence leading to imposition of *angular ordering* in emissions.

Searches have so far failed to give clear evidence for non-DGLAP dynamics. This is due to the fact that the phase space for DGLAP dynamics is far greater than that for BFKL-like dynamics. This leads to the conclusion that to find this new type of parton dynamics, it is necessary to look at very specific final states to extract a signal. One such final state was proposed by Mueller et al [Mue91b], [Mue91a], [BdRL92], [Tan92].

The idea is to investigate high energy parton emission in which the “room” for evolution in transverse momentum is severely restricted. This enhances the chance of seeing other types of dynamics. The method used is to study the events with a jet in the forward direction fulfilling certain kinematic requirements, and subsequently to compare the observations with predictions from the different QCD models.

The goal of this thesis is to investigate the parton dynamics of forward jet events. This is done through a cross section measurement of forward jet production and through the detailed study of event variables.

Part I constitutes an introduction to the relevant theory needed to understand this particular area of particle physics. The experimental apparatus of the H1 detector and the HERA collider is described in the second part. In part III, I will present a measurement of the forward jet cross section done with the H1 detector at HERA. The measurement is performed on data collected by the H1 collaboration during 1997, and the data are compared to various models of QCD.

To further distinguish between the employed models, several event variables have been studied with focus on the description of transverse dynamics given by the individual models.

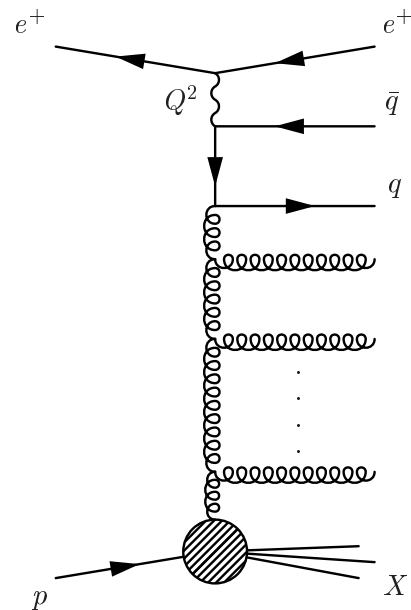


Figure 1.1: A parton cascade in DIS. The positron transfers a momentum Q , and the proton may dissociate into a complicated final state.

Part I

Theory

There is a theory which states that if ever anyone discovers exactly what the Universe is for and why it is here, it will instantly disappear and be replaced by something even more bizarrely inexplicable.

There is another theory which states that this has already happened.

[Douglas Adams, 1952 - 2001]

Chapter 2

Quantum Chromo Dynamics

Quantum Chromo Dynamics (QCD) is the theory of the strong nuclear force. QCD describes the interactions between *quarks* and *gluons*, and how they combine to form *hadrons* such as protons, neutrons or π -mesons.

In this chapter I will give a brief introduction to the so-called Quark Model, whereupon I will introduce the formal apparatus of QCD and discuss the physics it contains. The transition to a QCD description of the proton structure is saved for chapter 3.

2.1 The Quark Model

The quark model was originally suggested independently by Gell-Mann [GM64] and Zweig [Zwe] to explain the apparent $SU(3)$ symmetry in the mass spectra of the then-known hadrons. The cornerstone of the model was to suggest that the hadrons consist of either three *quarks* to form the half integer spin baryons or a *quark-antiquark pair* to form the mesons with integer spin.

The quarks themselves were thought of as occurring in (then) three varieties (flavours) having spin $\frac{1}{2}$ and having *fractional charges* of $+\frac{2}{3}$ and $-\frac{1}{3}$ of the proton charge. These three varieties were denoted u (up), d (down) and s (strange).

A proton was seen as consisting of two u and one d quark:

$$|p\rangle = |uud\rangle \tag{2.1}$$

This model from the beginning was quite successful in classifying the then known hadrons and predict the masses of some that had not been observed at the time. In spite of this a significant amount of objections were raised against it. How could one hypothesise about particles with properties that had never been seen? It must be possible to break up the hadrons in their constituents to observe their properties. All attempts at this failed, and it was argued that if energies at the GeV-scale were consistently not able to break up the proton, the binding energy of the individual quark had to be of the order of several GeV. This was obviously quite contrary to the observations putting the proton mass at roughly 1 GeV.

Another fundamental problem of the quark model was the fact that the quarks were postulated

to be fermions. In several of the hadrons there would have to be identical quarks with identical values of all known quantum numbers. This first seemed to be a violation of the Pauli exclusion principle, which states that no two fermions can be found in the same quantum state. The problem was solved with the advent of the *colour hypothesis*, which states that all quarks come in three *colours*, namely red, green and blue. “Colour” is here strictly referred to as a quantum number and not physical colour. The three colour states are assumed linearly independent, and the quarks may occur in any superposition - a *colour triplet* - of the three.

The asymmetry of the proton wave function could now be saved by writing it as:

$$|p\rangle = |\text{flavour,spin}\rangle \otimes |\text{colour}\rangle = |uud, \text{spin} = 1/2\rangle_S \otimes |\text{colour}\rangle_A \quad (2.2)$$

where S and A refer to ‘symmetric’ and ‘antisymmetric’ respectively.

The colour hypothesis also implied that hadrons be *colour neutral* and the quark bound states were thus seen to be invariant under $SU(3)_C$ -transformations.

Properties of the quark model, such as the colour hypothesis, have over the years become well established facts through many experimental measurements. In the beginning of the 1970’s Richard P. Feynman put forth the *Quark Parton Model* (QPM) in a series of talks and lectures. The QPM assumed hadronic particles to be composed of a small number of constituents, “partons”. These included the quarks, carrying electric charge, and possibly other particles holding the quarks together. The quarks were assumed to be essentially free and incapable of exchanging large portions of momentum. No one article stands out as the foundation of the QPM but [Fey72] and [Fey] are common references. With the discovery of *asymptotic freedom* the picture was finally complete, and the quark model has thus given birth to a full quantum field theory of the strong nuclear force. This theory is known as *Quantum Chromo Dynamics* (QCD), and it overcomes many of the objections raised above. In the following sections, I will treat QCD in detail.

2.2 Non-Abelian Yang-Mills Theory

The formulation of QCD rests upon the principles of invariance of the Lagrangian density under gauge transformations. In the case of QCD the Lagrangian must be invariant under $SU(3)_C$ -transformations.

I shall here provide only a brief treatment of the derivation of \mathcal{L}_{QCD} . For a more satisfactory treatment, the reader may consult [Pet94]. For an introduction to structure coefficients and representations see appendix A.

Fundamentally, the assumption of QCD is that matter is made out of quarks. The quark field is a fermion field, and as such may be described as a Dirac spinor $q_\alpha(x)$. We now denote the quark field colour triplet as

$$(q) = \begin{pmatrix} q^1 \\ q^2 \\ q^3 \end{pmatrix} = (q_\alpha^i(x)). \quad (2.3)$$

Ignoring the Dirac index α , the quark field transforms under $SU(3)_C$ as

$$q^i \rightarrow U_{ij} q^j \quad \text{or} \quad q \rightarrow \mathbf{U}q \quad (\text{and} \quad \bar{q} \rightarrow \bar{q}\mathbf{U}^\dagger), \quad (2.4)$$

where $\mathbf{U} \in SU(3)$.

Requiring that the free Lagrangian $\mathcal{L}_0 = \bar{q}(i\rlap{\not{D}} - m)q$ ¹ of the quark field remains invariant under $SU(3)$ -transformations inspires the definition of a covariant derivative:

$$\mathbf{D}_\mu = \partial_\mu + \mathcal{A}_\mu \quad (2.5)$$

where \mathcal{A}_μ is a 3×3 matrix field in the Lie-algebra of $SU(3)$. It is identified with the gluon field. Under a gauge transformation \mathcal{A}_μ can be readily shown to transform as

$$\mathcal{A}'_\mu = \mathbf{U}\mathcal{A}_\mu\mathbf{U}^\dagger - (\partial_\mu\mathbf{U})\mathbf{U}^\dagger \quad (2.6)$$

Defining the field strength tensor as:

$$\begin{aligned} \mathcal{F}_{\mu\nu} &= [\mathbf{D}_\mu, \mathbf{D}_\nu] \\ &= \partial_\mu\mathcal{A}_\nu - \partial_\nu\mathcal{A}_\mu + [\mathcal{A}_\mu, \mathcal{A}_\nu] \end{aligned} \quad (2.7)$$

we can without further ado write down the generic gauge-invariant Yang-Mills Lagrangian:

$$\mathcal{L} = \bar{q}(i\rlap{\not{D}} - m)q + \gamma Tr \{ \mathcal{F}_{\mu\nu}\mathcal{F}^{\mu\nu} \} \quad (2.8)$$

where γ is a dimensionless constant.

This Lagrangian is uniquely defined from the requirements of Lorentz invariance, gauge invariance and renormalisability when considering *only* the interactions of the fields $q(x)$ and $\mathcal{A}_\mu(x)$. There is nothing in equation (2.8) that refers explicitly to $SU(3)$, and in fact one may extract for instance the theory of electroweak interactions by replacing $SU(3)$ -symmetry with $SU(2) \otimes U(1)$ symmetry.

2.3 The Classical Lagrangian of Quantum Chromo Dynamics

Turning explicitly to $SU(3)$, we write \mathcal{A}_μ as a linear combination of the generators of the Lie-algebra in the fundamental representation:

$$\mathcal{A}_\mu = -ig\mathbf{T}^a A_\mu^a \quad (2.9)$$

where $\mathbf{T}^a = \frac{\lambda^a}{2}$ for $a = 1, \dots, 8$. The field strength tensor in the same way becomes:

$$\mathcal{F}_{\mu\nu} = -ig\mathbf{T}^a F_{\mu\nu}^a \quad (2.10)$$

Using the equations (2.7) and (2.10), one may show that

$$F_{\mu\nu}^a = \partial_\mu A_\nu^a - \partial_\nu A_\mu^a + gf_{abc}A_\mu^b A_\nu^c, \quad (2.11)$$

where f_{abc} are the structure coefficients of $SU(3)$. The gauge transformation of the gluon field shown in equation (2.6) becomes (for an infinitesimal global gauge transformation):

$$A_\mu^{\prime a}(x) = [\mathbf{1} - i\theta^c \tilde{\mathbf{T}}^c]_{ab} A_\mu^b(x) \quad (2.12)$$

¹ $\rlap{\not{D}} = \partial_\mu \gamma^\mu = \sum_{\mu=1}^4 \partial_\mu \gamma^\mu$

where $(\tilde{\mathbf{T}}^c)_{ab} = -if_{cab}$ is the $SU(3)$ generator of the *adjoint* or *octet* representation.

Writing out the trace in equation (2.8) it follows that

$$\text{Tr} \{ \mathcal{F}_{\mu\nu} \mathcal{F}^{\mu\nu} \} = -\frac{1}{2} g^2 F_{\mu\nu}^a F^{\mu\nu a}. \quad (2.13)$$

Taking $\gamma \equiv \frac{1}{2g^2}$, we can now write down the full Lagrangian of QCD and try to interpret it:

$$\begin{aligned} \mathcal{L}_{QCD} &= \sum_f \left\{ \bar{q}^{(f)} (i \not{D} - m_f) q^{(f)} \right\} + \frac{1}{4} F_{\mu\nu}^a F^{\mu\nu a} \\ &= \underbrace{\sum_f \left\{ \bar{q}^{(f)} (i \not{D} - m_f) q^{(f)} \right\}}_{\text{I}} + \underbrace{\sum_f \left\{ g \bar{q}^{(f)} \mathbf{T}^a \not{A}^a q^{(f)} \right\}}_{\text{II}} + \frac{1}{4} F_{\mu\nu}^a F^{\mu\nu a} \end{aligned} \quad (2.14)$$

where the f -index refers to quark flavours.

To understand the physical contents of equation (2.14), it is instructive to write out the tensor product of the field strength tensors. I will here just write the result:

$$\begin{aligned} F_{\mu\nu}^a F^{\mu\nu a} &= \underbrace{(\partial_\mu A_\nu^a - \partial_\nu A_\mu^a)(\partial^\mu A^{\nu a} - \partial^\nu A^{\mu a})}_{\text{III}} + \underbrace{2g f_{abc} A_\mu^b A_\nu^c (\partial^\mu A^{\nu a} - \partial^\nu A^{\mu a})}_{\text{IV}} \\ &\quad + \underbrace{g^2 f_{abc} f_{ab'c'} A_\mu^b A_\nu^c A^{\mu b'} A^{\nu c'}}_{\text{V}} \end{aligned} \quad (2.15)$$

I will briefly comment on the couplings between the quark and the gluon fields as they are found in equations (2.14) and (2.15). We are still in principle treating a classical theory, so these considerations have little direct applicability. However, it is nice to see some of the basic properties of the full quantum field theory read directly off the Lagrangian.

I This term describes the free quark field only. It gives rise to the free quark propagator.

II This term describes the coupling of the quark field to the gluon field.

III This is the kinetic term of the gluon field which gives rise to the gluon propagator.

IV As this term contains three A-factors, it describes a three-gluon self-coupling.

V In this term there are four gluon fields. This gives rise to the only quartic vertex in the Standard Model, namely the four-gluon coupling.

An extremely interesting point is that the coupling constant of the theory is determined from the gluon self-coupling alone, which again tells us that *all quark flavours couple to the gluon field with the same strength*. This is a property exclusive to non-Abelian gauge theories, as it stems from the non-Abelian terms in equation (2.15).

To summarise, the assumption of $SU(3)_C$ -invariance of the fermionic quark field triplets leads to a uniquely defined theory of strong interactions containing eight massless gluon fields in the octet (or *adjoint*) representation of $SU(3)$. Particular to this theory is that the bosonic fields interact not only with the fermions but also with each other².

Quark	Q/Q_p	Mass	Hadron energy (MeV)
u	$\frac{2}{3}$	≈ 4 MeV	$\frac{1}{2}m_\rho = 384$
d	$-\frac{1}{3}$	≈ 7 MeV	$\frac{1}{2}m_\rho = 384$
c	$\frac{2}{3}$	≈ 1.5 GeV	$\frac{1}{2}m_{J/\psi} = 1549$
s	$-\frac{1}{3}$	≈ 135 MeV	$\frac{1}{2}m_\phi = 510$
t	$\frac{2}{3}$	≈ 170 GeV	N.A.
b	$-\frac{1}{3}$	≈ 5 GeV	$\frac{1}{2}m_\Upsilon = 4730$

Table 2.1: [PDG98] The properties of the six quarks are listed here. Note that because free quarks cannot be observed, the listed masses are the so-called current masses for all the hadron forming quarks, whereas the t -mass is found from direct observations of t -decays. The t is extremely heavy and thus has too short a lifetime to form hadrons which is also the reason no hadron energy is listed.

2.3.1 Feynman Rules

To calculate amplitudes and cross sections for specific processes in a quantum field theory one uses perturbation theory in the form of *Feynman rules*. These are rules that describe an algorithm derived from the Lagrangian. The algorithm consists in short of writing down diagrams for *all possible processes* (to a given order in the coupling constant) with a given final state, $|F\rangle$ and initial state, $|I\rangle$. One then substitutes given mathematical expressions for the elements of the diagrams to calculate probability amplitudes $\langle F|S|I\rangle$, where S is the *scattering matrix*. The physical probability to a given order is then $|\langle F|S|I\rangle|^2$.

The Feynman rules are reviewed in figure 2.1. In this figure all momenta point towards the vertex so that the sum of all external momenta is zero.

In the figure, one may note that references are made to a λ -parameter. This parameter is connected to a choice of gauges within the class of *covariant gauges*. In this class of gauges one adds an additional term to (2.14) that introduces the so-called *Faddeev-Popov* ghosts. These are complex scalar fields that obey Fermi statistics(!). The ghost fields are denoted by dotted lines in the figure. For details on choice of gauge see [ESW96].

²Although the Glashow-Salam-Weinberg model of electroweak interactions contains a ZWW-vertex, this is the only part of the SM in which gauge bosons are seen to interact with other bosons of the same type.

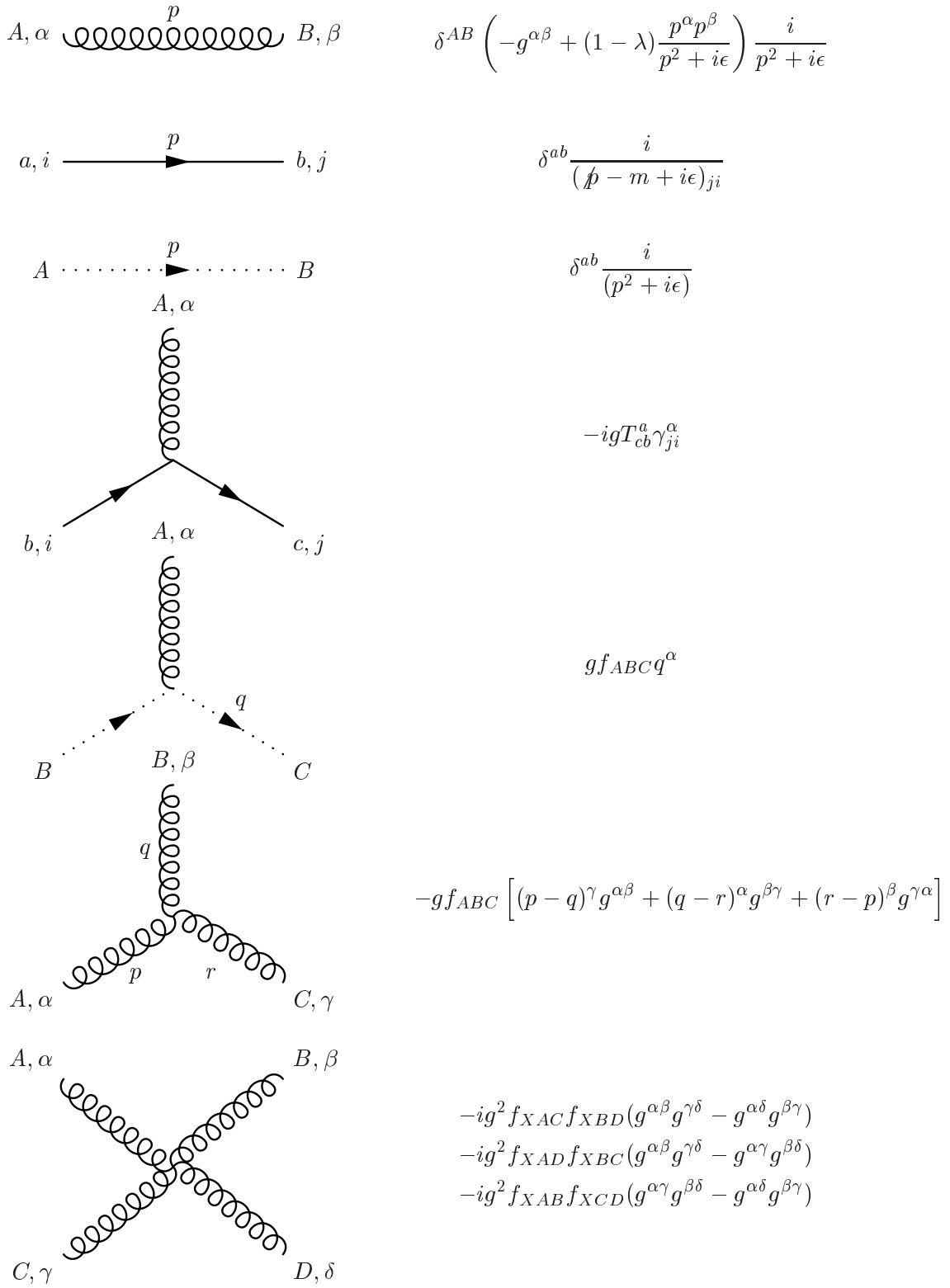


Figure 2.1: A figure showing all Feynman diagram components and their mathematical expression. Straight lines are quarks, curly lines are gluons. The dotted lines are scalar ghosts (obeying Fermi statistics) which are necessary in some gauges.

2.4 Renormalisation and Asymptotic Freedom

The Lagrangian as it is written out in equation (2.14) does not describe the full theory. To fully formulate the theory, one needs to address the problem of *renormalisation*.

As (2.14) is written, couplings are described in terms of a dimensionless constant g . One may now consider a theory in which the quark masses are set to zero (a fairly good approximation for the u and d quark). As the coupling constant is dimensionless, \mathcal{L}_{QCD} is seen to be scale invariant. One may redefine the scale of length (and thus also of energy) and find that the theory remains invariant. This is of course in direct contradiction with the observations, as we do not observe protons of any given size. Quite the contrary there seems to be a general scale of approximately 1 fm or 1 GeV for the strong interactions, as can be seen from table 2.2.

Physical dimension of the hadrons	$\sim 1 \text{ fm} \sim 5 \text{ GeV}^{-1}$
Total hadronic cross section	$\sim (1 \text{ fm})^2$
Universal Regge slope [Pet94]	$\alpha' \sim 1 \text{ GeV}^{-2}$
Mass of the lightest baryons	$\sim 1 \text{ GeV}$

Table 2.2: *Examples of the general scale of the strong interaction.*

2.4.1 Running of the Coupling Constant

A property of *quantum* field theories is the way the coupling constant varies with the scale at which you probe the theory. To understand the running of the coupling constant in QCD, it is instructive to start by considering Quantum Electro Dynamics (QED).

Amplitudes in QED are given as a function of the electron charge, which is the coupling constant of the theory. This of course implies that a precise definition and measurement of the electron charge is a fundamental part of the theory.

When measuring the electron charge, however, a fundamental fact of quantum field theory comes into play. *You cannot specify the charge without specifying the scale at which you probe it.* If we want to measure the charge of the electron sketched in figure 2.2(a), we may do so by measuring the Coulomb force between the electron and a test charge.

At “large” distances the test charge will experience not just the Coulomb force of the electron charge itself. It will also interact with all quantum fluctuations emanating from the electron itself or from the vacuum.

Because the electron is negatively charged, the positrons of the fluctuations will tend to be closer to the electron, which will subsequently be surrounded by a polarised cloud in such a way that the electron charge is screened. One refers to this as *vacuum polarisation*.

As we move our test charge closer to the electron itself, we penetrate the cloud of virtual charges surrounding it, and we will thus measure an increasing electrostatic force between the two charges, exceeding the contribution from the Coulomb-potential.

It turns out that

$$\lim_{Q^2 \rightarrow \infty} (g_{QED}) = \infty.$$

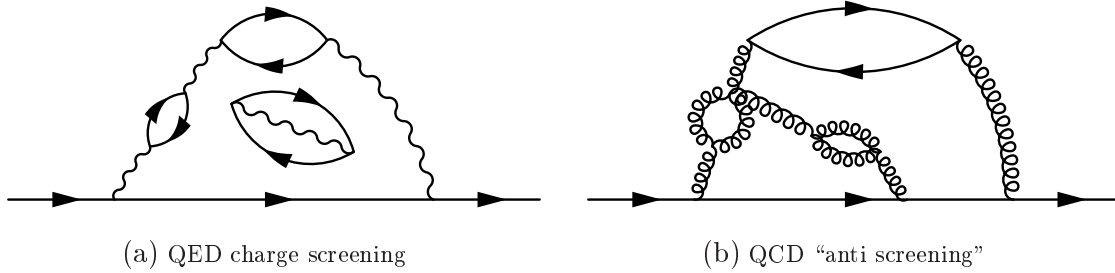


Figure 2.2: QED charge screening vs properties of QCD.

QED is thus expected to break down at extremely high energies. The theory is said to contain a *Landau pole*. This Landau pole, however, does not threaten the validity of perturbation theory for energies below 10^{279} GeV [Pet94], and we may thus safely trust QED as we know it for all energies that are currently available for experiments.

As a consequence of this *charge screening*, we can not consider the bare electron charge a meaningful physical quantity. We may instead measure it at a given energy scale and specify all physical predictions in terms of this *renormalisation scale*.

In QCD the charge screening has the opposite effect, as the gauge bosons are now free to interact also among one another (see figure 2.2(b)).

The reason for this behaviour arises from considering the *full* amplitude for $q \rightarrow q$ depicted in equation (2.16)

$$\begin{aligned}
 \Gamma_{\mu}^{(2)} = & \text{---} \text{---} \text{---} + \text{---} \text{---} \text{---} \\
 & + \text{---} \text{---} \text{---} + \text{---} \text{---} \text{---} \\
 & + \dots
 \end{aligned}
 \tag{2.16}$$

It turns out that adding the two diagrams

$$\dots + \text{---} \text{---} \text{---} + \text{---} \text{---} \text{---} + \dots$$

they contribute *with opposite signs*, and therefore not only cancel the screening of the colour charge, but even reverse the effect [AP99], [Pet94]. This fact can be seen from the so-called *renormalisation group equations* that specify the running of the coupling constant as the scale at which it is probed varies ([AP99] ch. 5).

Making the conventional choice of definition of the strong coupling constant

$$\alpha_s = \frac{g^2(Q^2)}{4\pi}$$

the renormalisation group equation reads [Pet94]

$$\frac{d}{d \log Q^2} (\alpha_s^{-1}(Q^2)) = \frac{1}{12\pi} (11N_C - 2N_f),
 \tag{2.17}$$

where N_C is the number of colours (3 for the case of QCD) and N_f is the number of active quark flavours.

One may then obtain [PS] / [Pet94]

$$\alpha_s = \frac{12\pi}{11N_C - 2N_f} \frac{1}{\log Q^2/\Lambda^2} \quad (2.18)$$

where Λ is a constant of integration.

Looking at equation 2.18 we first note, that the first fraction is always positive. QCD contains three colours and $N_f \leq 6$.³ We then turn to the limit of $Q^2 \rightarrow \infty$ in which α_s is seen to converge to zero. We may indeed consider the quarks to behave like free fermions as stipulated in the QPM. The theory is said to exhibit *asymptotic freedom*.

Considering now the limit of $Q^2 \rightarrow \Lambda^2$ we see that α_s diverges. This means that as we approach this limit, we cannot expect higher order processes to have negligible amplitudes. Perturbation theory thus ceases to be valid. Λ consequently represents a cut-off scale, where we can no longer apply perturbative QCD.

Experimental measurements of Λ gives a value of $\Lambda \approx 200$ MeV. We can thus trust perturbation theory when Q is significantly larger than this value. At a value of $Q^2 = 1$ GeV², α_s is approximately 0.4. Correspondingly, we may conclude that the strong interaction becomes strong for distances larger than $\frac{1}{\Lambda}$, which is the approximate size of the light hadrons ($c\hbar/200$ MeV ≈ 1 fm).

³At present day collider experiments one can normally safely assume N_f to be 4 or 5.

Chapter 3

Theory of Deep Inelastic Scattering

Deep Inelastic lepton-hadron Scattering (DIS) was suggested by Bjorken in 1966 as a testing ground for obtaining information on the nucleon structure. The keystone of Bjorken's argument was that by studying the properties of the scattered lepton alone and ignoring the hadronic final state, one could obtain information on the (then) hypothetical quark contents of the protons and neutrons. The experiments of the time were fixed target experiments, where electrons were brought to collide with nuclei. This is contrary to the situation at HERA, where a beam of electrons or positrons collide with a proton beam enabling much higher centre-of-mass energies to be reached.

I will here give an introduction to the basic theoretical formalism needed to study DIS in the HERA context. From there, chapter 4 will discuss the transition from first principle QCD/QED calculations to evolution schemes of different nature.

3.1 Kinematics of Deep Inelastic Scattering

The generic DIS process is:

$$l + p \rightarrow l' + X \quad (3.1)$$

This describes the most general form of scattering by a lepton on a proton. The process may take place via charged as well as neutral currents, and we include all possible hadronic final states X . As we shall be working with positron-proton-scattering, we now limit ourselves to considering the process

$$e^+ + p \rightarrow e^+ + X \quad (3.2)$$

We assign four-momenta to the individual particles in the process as shown in figure 3.1. Independently of the process denoted by the circle, we can define some kinematic variables. The invariant centre-of-mass energy of the ep -system is denoted \sqrt{s} , where

$$s \equiv (p_e + P)^2 \quad (3.3)$$

A variable which is more relevant to DIS, where one of the incident particles is composite, is

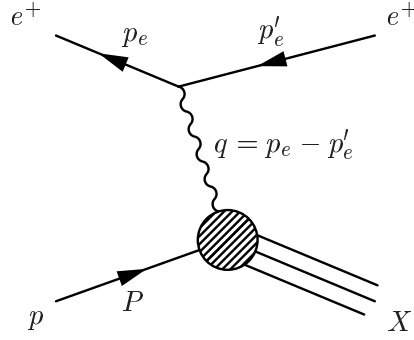


Figure 3.1: A diagram representing DIS.

the invariant mass of the hadronic final state. This is defined by:

$$W^2 \equiv (P + q)^2 \quad (3.4)$$

This quantity collects the invariant mass colliding with the positron and can be seen as the centre-of-mass energy of the photon-proton system.

The negative square of the four-momentum transfer is:

$$Q^2 \equiv -q^2 = -(p_e - p'_e)^2 \quad (3.5)$$

Q may be considered the invariant mass (often referred to as *virtuality*) of the photon.

DIS events are often described in terms of the dimensionless variables¹

$$x_{bj} \equiv \frac{Q^2}{2P \cdot q} \quad (3.6)$$

$$y \equiv \frac{P \cdot q}{P \cdot p_e}. \quad (3.7)$$

y varies between 0 and 1, as can be seen from the fact that (3.7) in the proton rest frame reduces to:

$$y = 1 - \frac{E'_e}{E_e} \quad (3.8)$$

where the prime denotes the positron energy *after* the collision. This directly provides the limit:

$$0 \leq y \leq 1 \quad (3.9)$$

For obvious reasons y is referred to as the *inelasticity* of the collision. For $y = 0$ the positron retains its energy, and we have a case of elastic scattering. Correspondingly, $y = 1$ represents the case of a completely inelastic collision. The limits are valid in all frames of reference due to Lorentz invariance. y provides a quantitative way of defining the phase space for DIS.

We can infer a limit on x_{bj} directly by noting that

$$W^2 = (P + q)^2 = m_p^2 - Q^2 + 2P \cdot q \quad (3.10)$$

from which it follows that

$$x_{bj} = \frac{Q^2}{W^2 + Q^2 - m_p^2} \quad (3.11)$$

¹The subscript bj refers to J. D. Bjorken, one of the founding fathers of the Quark Parton Model (QPM)

By definition $Q^2 \geq 0$. Also $W^2 - m_p^2 \geq 0$, as the invariant mass of the hadronic final state must be larger than m_p , when the lepton energy decreases. It now follows that $x_{bj} \geq 0$. As Q^2 goes to zero so does x_{bj} . From this it is seen that

$$0 < x_{bj} < 1. \quad (3.12)$$

In the framework of the Quark Parton Model (QPM), where the photon scatters on the point-like constituents of the proton, x_{bj} is the fraction of the proton momentum carried by the struck parton (see section 3.3.1)

A variable which is often also used is ν , given by:

$$\nu \equiv P \cdot q \quad (3.13)$$

In the proton rest frame, it reduces to

$$\nu = m_p(E'_e - E_e) \quad (3.14)$$

This shows that ν is a measure of the energy of the exchanged boson.

A final note on Q^2 is that it is solely dependent on the positron vertex. It can be shown that:

$$Q^2 \approx 2E_e E'_e (1 - \cos \theta) \quad (3.15)$$

where θ refers to the positron scattering angle. This follows directly from the defining relation (3.5):

$$Q^2 = -(p_e - p'_e)^2 = -(p_e^2 - p_e'^2 - 2p_e p'_e) \quad (3.16)$$

$$= -[2m_e^2 - 2(E_e E'_e - \vec{p}_e \cdot \vec{p}'_e)] = -2m_e^2 + 2E_e E'_e - 2|\vec{p}_e||\vec{p}'_e| \cos \theta \quad (3.17)$$

$$\approx 2E_e E'_e (1 - \cos \theta) \quad (3.18)$$

Equation 3.15 is valid in all frames of reference. The larger the scattering angle, the larger Q^2 . The upper limit on Q^2 is given by s as:

$$Q^2 = x_{bj} y (s - m_p^2) \approx x_{bj} y s \quad (3.19)$$

The approximation uses the fact that HERA energies are orders of magnitude larger than the proton mass, which is why we may in practice safely neglect it.

3.1.1 Reconstruction of Kinematic Variables

As mentioned above, Q^2 may be parametrised by positron information alone. This is also the case for the other variables of DIS.

The standard H1 coordinate system is defined with the positive x-axis pointing toward the centre of the HERA ring, and the positive y-axis pointing vertically upwards. The positive z-axis is in the proton direction. This corresponds to a polar angle of $\theta = 0$, and angles specified in the remainder of this thesis will *not* be positron scattering angles like in equation (3.15), but rather $\pi - \theta_{scatter}$ as shown in figure 3.2.

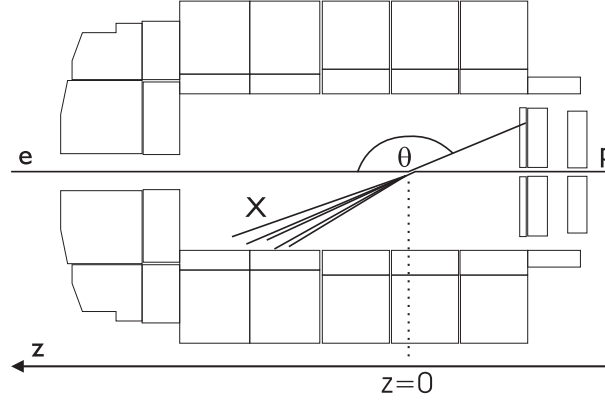


Figure 3.2: Definition of the polar angle in H1.

Reconstructing the kinematics from the scattered positron alone is one among several methods, and it is known as *the electron method*. The parameters are reconstructed according to:

$$Q^2 = 2E_e E'_e (1 + \cos \theta) \quad (3.20)$$

$$y = 1 - \frac{E'_e}{2E_e} (1 - \cos \theta) \quad (3.21)$$

$$x_{bj} = \frac{Q^2}{sy} \quad (3.22)$$

Note the change of sign between equations (3.15) and (3.20). This is due to the definition of the polar angle, which is *not* the lepton scattering angle. Note also that m_e and m_p have been neglected in (3.22) as they are much smaller than s .

The primary advantage of the electron method is that it is easy to use, as it only requires the accurate reconstruction of one particle. Its problems, on the other hand, are a large sensitivity to radiative corrections (see section 9.8.2) and a low x_{bj} -resolution at low y -values. This resolution problem is seen by considering the error on x_{bj} :

$$\sigma_x^2 = \left(\frac{\partial x}{\partial y}\right)^2 \sigma_y^2 + \left(\frac{\partial x}{\partial s}\right)^2 \sigma_s^2 + \left(\frac{\partial x}{\partial Q^2}\right)^2 \sigma_{Q^2}^2 + (\text{mixed derivatives}) \times (\text{correlations}) \quad (3.23)$$

At low y -values, this error will be dominated by the σ_y -term:

$$\sigma_x \approx \left|\frac{\partial x}{\partial y}\right| \sigma_y = \frac{Q^2}{sy^2} \sigma_y = \frac{x}{y} \sigma_y \quad (3.24)$$

In this analysis, the electron method has been used. As we cut away events with $y < 0.1$, this method is quite safe, as long as we take into account corrections for QED radiation.

3.1.2 Frames of Reference

In accelerator based particle physics experiments, one most often wishes to work in the Centre-of-Mass System (CMS), as both the initial and final states are then known to be at rest, constraining the kinematics significantly.

In ep -collisions, however, the lepton-parton CMS is not known due to the composite nature of the proton. One therefore often chooses to work in other frames of reference. The most common ones are:

The Laboratory Frame

The laboratory frame is in many aspects the easiest to use. The detector geometry is clearly defined, so effects arising from detector inadequacies, such as dead areas in calorimeters, are clearly defined. The downside is that physics signals can be “washed out” by the varying boost of the CMS.

The Hadronic Centre-of-Mass Frame

It is often of interest to consider physics variables in other systems than the laboratory frame. Some physics parameters may be easier to analyse and understand. One such frame is *The Hadronic Centre-of-Mass (HCM) frame*. The HCM frame is defined as the photon-proton centre-of-mass system, and it is precisely the rest frame of the hadronic final state.

Many analyses have been carried out in the HCM frame, as the connection between the physics and the geometry of the event is clearer here. The price is a reduced understanding of the detector geometry, as the boost and rotation angle will vary event by event.

The Breit Frame

In the Breit frame, the momentum transfer of the positron has only a z -component [ESW96]. The four-momentum of the exchanged virtual photon therefore becomes:

$$q = (0, 0, 0, Q) \quad (3.25)$$

The Breit frame is often referred to as the *brick wall frame*. Considering the collision in the QPM as seen in figure 3.3, the struck quark enters the reaction from the right with $p_z = -\frac{1}{2}Q$. It sees the photon as a “brick wall” from which it simply rebounds, carrying away a momentum portion $p_z = \frac{1}{2}Q$

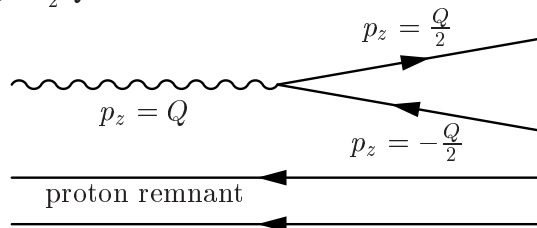


Figure 3.3: Photon-quark collision in the Breit frame

The Breit frame is used to define variables for the jet algorithm used in this analysis, namely the *inclusive k_t -algorithm* (see section 6.5). The reason for this is that the right-hand side of the event should look like one hemisphere of an e^+e^- -annihilation event at $E_{CM} = Q$. This side of the event is therefore often referred to as the *current jet hemisphere*. In contrast the left-hand side of the event which contains the proton remnant is denoted the *beam jet*

hemisphere. The similarity between the current jet hemisphere and a $q\bar{q}$ -hemisphere from e^+e^- -physics makes it easier to carry over the definition of jets from the $q\bar{q}$ case where the initial state consists of two point particles (the quarks) to DIS, where the initial state contains one point particle (the struck quark) and an extended object (the proton remnant).

3.1.3 Coordinates

In experiments, where the CMS is known, or perhaps even coincides with the laboratory frame, the relevant coordinates to use will almost always be the standard spherical coordinates (θ, ϕ) . At collisions involving hadrons, other coordinates are typically used. This is due to the fact that (θ, ϕ) -coordinates do not behave “nicely” under a Lorentz transformation.

At HERA a typical choice of coordinates is (η, ϕ) , where ϕ is the standard azimuthal angle. η is called the *pseudorapidity*. The definition stems from the definition of *rapidity* [PDG98]:

$$y = \frac{1}{2} \ln \left(\frac{E + p_z}{E - p_z} \right) = \tanh^{-1} \left(\frac{p_z}{E} \right) \quad (3.26)$$

Under a boost β in the z -direction, the rapidity transforms additively:

$$y \rightarrow y - \tanh^{-1} \beta \quad (3.27)$$

Rapidity differences between particles or jets in an event are therefore invariant under longitudinal boosts. The only problem is that calculation of rapidity requires a measurement of any two of E, p or m , which is difficult. In the high energy limit where $E \simeq p$, the rapidity may be approximated by the pseudorapidity [PDG98]:

$$y \approx \eta = -\ln \left[\tan \left(\frac{\theta}{2} \right) \right] \quad (3.28)$$

which only depends on the measurement of θ .

The requirement for η to be approximately equal to y is that $p \gg m$ and $\theta \gg 1/\gamma$ [PDG98].

3.2 The Elastic QED Cross Section

At low energies, ep -scattering can be described quite accurately as coherent QED-scattering between the lepton and the proton. Experiments at low energies have traditionally been fixed-target experiments where the proton is at rest. *Elastic scattering* means that both the lepton and the proton retain their identities. A diagram representing the amplitude for an electron-proton scattering process in QED is shown in figure 3.4.

Note that no contribution from Z^0 is noted here, as $Q^2 \ll m_Z^2$.

Taking the proton as being at rest and assigning momenta as in figure 3.1 ($P_i \equiv 0$), the process has most often been described in terms of the *Mott* cross section ([BJ] p. 437):

$$\left(\frac{d\sigma}{d\Omega} \right)_{Mott} = \frac{\alpha^2 \cos^2 \left(\frac{\theta}{2} \right)}{4E_e^2 \sin^4 \left(\frac{\theta}{2} \right) \left[1 + \frac{2E_e}{m_p} \sin^2 \left(\frac{\theta}{2} \right) \right]} \quad (3.29)$$

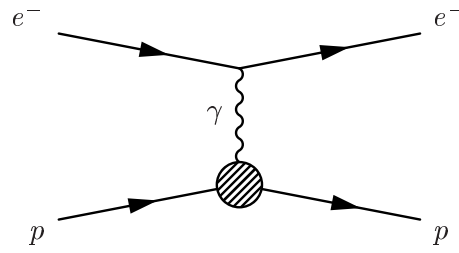


Figure 3.4: Elastic e-p scattering.

α is the electromagnetic coupling constant often referred to as the *fine structure constant*. We have here reverted to the definition of θ as the lepton scattering angle. It is defined in the laboratory frame, which is now the proton rest frame.

The Mott cross section is valid for the electromagnetic scattering of two point-like spin $\frac{1}{2}$ Dirac particles. It differs from the classical Rutherford calculation through the inclusion of the spin of the particles and by allowing the struck particle to recoil.

The proton, however, is an extended object, and it cannot be described in the same way as the electron current:

$$j_\mu = -e\bar{u}(p'_e)\gamma_\mu u(p_e) \quad (3.30)$$

Writing down the proton current in its most general form ([BJ] p. 437), one finds it to be of the form

$$J^\mu = e\bar{u}(P') \left[F_1(q^2)\gamma^\mu + \frac{\kappa}{2m_p}F_2(q^2)i\sigma^{\mu\nu}q_\nu \right] u(P). \quad (3.31)$$

$\sigma^{\mu\nu}$ is defined by $\sigma^{\mu\nu} = \frac{i}{2}[\gamma^\mu, \gamma^\nu]$, and κ is the anomalous magnetic moment of the proton. F_1 and F_2 are independent form factors parametrising the detailed structure of the proton represented by the “blob” in figure 3.4. In the Breit frame they can be shown to describe the proton charge and magnetic moment distributions [HM]. They will be interpreted in detail for inelastic scattering in section 3.3.1.

In the limit $q^2 \rightarrow 0$, both form factors go to 1, as the proton is then viewed as a point-like particle with magnetic moment $(1 + \kappa)\frac{e}{2m_p}$. Its substructure is not resolved by the exchanged photon, as the photon wavelength is much larger than the size of the proton.

A calculation of the scattering cross section gives [BJ]:

$$\frac{d\sigma}{d\Omega} = \left(\frac{d\sigma}{d\Omega} \right)_{Mott} \times \left\{ \left[F_1^2(q^2) - \frac{\kappa^2 q^2}{4m_p^2} F_2^2(q^2) \right] - \frac{q^2}{2m_p} [F_1(q^2) + \kappa F_2(q^2)]^2 \tan^2 \left(\frac{\theta}{2} \right) \right\} \quad (3.32)$$

Remember that we are still considering *elastic* scattering. The inelastic variables defined in section 3.1 have not yet come into play.

If the proton were structureless, F_1 would be 1 for all values of q^2 and κ would be zero. This would revert equation (3.32) to

$$\frac{d\sigma}{d\Omega} = \left(\frac{d\sigma}{d\Omega} \right)_{Mott} \left[1 - \frac{q^2}{2m_p^2} \tan^2 \left(\frac{\theta}{2} \right) \right] \quad (3.33)$$

which is basically the Mott cross section supplemented with a treatment of the magnetic moment. This is precisely the cross section for $e\mu \rightarrow e\mu$ ([BJ] p. 437) if one substitutes m_μ for m_p .

3.3 The Inelastic Cross Section to Lowest Order

Moving on to inelastic scattering, the electromagnetic cross section for the process $l p \rightarrow l X$ is given by [ESW96]:

$$\frac{d^2\sigma^{em}}{dx_{bj}dy} = \frac{8\pi\alpha^2 m_p E_e}{Q^4} \times \left[\left(\frac{1 + (1-y)^2}{2} \right) 2x_{bj}F_1^{em} + (1-y)(F_2^{em} - 2x_{bj}F_1^{em}) - \left(\frac{m_p}{2E_e} \right) x_{bj}yF_2^{em} \right] \quad (3.34)$$

This equation is valid for charged leptons and for $Q^2 \ll m_Z$. Note how the inelastic variables now come into play, as they are no longer constrained by the kinematics of elastic scattering.

3.3.1 Proton Structure in the Quark Parton Model

In inelastic scattering, the form factors evolve from being merely functions of q^2 (or Q^2), as in the elastic case, to being functions of both x_{bj} and Q^2 . However, it was Bjorken's great achievement that he predicted the scaling of the structure functions.

The *Bjorken limit* is defined as the limit in which Q^2 and $\nu = P \cdot q \rightarrow \infty$, while x_{bj} is kept fixed. *Bjorken scaling* is the term for the observation that the structure functions in this limit behave as:

$$F_i(x_{bj}, Q^2) \rightarrow F_i(x_{bj}) \quad (3.35)$$

This shows that the structure functions cease to have any dependence on the absolute energy scale of the reaction. They are only functions of the dimensionless scaling variable introduced in section 3.1. An illustration of Bjorken's prediction is shown in figure 3.5² The data have been obtained over more than twenty years in many different experiments. As can be seen, the measurements are very alike despite the fact that the Q^2 -range spans four orders of magnitude.

The physical interpretation of the scaling phenomenon is that the photon scatters on point-like constituents of the proton. Had these constituents had a non-trivial spatial distribution, the structure functions would have a Q/Q_0 -dependence, with $1/Q_0$ as a characteristic scale of the constituents. In other words the resolving power of the photon relative to the scale $1/Q_0$ of the proton constituents would have to be taken into account.

We can now formulate DIS in the QPM-picture. We work in the ultra-relativistic limit in which $E_p \approx P$ ($c = 1$ as usual). This means that $P \gg m_p$. In other words, we can neglect the mass of the proton. We also ignore any intrinsic motion of the partons in the proton. The photon scatters incoherently on a point-like quark constituent carrying a fraction ξ of the proton momentum ($p_q^\mu = \xi P^\mu$). Equation (3.34) can now be rewritten as [ESW96]:

$$\frac{d^2\sigma}{dx_{bj}dQ^2} = \frac{4\pi\alpha^2}{Q^4} \left\{ [1 + (1-y)^2]F_1 + \frac{1-y}{x_{bj}}(F_2 - 2x_{bj}F_1) \right\} \quad (3.36)$$

²Reproduced from [ESW96] p. 88

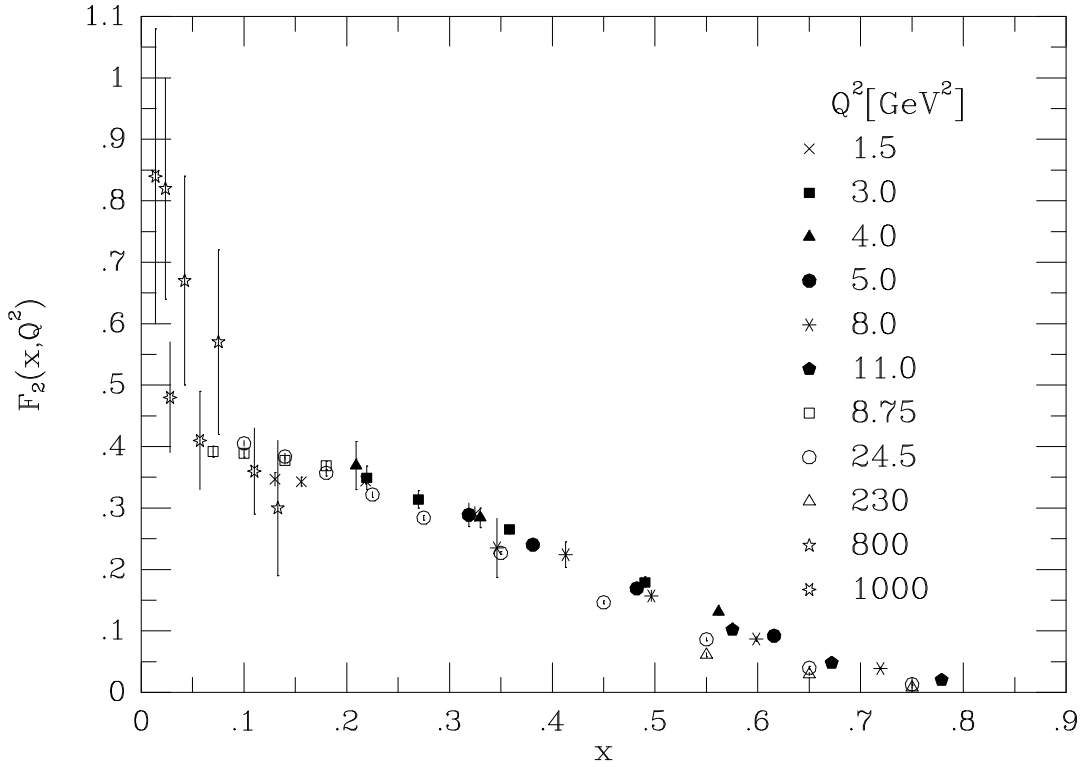


Figure 3.5: Measurements of F_2 from SLAC-MIT, BCDMCS, H1 and ZEUS.

It can be shown from considerations of the basic matrix-element for $2 \rightarrow 2$ - scattering that the partonic cross section must also satisfy ([ESW96] p. 89):

$$\frac{d^2\hat{\sigma}}{dx_{bj}dQ^2} = \frac{4\pi\alpha^2}{Q^4} [1 + (1-y)^2] \frac{1}{2} e_q^2 \delta(x_{bj} - \xi) \quad (3.37)$$

Comparison of the two expressions gives the structure functions in this picture as:

$$\hat{F}_2 = x_{bj} e_q^2 \delta(x_{bj} - \xi) = 2x_{bj} \hat{F}_1 \quad (3.38)$$

The “hat” denotes the fact that these quantities refer to the individual partons and not to the proton as a whole. The above relation between \hat{F}_1 and \hat{F}_2 is known as the *Callan-Gross relation*.

Equation (3.38) provides the reason for the traditional interpretation of x_{bj} . \hat{F}_2 describes a quark constituent mass with momentum fraction $\xi = x_{bj}$. From figure 3.5, it is obvious that F_2 is a distribution rather than a delta function. This indicates that the constituents of the proton carry a continuous range of momentum fractions. Figure 3.6 shows an intuitive picture of F_2 , as it should behave for the proton considered as one of four possibilities:

1. A point particle. The struck “parton” is the proton itself. All momentum is carried by this particle.
2. The proton consists of three valence quarks, carrying $1/3$ of the proton momentum each.

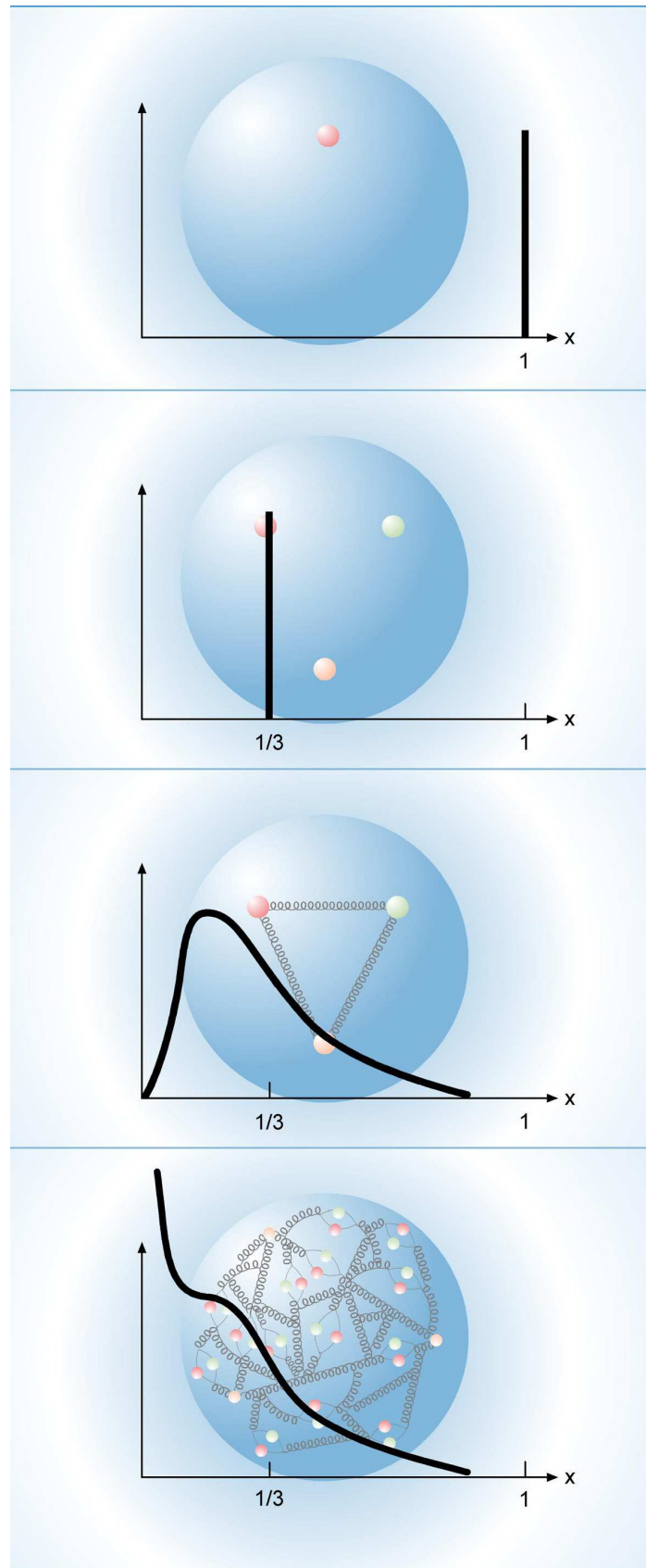


Figure 3.6: The expected behaviour of F_2 for three different notions of the proton contents [DES].

3. The proton contains three bound valence quarks. The quarks are held together by gluons. These must consequently carry some of the momentum, and the exchange of momenta smears the distribution
4. The proton consists of three valence quarks plus a number of gluons, and sea quark pairs carrying possibly very low momenta, thus creating the low- x rise of F_2 .

The idea of the continuous momentum spectrum together with equation 3.38 are incorporated into the so-called *naïve parton model* [Fey72], in which the virtual photon scatters *incoherently* off the individual quarks. In this model, the *quark distribution function* $q(\xi)$ is introduced. $q(\xi)d\xi$ represents the probability that a quark q carries a proton momentum fraction ξ between ξ and $\xi + d\xi$.

We can now obtain the structure functions by weighting $q(\xi)$ with the quark distribution functions:

$$\begin{aligned}
 F_2(x_{bj}) = 2x_{bj}F_1(x_{bj}) &= \sum_{q,\bar{q}} \int_0^1 d\xi q(\xi) x_{bj} e_q^2 \delta(x_{bj} - \xi) \\
 &= \sum_{q,\bar{q}} e_q^2 x_{bj} q(x_{bj})
 \end{aligned} \tag{3.39}$$

3.4 DIS to First Order in α_s

So far, we have studied the ep -scattering only for electromagnetic interactions, and although this may provide a lot of information on the partonic contents of the proton, it does not allow for detailed studies of the strong interaction. In this section, we will look at the possible first-order QCD processes that may take place in ep -scattering. The cross section presented will follow the derivation in [CES92].

Figure 3.7 shows the generic diagrams for DIS. Figures 3.7(a) and 3.7(b) show the diagrams already considered in section 3.3. The remaining diagrams in the figure show first order processes in α_s . To first order³, two types of processes are possible. Either a gluon is emitted, as shown in figure 3.7(c) and 3.7(d), or the gluon splits into a quark box that interacts with the photon. The first type is called *QCD Compton scattering*, while the latter is referred to as *Boson-Gluon Fusion (BGF)*. Where the zeroth order diagrams have one parton in the hadronic final state apart from the proton remnants, the first order processes all have two partons in the final state.

In order to simplify the situation, we refine our choice of variables further and introduce the Lorentz invariant partonic scaling variables

$$x_p \equiv \frac{Q^2}{2p_0 \cdot q} = \frac{Q^2}{2\xi P \cdot q} = \frac{x_{bj}}{\xi} \tag{3.40}$$

$$z \equiv \frac{p_0 \cdot p_1}{p_0 \cdot q}, \tag{3.41}$$

where p_0 is the momentum of the initial parton. P and q are the momenta of the proton and the photon, respectively, as previously defined, and p_1 is the momentum of one of the

³often referred to as Leading Order (LO)

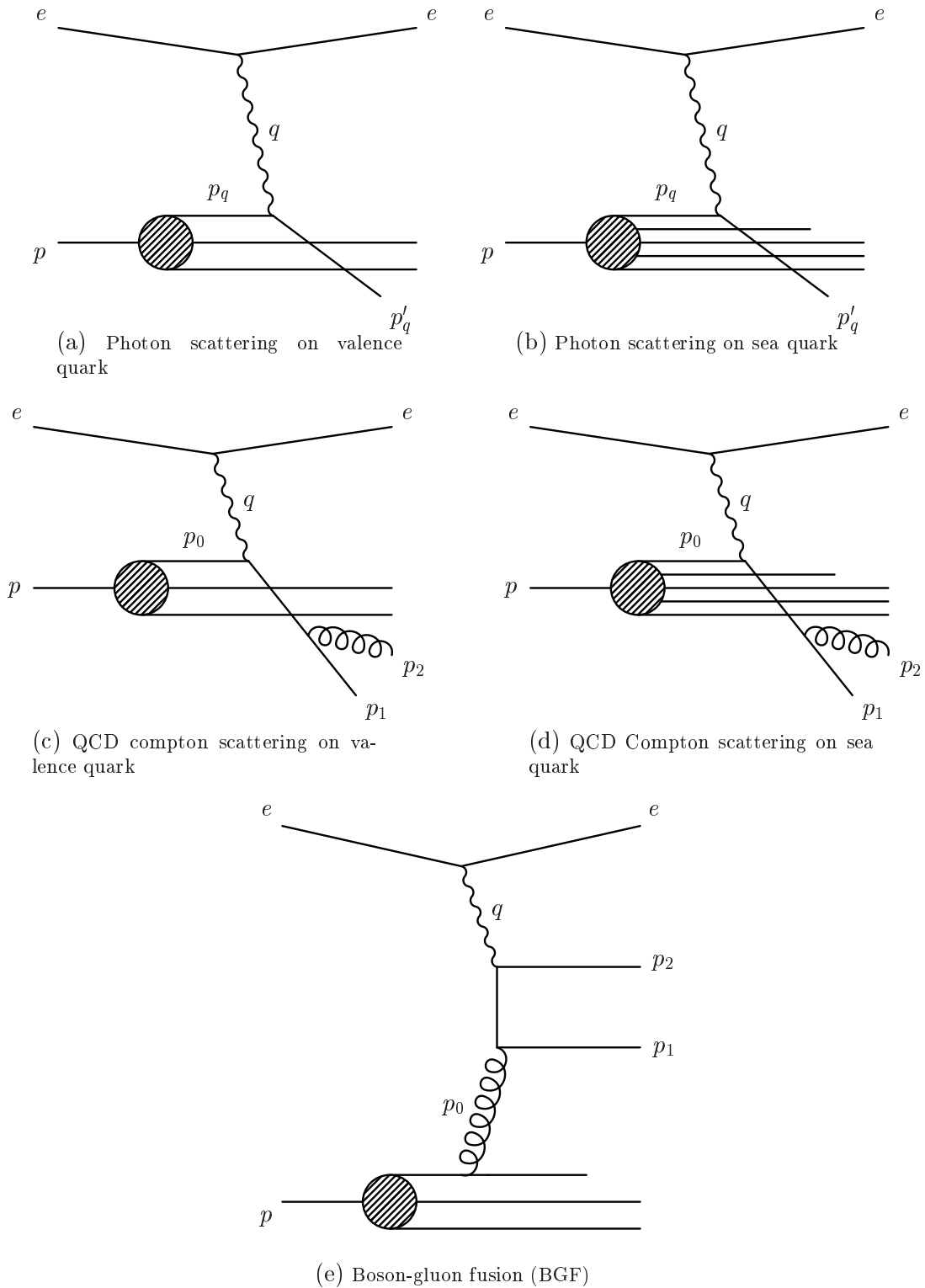


Figure 3.7: Shown here are generic diagrams of zeroth and first order processes in α_s . The diagrams are not meant to be read as Feynman diagrams in the strict sense. No distinction is made between particles and antiparticles. For full gauge invariance one also needs to include versions of the QCD Compton diagrams with gluon emission from the initial quark.

outgoing partons. The momentum of the other outgoing parton needs not be specified as knowledge of any three of p_0, q, p_1 and p_2 implies the last one due to momentum conservation. x_p is seen to be the fraction of the initial parton momentum carried by the struck parton (to leading order).

Corresponding to $p_{1,2}$, we define $P_{1,2}$ as the momenta of the observed final state hadrons. We may therefore also define z_H to be:

$$z_H = \frac{P \cdot P_1}{P \cdot q} \quad (3.42)$$

In the hadronic centre-of-mass frame (see section 3.1.2), $p_t = p_{t,1} + p_{t,2}$ of the outgoing partons is zero, if we disregard the intrinsic motion of the partons within the proton.

For massless partons, p_t is given by:

$$p_t^2 = \frac{(1-x_p)z(1-z)}{x_p} Q^2. \quad (3.43)$$

The parton cross section for the first order processes can now be written

$$\frac{d^5 \hat{\sigma}_{ij}}{dx_p dy dz d^2 p_t} = \frac{\alpha Q_q^2}{16\pi^2 Q^4} y L_{\mu\nu} M_{ij}^{\mu\nu} \times \delta \left[p_t^2 - \frac{(1-x_p)z(1-z)}{x_p} Q^2 \right], \quad (3.44)$$

where Q_q is the charge of the scattered quark. $L_{\mu\nu}$ ($M_{\mu\nu}$) is the square of the leptonic (partonic) current. $L_{\mu\nu}$ thus describes how the lepton couples to the photon, while $M_{\mu\nu}$ describes the photon coupling to the parton. Writing out $L_{\mu\nu} M_{ij}^{\mu\nu}$ for $ij = q\bar{q}$, qg and gq , the following expressions are obtained for the processes shown in figure 3.7.

$$L_{\mu\nu} M_{q\bar{q}}^{\mu\nu} = \frac{64\pi}{3} \alpha_s Q^2 \frac{(p_e \cdot p_0)^2 + (p'_e \cdot p_1)^2 + (p'_e \cdot p_0)^2 + (p_e \cdot p_1)^2}{p_0 \cdot p_2 \ p_1 \cdot p_2} \quad (3.45)$$

$$L_{\mu\nu} M_{gq}^{\mu\nu} = \frac{64\pi}{3} \alpha_s Q^2 \frac{(p_e \cdot p_0)^2 + (p'_e \cdot p_2)^2 + (p'_e \cdot p_0)^2 + (p_e \cdot p_2)^2}{p_0 \cdot p_1 \ p_1 \cdot p_2} \quad (3.46)$$

$$L_{\mu\nu} M_{q\bar{q}}^{\mu\nu} = 8\pi \alpha_s Q^2 \frac{(p_e \cdot p_2)^2 + (p'_e \cdot p_1)^2 + (p'_e \cdot p_2)^2 + (p_e \cdot p_1)^2}{p_0 \cdot p_1 \ p_0 \cdot p_2} \quad (3.47)$$

The total cross section may now be written as

$$\begin{aligned} \frac{d^5 \sigma}{dx_{bj} dy dz_H d^2 p_t} &= \sum_{i,j} dx_p dz d^2 p_t d\xi d\xi' \delta(x_{bj} - \xi x_p) \delta(z_H - \xi' z) \delta^2(P_t - \xi' p_t) F_i(\xi, Q^2) \\ &\times \frac{d^5 \hat{\sigma}_{ij}}{dx_p dy dz d^2 p_t} D_j(\xi', Q^2), \end{aligned} \quad (3.48)$$

where $F_i(\xi, Q^2)$ is the probability distribution describing an i -type parton with a fraction ξ of the proton momentum. $D_j(\xi', Q^2)$ is the probability distribution for a j -type parton to fragment producing a hadron with a fraction ξ' of the parton's momentum $P_1 = \xi' p_1$.

The equations (3.45), (3.46) and (3.47) can be written out in coordinates. This is done in [Jac94], but has not been included here. In this process, one sees that singularities arise as $x_p \rightarrow 1$, $z \rightarrow 1$ or $z \rightarrow 0$ resulting in a divergence of the total cross section. These calculations

are therefore not safe in the region of very soft or collinear gluon emissions. By introducing a p_t -cut-off, the divergent regions are avoided.

For large virtualities and correspondingly small values of α_s the dynamics is totally dominated by zeroth and first order processes as described here. However as the virtualities decrease and α_s rises higher order effects must be taken into account.

At present DIS is only described up to next-to-leading order (NLO), as higher order calculations are too complex. A variety of approximation methods are used to take higher order effects into account without performing the full calculation.

Some of these methods will be described in chapter 4.

Chapter 4

DIS Processes and QCD Evolution Schemes

As described in Chapter 2, QCD is an asymptotically free theory. We can refine predictions of the theory by considering higher and higher orders of expansions in α_s as long as $Q^2 \gg \Lambda_{QCD}^2$. This road turns out to be a rocky one. The complications of the calculations rise drastically as soon as one attempts calculations beyond leading order (LO). The DIS-processes have been described to Next-to-Leading Order (NLO). Higher order solutions do not seem realistic to work out at this point, although NNLO-calculations exist for some processes.

In DIS at HERA, interactions occur at very high energies. This leaves a large phase space for parton emissions. Higher order effects of QCD therefore plays a large role. The proton and the lepton interacts through a complicated cascade of partons at varying scales.

An approach to enhancing the predictive power of QCD is the concept of *resummation*. It turns out that one can expand the structure functions in the kinematic variables of the process, and that this expansion is equivalent to the full summation of certain classes of diagrams. We can in other words regard resummation schemes as calculations *of an arbitrarily high order* in which we restrict ourselves to only considering certain types of processes.

Such an approach has of course certain disadvantages compared with analytical calculations.

- Predictions will generally *not* be gauge-invariant, since this requires *all* processes with the same initial and final state to be taken into account (to the required order).
- Depending on the evolution parameter, there will be regions in phase space that are described better than others.

However, there is a hope that regions of phase space may be identified in which the different approaches can be seen to have physical significance.

In the following, I will describe four of these schemes as well as their expected region of validity. The models are embodied in Monte Carlo event generators that have been used in the analysis. These generators will be treated in chapter 5.

4.1 DGLAP

In this section I will present the DGLAP (Dokschitzer, Gribov, Lipatov, Altarelli, Parisi) evolution equations ([GL72], [Lip75], [AP77], [Dok77]). These equations provide a foundation for treating parton splittings for the case when Q^2 is very large.

A fundamental assumption in the QPM is that the intrinsic motion of the partons in the protons may be neglected, and that we may consider the quarks to have zero transverse momentum. This is not true in QCD. Quarks and gluons are in permanent interaction and explicitly gluons may be emitted at any point in time leading to large transverse momenta k_t of the quarks.

Doing detailed calculations of the corrections to the quark distribution functions (see section 3.3.1) from gluon emission one obtains

$$q(x, \mu^2) = q_0(x) + \frac{\alpha_s}{2\pi} \int_x^1 \frac{d\xi}{\xi} q_0(\xi) \left[P\left(\frac{x}{\xi}\right) \ln \frac{\mu^2}{\kappa^2} + C\left(\frac{x}{\xi}\right) \right] + \dots \quad (4.1)$$

x is the fraction of the proton momentum carried by the parton. This x needs not be the x_{bj} of a scattering process, as the q -distribution is not a physical observable (see figure 4.1). The distribution function is given not only as a function of x . A scale μ^2 is also included. μ^2 is known as the *factorisation scale*, and it results from the treatment of the collinear divergence of the matrix element for gluon emission. $q_0(x)$ plays the role of the unmeasurable *bare* distribution. $P(x)$ is known as the *splitting function* and is defined as

$$P(x) = \frac{4}{3} \frac{1+x^2}{1-x}$$

Its form is specific to the $q\bar{q}g$ -vertex and it will be interpreted later.

F_2 can now be obtained using equation (3.39):

$$F_2(x_{bj}, Q^2) = x_{bj} \sum_{q, \bar{q}} e_q^2 \int_{x_{bj}}^1 \frac{d\xi}{\xi} q(\xi, \mu^2) \left[\delta\left(1 - \frac{x_{bj}}{\xi}\right) + \frac{\alpha_s}{2\pi} P\left(\frac{x_{bj}}{\xi}\right) \ln \frac{Q^2}{\mu^2} + \dots \right] \quad (4.2)$$

As a direct consequence of QCD, it is now seen, that F_2 does *not* scale. Bjorken scaling is logarithmically broken. This does not express that quarks and gluons are not point-like. Rather it is a consequence of the transition from the QPM picture to the more dynamic description of QCD.

Note here that we do *not* know the parton distribution functions. They must include contributions from the non-perturbative regimes of the theory, and they are therefore not calculable from perturbation theory. They have to be measured by experiment.

We now define a variable $t = \mu^2$ and take the derivative of (4.2) with respect to $\ln t$. There is no t -dependence on the left-hand side, so the derivative is zero. As for the sum that results on the right-hand side, it is seen that any t -dependence there may be in the individual terms *should be the same* due to flavour invariance of QCD (we ignore the masses of the quarks). The sum is now a vanishing sum of identical quantities, so all terms must vanish identically. The DGLAP evolution equation now results:

$$\frac{dq(x, t)}{d \ln t} = \frac{\alpha_s(t)}{2\pi} \int_x^1 \frac{d\xi}{\xi} P\left(\frac{x}{\xi}\right) q(\xi, t) \quad (4.3)$$

The left-hand side of (4.3) arises from integrating over the δ -function in equation (4.2), whereas the right-hand side rests upon the assumption that the only explicit $\ln t$ -dependence in the expansion comes from the $\ln \frac{Q^2}{t}$ -term. Note that x has been substituted for x_{bj} , as the equation should describe the evolution of a parton cascade (figure 4.1) with varying x -values.

This is of course not a very rigorous treatment, as we have ignored the t -dependence of α_s as well as of $q(\xi, t)$ inside the integral. A more formal treatment is based on operator product expansion (OPE), and may be found in [GP74], [GW74], or in [PS]. This treatment confirms equation (4.3) and gives the full prediction as a $2n_f + 1$ -dimensional matrix equation

$$t \frac{\partial}{\partial t} \begin{pmatrix} q_i(x, t) \\ g(x, t) \end{pmatrix} = \frac{\alpha_s(t)}{2\pi} \sum_{q_j, \bar{q}_j} \int_x^1 \frac{d\xi}{\xi} \begin{pmatrix} P_{q_i q_j} \left(\frac{x}{\xi}, \alpha_s(t) \right) & P_{q_i g} \left(\frac{x}{\xi}, \alpha_s(t) \right) \\ P_{g q_j} \left(\frac{x}{\xi}, \alpha_s(t) \right) & P_{g g} \left(\frac{x}{\xi}, \alpha_s(t) \right) \end{pmatrix} \begin{pmatrix} q_j(x, t) \\ g(x, t) \end{pmatrix}, \quad (4.4)$$

where the quark distribution function has been replaced with the general parton distribution functions. The splitting functions now have a physical interpretation. The leading order DGLAP splitting function $P_{ab}^{(0)}(x)$ is the probability of finding a parton of type a in a parton of type b with a fraction x of the longitudinal momentum of the parent parton and a transverse momentum squared much less than μ^2 ([ESW96] p. 109).

For a physical interpretation of the DGLAP equation, we consider a situation in which the electron scatters off the proton in a reaction fulfilling $Q^2 \gg m_p$. Considering a parton in the proton, it may either be a real parton or a result of an emission with some virtuality t . In each parton branching, the virtuality of at least one of the partons has to increase, and we may therefore regard the DGLAP scenario as a series of parton splittings with a strong ordering in virtuality from Q^2 and steeply falling, moving from the photon side to the proton side, as depicted in figure 4.1

As the virtuality of a parton may be written as [Dav01]:

$$t = \frac{k_t^2}{1 - x_n}$$

This ordering translates directly into a requirement by DGLAP on the transverse parton dynamics of the propagators. These dynamics can be expressed as

$$k_{t_0}^2 \ll k_{t_1}^2 \ll \dots \ll k_{t_{n-1}}^2 \ll k_{t_n}^2. \quad (4.5)$$

By momentum conservation in the individual vertex, we arrive at the conclusion that the DGLAP equation effectively implies a cascade-like picture of (predominantly) gluon emissions as depicted in figure 4.1. In this cascade the emissions are strongly ordered in transverse momentum.

This behaviour predicted by DGLAP including k_t -ordering and scaling violation of F_2 has been experimentally confirmed in the $\ln Q^2 \gg \ln(1/x)$ -regime (example: [H194]).

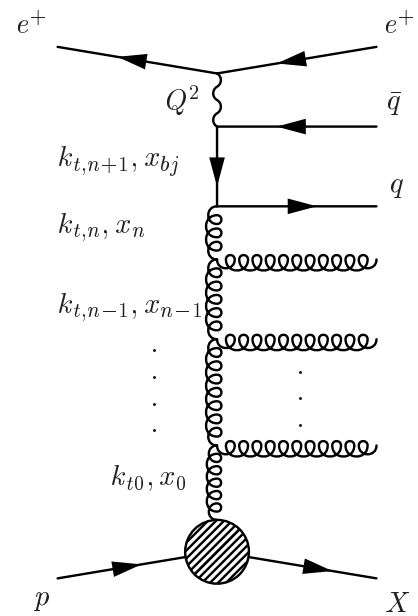


Figure 4.1: Gluon cascade.

4.2 BFKL

DGLAP evolution has its region of validity in the regime where $\ln Q^2 \gg \ln(1/x)$. This is due to the fact that it effectively resums the $[\alpha_s \ln Q^2]^n$ -terms in the full QCD-expansion. However, there are also terms of $[\alpha_s \ln 1/x]^n$ that may contribute. In the kinematic regime, where $\ln Q^2 \ll \ln(1/x)$ it is therefore necessary to select another approach.

Resummation of the $\ln 1/x$ -terms was first done by Balitsky, Fadin, Kuraev and Lipatov ([KLF76],[KLF77],[BL78]), and the result may be expressed in the BFKL equation (in the form given in [ESW96]):

$$\frac{\partial \mathcal{G}(x, k_t^2)}{\partial \ln 1/x} = \int d^2 k'_t K(\vec{k}_t, \vec{k}'_t) \mathcal{G}(x, k_t'^2) \quad (4.6)$$

Looking at a particular vertex, the primed quantities represent the daughter parton, and the non-primed the mother. The details of the splitting dynamics are governed by the *BFKL splitting kernel*, $K(\vec{k}_t, \vec{k}'_t)$, and the function \mathcal{G} is the *unintegrated gluon density* fulfilling

$$xg(x, Q^2) \simeq \int_0^{Q^2} dk_t'^2 \mathcal{G}(x, k_t'^2), \quad (4.7)$$

where $g(x, Q^2)$ is the total proton gluon density.

BFKL-evolution represents a ladder of parton splittings, as shown in figure 4.1, where the emissions are ordered in x instead of k_t :

$$x_0 \gg x_1 \gg \dots \gg x_{n-1} \gg x_n \quad (4.8)$$

with x_{bj} setting the lower limit. This can be interpreted as the assumption that an emitted gluon tends to carry a large fraction of the momentum of the propagating gluon.

On the other hand, there is no requirement on the transverse momentum, which may vary randomly. This means that while both DGLAP and BFKL predicts the emission of a gluon cascade, their predictions on the transverse dynamics is very different. In other words it should be possible to disentangle the two types of dynamics, by applying the right cuts on the transverse momenta in the hadronic final state. This is exactly what is attempted in the present analysis.

4.3 CCFM

The CCFM (Catani, Ciafaloni, Fiorani, Marchesini) equation ([Cia88], [CFM90a], [CFM90b], [CCH91]) imposes the requirement on the parton cascade that parton emissions in the initial cascade only take place in an angular ordered region of phase space. CCFM reproduces as well DGLAP as BFKL behaviour in the appropriate limits. CCFM evolution is used in the Monte Carlo event generator CASCADE.

The requirement of angular ordering stems from considerations of *colour coherence*. The maximum allowed angle is denoted Ω , and it is determined by the quark box connecting the photon to the gluon.

Decomposing the gluon momenta in components parallel with and perpendicular to the proton direction, the four-momenta p_i of the emitted gluons may be written [JS01]

$$p_i = \underbrace{y_i(p_p + \omega_i p_e)}_{p_{\parallel i}} + p_{ti}, \quad \omega_i = \frac{p_{ti}^2}{s y_i^2}, \quad (4.9)$$

where $y_i = (1 - z_i)x_{i-1}$ and $x_i = z_i x_{i-1}$. ω_i is thus connected to the angle of the emitted gluon with respect to the proton. x_i and y_i are the momentum fractions of the exchanged and emitted gluons. z_i is the momentum fraction in the branching $(i - 1) \rightarrow i$, i.e. the fractional energy transfer between the $i - 1$ st and the i th exchanged gluon. p_{ti} is the transverse momentum of the emitted gluon.

Angular ordering translates to

$$\omega_0 < \omega_1 < \dots < \omega_n < \Omega \quad (4.10)$$

or

$$z_{i-1} q_{i-1} < q_i, \quad (4.11)$$

where q_i is the rescaled transverse momentum of the emitted gluons defined by

$$q_i = x_{i-1} \sqrt{s \omega_i} = \frac{p_{ti}}{1 - z_i}. \quad (4.12)$$

When generating a parton cascade, the quantity of interest is the splitting function. The CCFM splitting function is given by ([Cia88], [CFM90a], [CFM90b]):

$$dP_i = \tilde{P}_g^i(z_i, q_i^2, k_{ti}^2) \Delta_s dz_i \frac{d^2 q_i}{\pi q_i^2} \Theta(q_i - z_i q_{i-1}) \Theta(1 - z_i - \epsilon_i) \quad (4.13)$$

where the Θ -function has the conventional definition:

$$\Theta(x) = \begin{cases} 0 & , x < 0 \\ 1 & , x \geq 0 \end{cases} \quad (4.14)$$

$\Delta_s(q_i, q_{i-1})$ is the *Sudakov form factor*, which may be interpreted as the probability for a parton at the scale q_{i-1} to “survive” to the scale q_i [ESW96]. It is often referred to as the *probability of non-emission*. An expression for Δ_s is found in [JS01].

Colour coherence effects are taken into account by the angular ordering imposed by the first Θ -function in equation (4.13).

The gluon splitting function is given by [JS01]:

$$\tilde{P}_g^i = \frac{\bar{\alpha}_s(q_i^2(1 - z_i)^2)}{1 - z_i} + \frac{\bar{\alpha}_s(k_{ti}^2)}{z_i} \Delta_{ns}(z_i, q_i^2, k_{ti}^2) \quad (4.15)$$

where $\bar{\alpha}_s = \frac{3\alpha_s}{\pi}$.

Δ_{ns} is the *non-Sudakov* form factor that counters the $1/z$ singularity in the splitting function. An expression of Δ_{ns} may be found in [JS01].

Having introduced some of the formalism, the CCFM equation is given in equation (4.16) as an integral equation ([Mar95], [BMSS98], [KMS95]):

$$\mathcal{A}(x, k_t, \bar{q}) = \mathcal{A}_0(x, k_t, \bar{q}) + \int \frac{dz}{z} \int \frac{d^2q}{\pi q^2} \Theta(\bar{q} - z\bar{q}) \Delta_s(\bar{q}, zq) \tilde{P}(z, q, k_t) \mathcal{A}\left(\frac{x}{z}, k'_t, q\right) \quad (4.16)$$

where $k'_t = |\mathbf{k}_t + (1 - z)\mathbf{q}|$, and \mathbf{k}_t and \mathbf{q} are two-dimensional vectors. \bar{q} is the upper scale for the last angle of emission:

$$\bar{q} > z_n q_n, \quad q_n > z_{n-1} q_{n-1}, \quad \dots, \quad q_1 > Q_0 \quad (4.17)$$

The \mathcal{A} in equation (4.16) is the unintegrated gluon density, defined according to [Jun02b]:

$$xg(x, \bar{q}) \simeq \int_0^{\bar{q}^2} dk_t^2 x \mathcal{A}(x, k_t^2, \bar{q}) \quad (4.18)$$

4.4 CCFM vs. BFKL

The CCFM equation as well as the BFKL equation are known to reproduce the correct leading logarithms in the small- x limit for all final state observables ([FSV98], [Web98], [Sal99]). It would therefore seem obvious to implement BFKL in a Monte Carlo generator. This approach, however, runs into a number of problems.

Using x as the evolution parameter introduces a dependence on the infrared (soft) cut-off [Sal99]. The rapidity can also be used as the evolution parameter. This fixes the problem with the cut-off-dependence, but introduces a new problem [JS01]. This problem can be seen from the fact that DGLAP, CCFM and BFKL with x as the evolution parameter all predict F_2 at small x and large Q^2 to behave as:

$$F_2(x_{bj}, Q^2) \sim \exp\left(2\sqrt{\bar{\alpha}_s \ln Q \ln 1/x_{bj}}\right) \quad (4.19)$$

Using rapidity as the evolution parameter in BFKL, however, F_2 is predicted to behave as:

$$F_2(x_{bj}, Q^2) \sim \exp\left(2\sqrt{\bar{\alpha}_s \ln Q \ln 1/x_{bj} + \bar{\alpha}_s \ln^2 Q}\right) \quad (4.20)$$

The CCFM equation does not suffer from these problems. Furthermore, it is seen in the DGLAP limit that the angular ordering of CCFM translates into an ordering in q , reproducing DGLAP dynamics. CCFM therefore forms a better basis for an implementation in a Monte Carlo generator.

4.5 The Colour Dipole Model (CDM)

Another model for higher order QCD radiation needs to be mentioned here. In the Colour Dipole Model (CDM) ([Gus86], [GP88]), the parton cascades are modelled from the assumption that emissions take place from the formation of colour dipoles spanned by quarks and

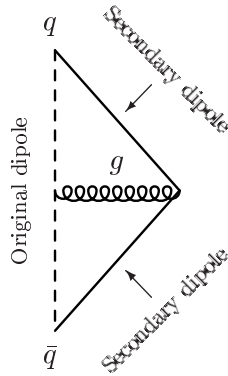


Figure 4.2: A primordial colour dipole spanned by a $q\bar{q}$ -pair emits two secondary dipoles by the emission of a gluon.

antiquarks. When the primordial dipole emits a gluon, this gluon carries colour charge by itself, producing a “kink” in the dipole as shown in figure 4.2. This leads to the formation of secondary dipoles of quarks and gluons which may in turn produce more dipoles independently. The only constraint is that k_t decreases at each radiation of new dipoles. It should be emphasised that this is *not* the same as the strong k_t -ordering of DGLAP. It is simply the observation that the primordial dipole “contains” the highest transverse momenta, and that subsequent emissions must fall between the two partons of the dipole.

In CDM there are three fundamental types of dipoles that may radiate. These are shown in figure 4.3.

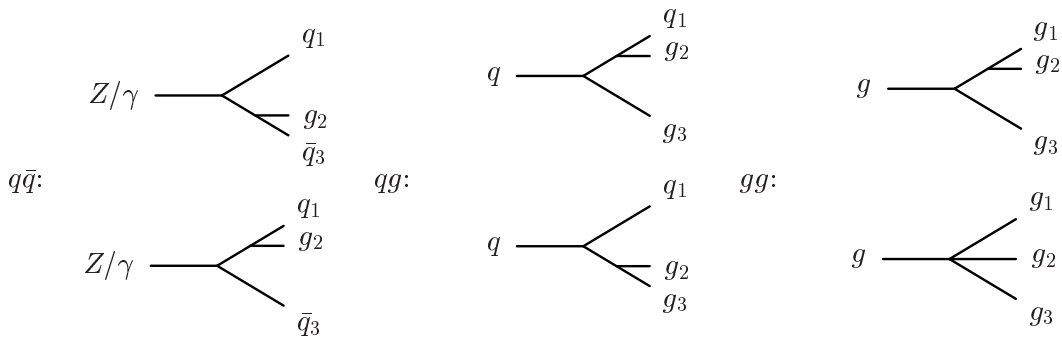


Figure 4.3: Dipole types in the Colour Dipole Model.

The radiation of a gluon from a dipole of mass W is therefore described in terms of three fundamental cross sections: $\frac{d\sigma_{q\bar{q}}}{dx_1 dx_3}$, $\frac{d\sigma_{qg}}{dx_1 dx_3}$ and $\frac{d\sigma_{gg}}{dx_1 dx_3}$, where the x_i are the final state energy fractions $2E_i/W$ of the emitting partons in the dipole CMS. As three partons take part in the emission, two of the x_i need to be specified. All three cross sections are well approximated by [Lon92]

$$d\sigma \propto \alpha_s \frac{dp_t^2}{p_t^2} dy, \quad (4.21)$$

where p_t, y are the transverse momentum and rapidity of the emitted gluon with respect to the total dipole momentum.

Considering this concept applied to DIS, the first dipole is created by the scattered quark and the proton remnant. The available phase space can be roughly represented as a triangle in the $(y, \ln p_t^2)$ plane as shown in figure 4.4.

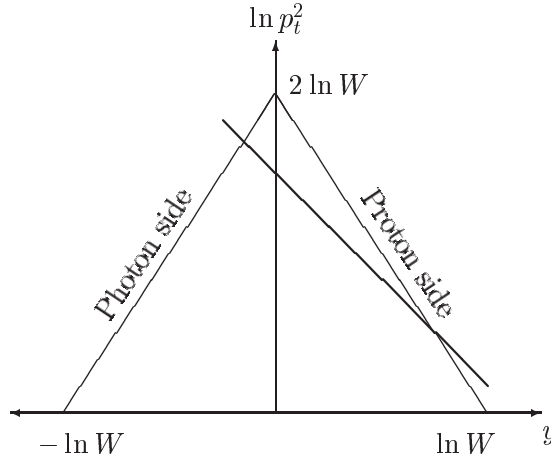


Figure 4.4: *Phase space for DIS in CDM.*

Since the proton remnant is treated as an extended object, there is an additional reduction of the phase space for gluon emission due to the fact that a gluon can only access a fraction of the momentum carried by the remnant [Lon99]. The effect can also be understood as a suppression of the radiation of small wavelengths from an extended antenna. The suppression is indicated by the line in the diagram above. Treating the photon as an extended object with associated parton density functions introduces a similar suppression on the photon side.

CDM is a highly tunable model, and it is often used to correct for detector effects. It is implemented in the Monte Carlo event generator ARIADNE.

Chapter 5

Monte Carlo Event Generation

In most data analyses in physics, the measurement of physical observables from a particle detector have to be compared with the predictions from different theories or models. These are usually implemented in so-called Monte Carlo generators, which provide a specific description of processes under investigation. In this analysis, the following three generators have been used:

- **ARIADNE v. 4.08 (CDM)**
This generator has been used to correct for detector effects, as it turns out to describe the forward jet cross section fairly well.
- **RAPGAP v. 2.8 + 3.0 (DGLAP + Resolved photon)**
This event generator has been used to compare pure DGLAP evolution applied for the forward jet case.
- **CASCADE v. 1.2 (CCFM)**
As this generator embodies CCFM evolution it is a good candidate to describe parton dynamics, where DGLAP in the form of RAPGAP fails.

I will here present these generators with a short description of the method of event generation. It is here important to remember, that CDM (as embodied in ARIADNE) is a highly tunable model, that is often used for detector corrections. However, it gives little information in the context of parton dynamics. DGLAP and CCFM, on the other hand, are models based on a well defined theoretical approach, and they contain fewer parameters. DGLAP relies on the choice of factorisation scale μ^2 , and CCFM (as implemented in CASCADE) relies on three parameters as will be described in section 5.2. The resolved photon model is also a model which contains many parameters, introducing a complete set of parton density functions for the photon as will be mentioned in section 5.1.

5.1 RAPGAP

The RAPGAP Monte Carlo event generator [Jun95] is designed specifically to describe DIS as well as diffractive scattering. The Monte Carlo generator implements the zeroth and first

order matrix elements of QCD to generate the hard sub-process (Q^2) itself. The parton shower is then generated using a backwards evolution scheme, starting at the photon side of the scattering and iterating successive branchings towards the proton side. This is done under the requirement of a strict ordering in virtuality of the propagator, and hence k_t , as described in section 4.1. The iteration process continues until a cut-off Q_0 is reached as shown in figure 5.1(a). Final state parton showering and fragmentation is treated with the Lund String Model [And97] (see section 6.2) as implemented in JETSET ([Sjo86], [SB87], [Sjo94]). RAPGAP is also capable of using CDM (section 4.5) instead of DGLAP.

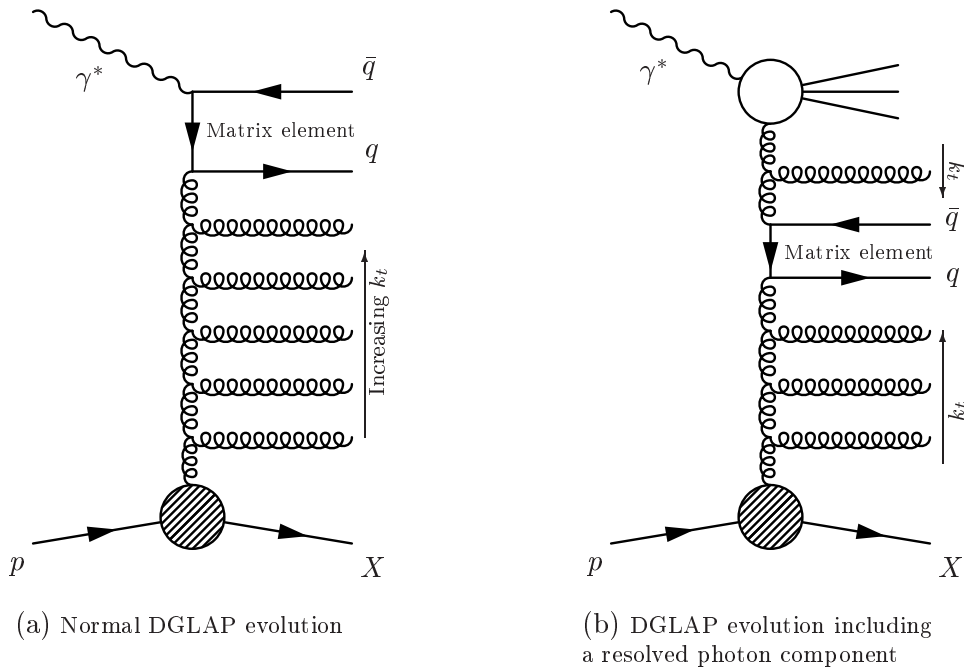


Figure 5.1: *Parton evolutions.*

RAPGAP includes the possibility of treating the photon as a resolved object with corresponding parton density functions according to the *Resolved photon model* ([Jun95], [JJK98]). In this model the hard scale of the process needs not be on the photon side of the ladder. The implementation is accomplished by adding another DGLAP evolution starting at the hard scale and limited by the virtuality of the photon. The resolved photon approach is shown in figure 5.1(b).

In the remainder of this thesis “RAPGAP DIR” will be referring to RAPGAP using standard DGLAP, with a renormalisation and factorisation scale of $\mu^2 = p_t^2 + Q^2$.

“RAPGAP DIR+RES” will be referring to RAPGAP including a resolved photon component. The virtual photon has been parametrised using the SaS photon structure function [SS96].

In the analysis, two versions of the RAPGAP program have been used. For corrections we used a sample of detector simulated and reconstructed RAPGAP 2.8 (DIR). For comparison between data and Monte Carlo, RAPGAP 3.0 generated through the HzTool framework [B⁺] was used.

5.2 CASCADE

As described in section 4.4, there are problems involved with building a BFKL-based event generator. Therefore, CASCADE [Jun02a] has been used in this analysis. CASCADE embodies CCFM evolution in combination with zeroth and leading order matrix elements.

In analogy with RAPGAP, CASCADE generates the hard scattering from QCD matrix elements. Parton showering is then added, using a backward evolution scheme. In this scheme, the starting point is the quark box with an upper angle Ω . From here, the program goes successively down the ladder until the proton side is reached. This is done under the requirement of angular ordering imposed by the CCFM equation.

The unintegrated gluon density $x\mathcal{A}(x, k_t^2, \bar{q})$ (see section 4.3) is obtained from a forward evolution procedure using the forward evolution Monte Carlo program SMALLX ([MW91], [MW92]). As the CCFM equation is quite complicated, the gluon density is not parametrised. Instead, it is calculated on a grid in $\log x$, $\log k_t$ and $\log \bar{q}$ [JS01]. The three input parameters have been fitted to $F_2(x, Q^2)$ as measured by the H1 and ZEUS experiments [HJ03].

Two sets of unintegrated gluon densities have been used in the analysis. These are *J2003 set 1* and *J2003 set 2* [HJ03]. The difference between these two sets is that Set 2 progresses to a soft k_t -scale of 1.18 GeV, whereas Set 1 cuts off at 1.33 GeV. Furthermore, Set 2 includes the full gluon splitting function. Contrary to equation (4.15), non-singular terms are included that have been ignored in other implementations. It is therefore of interest to see if this more complete treatment of the splitting function and the associated gluon density changes the predictions of CCFM.

CASCADE v. 1.2 using J2003 Set 1/2 will henceforth be referred to as CASCADE J2003 Set 1/2 or simply CASCADE Set 1/2.

5.3 ARIADNE

The ARIADNE Monte Carlo generator [Lon92] implements CDM in the treatment of parton showers. As described in section 4.5, the initial dipole is formed by the scattered parton and the proton remnant. This dipole now successively emits more dipoles without requirement of k_t -ordering. This is shown in figure 5.2.

ARIADNE contains a native description of the QCD Compton processes (figure 3.7 p. 26), whereas the boson-gluon fusion process (BGF) must be included “by hand”. This is accomplished by the use of a matching procedure on the first emission in the event [Lon92]. The primordial dipole spanned by the struck quark and the proton remnant may either emit a gluon according to the corresponding matrix element (including the phase space suppression from section 4.5) or “emit” the anti-partner of the struck quark according to the BGF matrix element, constructing a quark box.

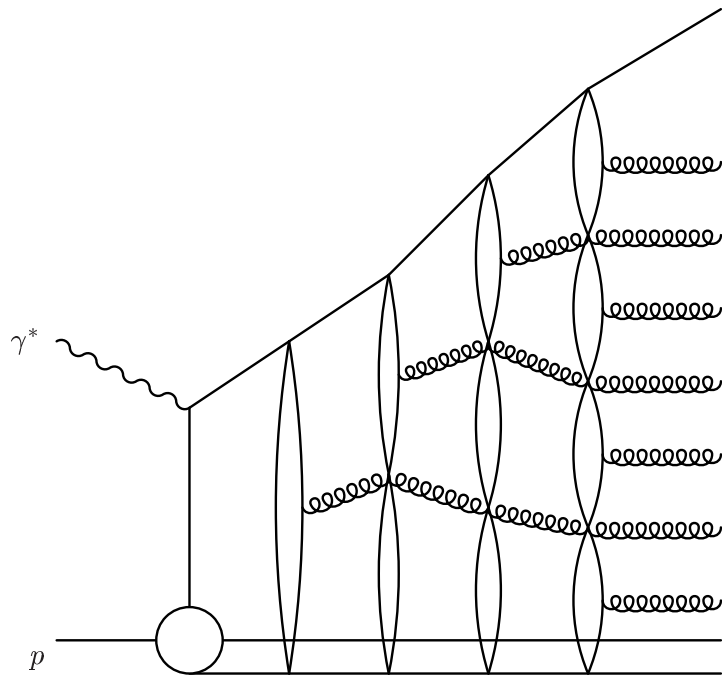


Figure 5.2: *QCD radiation in CDM as implemented in ARIADNE.*

Chapter 6

Jet Physics

One of the most direct pieces of experimental evidence for the existence of quarks is the jet phenomenon. In this chapter, I will give a brief introduction to jets. What they are, and how to reconstruct them.

6.1 Colour Confinement and the Jet Phenomenon

As discussed in chapter 2, QCD exhibits asymptotic freedom in the high energy limit. It was also mentioned how perturbation theory breaks down due to a divergence of the strong coupling constant as energies approach $\Lambda_{QCD} \approx 200$ MeV. As no free quarks and gluons have ever been observed, this is said to be the consequence of *colour confinement*.

This leads to the notion that quarks and gluons are to be regarded as field excitations in the asymptotic limit, where they can be treated as being free. The concept of a quark or a gluon loses its meaning as the energy scale decreases.

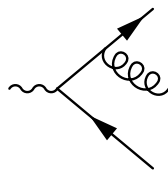


Figure 6.1: *Emission of three partons. This situation is typical for a high energy real boson decay as for example a W^\pm or a Z^0 .*

We now consider the emission of a high energy parton as shown in figure 6.1. Each of the three shown partons may carry a large fraction of the original boson energy.

In the time span from the initial parton emission to the final state particles are formed, these particles undergo a series of fragmentations, each reducing the energy per particle until the energy is so low that the non-perturbative nature of confinement sets in, and hadrons are formed.

The final state particles may form a very complex state consisting of any number of photons, leptons and light hadrons. Due to momentum conservation, the momenta of the decay products from, say, a quark should add up to reconstruct the original quark momentum.

For high energy parton decays, this will lead to a collimated flow of final state particles in the detector. This is called a *jet*. Looking at a particular high-energy quark fragmenting, the first emission of a gluon is restricted in p_{\perp} (relative to the quark direction of motion) by Λ_{QCD} to be ~ 1 GeV. All subsequent emissions have lower p_{\perp} , while the forward momentum suffers no such constraint. The higher the energy content of the reaction, the better the jets are defined, as the ratio $\frac{p_{\perp}}{p_{\parallel}}$ decreases.

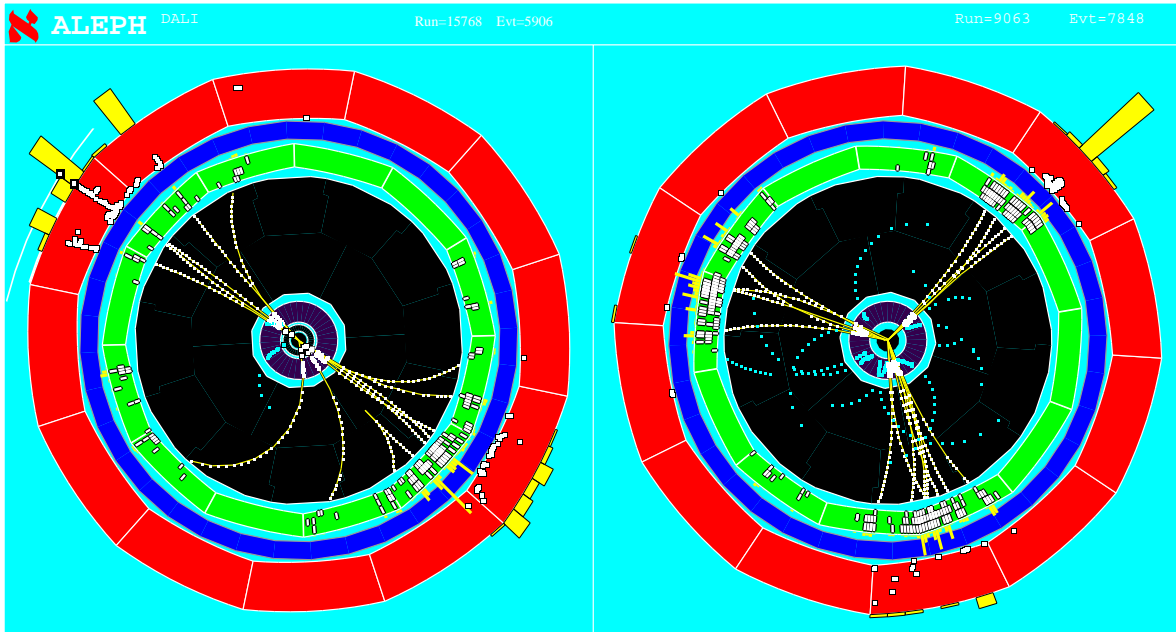


Figure 6.2: A two jet event and a three jet event from the ALEPH experiment [8b] at CERN. The events are interpreted as a Z^0 decaying to two quarks. In the right picture, one of the quarks has emitted a gluon as in figure 6.1.

Figure 6.2 shows two jet events recorded with the ALEPH detector at CERN. Note how the opening angles of the jets are very small, indicating a very high energy of the original partons.

6.2 The Lund String Model

The above description of fragmentation is not complete. Both quarks and gluons carry colour charge, whereas the final state particles must be colour neutral due to colour confinement. In other words, there must be a colour flow between decay products of *different* initial state partons. This in turn leads to correlations in the fragmentation that are described in the *Lund String Model* (LSM) [And97].

In the LSM, the partons in the initial state are connected with so-called strings. These strings are to be viewed as a non-perturbative aspect of QCD. They are *colour flux tubes* which exchange the colour needed to ensure colour neutral final state hadrons.

Inherent in the LSM is a prediction of correlations in the fragmentation. A string “tension” is defined, and new particles are the result of a string breaking in two. Fragmentation of the partons is thus equivalent to fragmentation of the strings. For the example in figure 6.3, this

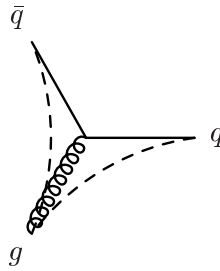


Figure 6.3: *Strings in a $q\bar{q}g$ -configuration. This is the event plane as seen in the Centre-of-Mass frame. It is not a Feynman diagram.*

leads to enhanced particle production between the quarks and the gluon relative to the region between the quarks.

The string effect is well supported by experiment ([Na], [JA81], [JA83]) and the LSM is implemented in JETSET ([Sjo86], [SB87], [Sjo94]). JETSET is today regarded as a standard tool to simulate final state parton showering and fragmentation. Other models of fragmentation exist. The most well-known is the HERWIG cluster model [Kup98].

6.3 Finding Jets

If jets are to be manifestations of the original partons, there is no unique way to determine which particles belong to a jet. In the three jet event in figure 6.2, it is seen that there are some soft emissions that can not in a sensible way be assigned to either one of the jets without ambiguity. This ambiguity is already caused by the underlying physics. The hadronisation process is not independent in both jets, as e.g. in the LSM model both sides are connected by a colour flux tube.

To consistently reconstruct jets, *jet algorithms* have been defined to prescribe how particles close in phase space should be combined into jets. These algorithms do not guarantee the accurate reconstruction of the underlying partons in the final state. Rather they ensure that all jets are reconstructed in a consistent way. Different algorithms will generally give different results. It is therefore important to use the same jet algorithm on data and on hadron level Monte Carlo, in order to make a comparison.

Jet algorithms divide into two main groups: The so-called cone algorithms and the clustering algorithms

The Cone algorithms rely on the idea that a jet can be characterised as a concentration of transverse energy in a cone of radius R in (η, ϕ) -space [AC99]. In the algorithm, all particles within a radius R_0 ,

$$R = \sqrt{(\Delta\eta)^2 + (\Delta\phi)^2} \leq R_0 \quad (6.1)$$

are combined into a jet of transverse energy E_t

$$E_t = \sum_{i\text{th part. in cone}} E_{t_i}, \quad (6.2)$$

and a new jet axis is defined. This procedure is then applied over a number of iterations until the quantities are fixed.

Using $\Delta\eta$ instead of $\Delta\theta$, a jet measure is obtained, which is invariant under longitudinal boosts.

The specifics on how to define, merge and disregard jets vary from implementation to implementation.

Cone jets have traditionally been the canonical choice in hadronic collisions, as the centre of mass of the hard scattering process is typically boosted with an unknown amount. Furthermore, hadronic collisions will typically include a lot of soft activity from spectator partons such as the proton remnant in DIS. The “pollution” of the jets from these underlying event quantities is to a large extent determined by geometry and is thus easily estimated.

Clustering algorithms are based on grouping particles together according to a metric [ES93]. Particles with “nearby” momenta are defined as belonging to the same jet, and a pseudo particle is defined from the two. This pseudo particle then goes into the clustering as the regular particles.

The clustering typically continues until all particles above a certain momentum threshold belong to a pseudo particle or are too far away from anything else in the event to be merged into a pseudo particle. The surviving pseudo particles are then taken as the jets.

An advantage of clustering algorithms is that they are rotationally invariant. They are thus well fitted to describe jet production in for example e^+e^- -collisions, where the CMS coincides with the laboratory frame.

For hadronic collisions, the drawback is that most clustering schemes assume everything in an event to be of interest, thus including all particles in the hadronic final state in a jet. In hadronic collisions this is not a good assumption. The typical object of study is parton-parton or photon-parton scattering. Apart from the hard scattering process there is a lot of activity near the beam pipe due to the fragmentation of the spectator partons.

In the present analysis, the *inclusive k_t -algorithm* ([ES93], [CDSW93]) has been used. For that reason this is the only jet algorithm that I will describe in detail.

6.4 Choice of Jet-Algorithm

A study of a number of jet-algorithms applied to DIS was presented in [Kar02]. The study consisted of a detailed investigation of how hard partons at the matrix element level were reconstructed after parton showering and after hadronisation.

The jet-algorithms were compared according to a number of criteria describing the deviations in invariant mass and momentum direction between the three levels. This was done as a function of the jet resolution parameters of the individual jet-finders.

A number of quantities were defined and measured to this end. The measurements were carried out on a RAPGAP event sample which was divided into a number of sub-samples containing different types of physics such as diffraction, QCD-Compton processes or BGF events. The jet algorithms were in this way tested on a wide variety of physics signatures to make the conclusions as universally valid as possible. The conclusion was that the CDF-CONE algorithm and the inclusive k_t -algorithm showed the best performance judged on the ability to reconstruct the parton characteristics. There was a tendency in many of the parameters

studied for the two to be very alike. The inclusive k_t -algorithm was not as good as the CDF-CONE algorithm in describing the direction of very soft jets, but for harder jets ($\sim 2-3$ GeV) the inclusive k_t -algorithm in general showed smaller mean deviations in (η, ϕ) -space than the CDF-CONE algorithm. This is a main reason that it has been used in the present analysis.

6.5 The Inclusive k_t -Algorithm

The inclusive k_t -algorithm ([ES93], [CDSW93]) is an attempt to define a clustering algorithm in a way that makes good sense for hadron-hadron collisions. The resulting algorithm is a clustering scheme by nature, but it shares many features with cone jets.

The algorithm was originally defined for hadron hadron collisions in the CMS. As this frame has no direct equivalent in DIS, it has here been executed in the Breit frame (see p. 19).

The hadronic final state is seen as consisting of a set of ‘‘protojets’’ i with momenta p_i^μ . As protojets are taken the individual particles in the hadronic final state. The masses $\sqrt{p_i^\mu p_{i,\mu}}$ are assumed to be small compared to the transverse momenta $p_{t,i}$. Each protojet is characterised by $(\eta_i, \phi_i, E_{t,i})$, where $E_{t,i}$ is defined as $E_i \sin \theta_i$. This is actually a slight change from the original formulation [ES93], which used $E_{t,i} = |p_{t,i}|$.

Given a list of protojets the inclusive k_t algorithm now recursively joins pairs of protojets to form new protojets. The algorithm also determines, when manipulations of a protojet should cease, and it should be moved to the list of ‘‘jets’’.

Given a list of protojets, the jet algorithm proceeds as follows:

1. For each protojet, a ‘‘size’’ d_i is defined:

$$d_i = E_{t,i}^2 \quad (6.3)$$

Correspondingly for all pairs of protojets i, j , a ‘‘distance’’ is defined according to the metric:

$$d_{ij} = \frac{\min(E_{t,i}^2, E_{t,j}^2) [(\eta_i - \eta_j)^2 + (\phi_i - \phi_j)^2]}{R^2} \quad (6.4)$$

Note the parameter R , which should be supplied by the user. It is analogous to the cone size in the cone algorithms. R has been set to 1 in the present analysis.

2. Define d_{\min} to be the smallest of all the d_i and d_{ij} .
3. If d_{\min} is a d_{ij} , protojets i and j are merged into a new protojet k according to:

$$E_{t,k} = E_{t,i} + E_{t,j} \quad (6.5)$$

$$\eta_k = \frac{E_{t,i}\eta_i + E_{t,j}\eta_j}{E_{t,k}} \quad (6.6)$$

$$\phi_k = \frac{E_{t,i}\phi_i + E_{t,j}\phi_j}{E_{t,k}} \quad (6.7)$$

4. If d_{\min} is a d_i , protojet i is considered not mergeable. It is consequently moved from the list of protojets to the list of jets.
5. Re-iterate

The procedure continues until there are no more protojets. The result is that all particles in the hadronic final state are grouped into a list of jets. The list is ordered by transverse momentum as a consequence of step 3 and 4 above. Only the jets with high E_t will generally be of physical interest, though.

The fact that all particles are included makes the algorithm well suited for inclusive measurements, such as the “one jet or more”-cross section. If one wishes to make exclusive measurements, $p_t = E_t$ of the jets is a good cut-off parameter.

It is a matter of key importance that a jet algorithm be infrared safe. This is simply the statement that the addition of a soft parton should not change the results.

The infrared divergences at parton level arise from situations in which a parton emits a soft gluon, with $q^\mu \rightarrow 0$, or in which a parton splits into two collinear partons.

Infrared safety is quickly realised for this case, as two collinear partons would immediately be recombined by the algorithm. Also, there would be no change in the jet cross sections for very soft gluon emissions, as neither the angle nor the E_t of the jets would be changed by the soft gluon.

Part II

The Experimental Facility

No amount of experimentation can ever prove me right; a single experiment can prove me wrong.

[Albert Einstein, 1879 - 1955]

Chapter 7

The HERA Collider

The HERA collider is an accelerator complex designed to collide electrons or positrons with protons. The main components of HERA are the two storage rings, in which the protons and electrons are accelerated to their final energies of respectively 820 GeV and 27.5 GeV.¹

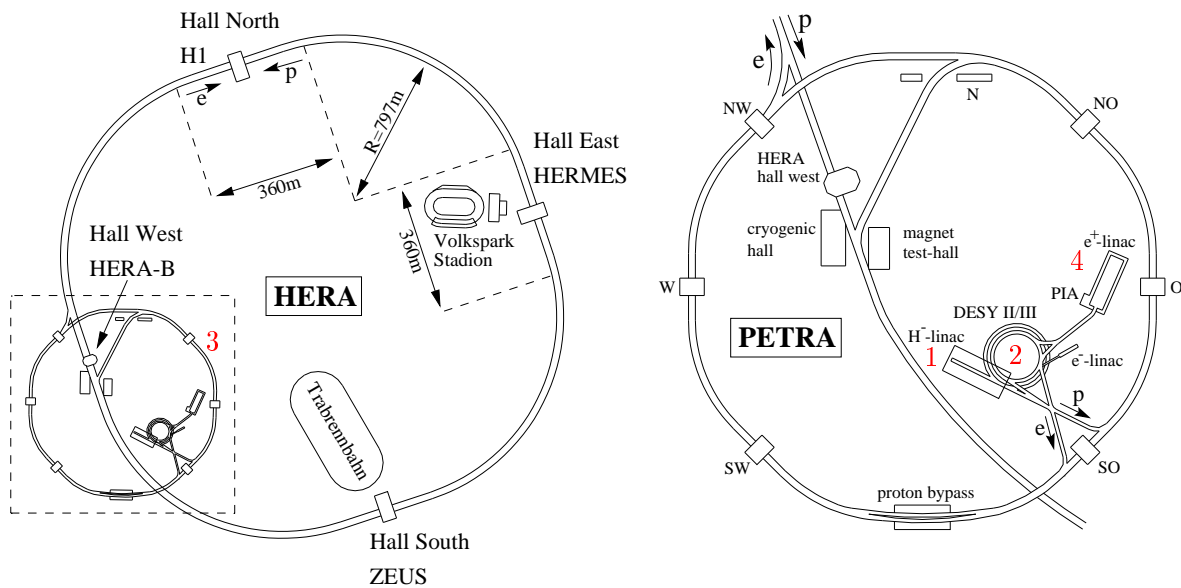


Figure 7.1: An overview of the HERA facilities

7.1 The Colliding Beams

To reach the point where the two beams are ready to be brought to collision, the particles pass through several stages of pre-acceleration before entering the main HERA ring.

First, the proton beam is prepared. A sample of protons is made by stripping hydrogen atoms of their electrons. The linear accelerator LINACIII (1) accelerates the protons to 50 MeV,

¹In 1998, the proton energy was upgraded to 920 GeV

whereupon the DESYIII accelerator (2) increases the energy to 7.5 GeV. The proton bunches are then transferred to PETRAII (3) for acceleration to approximately 40 GeV. When this energy is reached, the protons are injected into HERA.

When all available proton bunches in HERA have been filled and accelerated to their final energy, there are around 180 bunches with a total current of approximately 80 mA.

After injection and acceleration of the protons, the electron beam is prepared. For stability reasons typically a positron beam is used.

The electrons are accelerated to 450 MeV in the linear accelerator LINACII (4). They are then transferred to the DESYII ring (2), where they reach an energy of 7 GeV. At this energy, they are injected into PETRAII. At an energy of 13 GeV, the electron beam is transferred to HERA, for final acceleration to 27.5 GeV.

The filling of the bunches in HERA takes place in several stages. In the luminosity mode, the electrons generate a current of typically 20-30 mA.

In the past years the lepton beam has typically consisted of positrons. This is due to the fact that a positron beam is easier to keep stable over long periods of time. Positively charged gas ions remaining in the beam pipe tend to get attracted to an electron beam causing the beam quality to deteriorate faster, as the ions attenuate the beam.

7.2 Experiments at HERA

The experimental program of HERA includes four experiments. These are ZEUS, HERMES, HERA-B and H1.

HERMES [Mil97] is a fixed target experiment focused on studying the spin structure of the proton. For this purpose, a polarised gas target is used as a target for the polarised e^+ -beam to study the polarisation dependence of DIS.

HERA-B [H^+] is another fixed target experiment. It was originally intended to provide fast results on CP-violation parameters in b-physics through Υ -production in pN-collisions, but recently the focus has shifted to more general areas of QCD. The collaboration itself has now decided to stop the experiment, but the possibility still remains that other collaborations may be interested in using the detector.

ZEUS [ZE] is a general purpose ep-collision detector similar to H1. It is designed to investigate parton dynamics in QCD in depth. Main topics are the partonic structure of the proton and the photon, vector meson production and hadronic final states.

The H1 detector is described in detail in the next chapter.

Chapter 8

The H1 Experiment

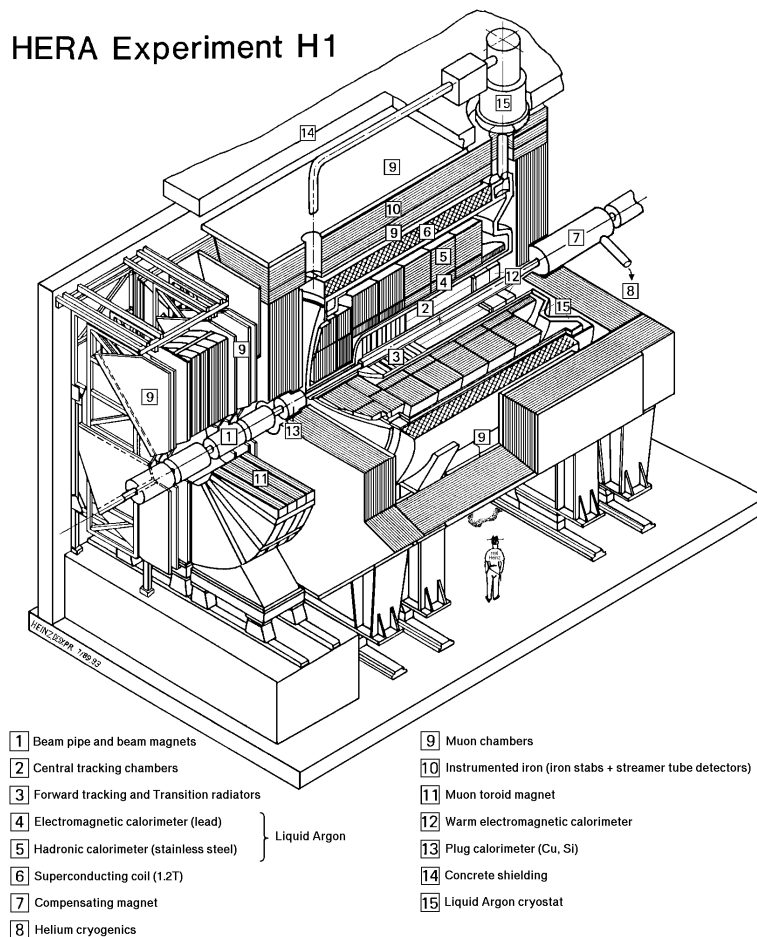


Figure 8.1: An overview of the H1-detector

The H1 detector is a complex apparatus designed to measure properties of particles originating from high energy ep -collisions at HERA. The detector consists of a multitude of sub-detectors arranged around the nominal interaction point with a solid angle coverage of close to 4π . The only openings in the detector are in the forward and backward regions to allow for the beams

to enter and exit the detector.

I will here describe the 1997 configuration of the H1 detector, with a few concluding remarks on later upgrades. Where no other references are given, the reader is referred to the technical design report: [H197a], [H197b].

The interaction point is surrounded by a tracking system, which is again divided into a central and a forward tracker. The trackers are used for high-precision measurements of charged particle trajectories and particle identification. The energies of the particles in the event are measured by calorimeters surrounding the trackers. Along the beam axis, a Time-of-Flight system (ToF) is installed. This consists of three stations of scintillators, and it is used for particle identification as well as for trigger veto on the primary vertex of the event. Around the trackers and the calorimeters, there is a superconducting solenoid magnet which produces a close-to uniform magnetic field of 1.15 T. To detect muons and hadronic energy which penetrate all of the inner detector elements as well as the solenoid magnet, the return yoke of the solenoid is instrumented with streamer tubes and muon detectors. Forward muons are measured with the Forward Muon Spectrometer (FMS).

In this analysis, the following detectors are of key importance:

- The backward “Spaghetti” Calorimeter (SpaCal), together with the Backward Drift Chamber (BDC), performs high precision measurements of the scattered electron, providing key information on the kinematics of the event.
- The Liquid Argon (LAr) calorimeter measures energy deposits in the main solid angle of the detector.

The standard H1 coordinate system is chosen as a right-hand system with the z -axis along the proton beam direction and the x -axis pointing towards the centre of the HERA ring. The origin of the system is placed in the nominal interaction point.

8.1 General Design Considerations

In HERA ep -collisions, the Centre-of-Mass system is highly boosted in the forward (proton) direction. The boost corresponds in average to $\gamma \approx 2.9$. A consequence of this energy asymmetry is the asymmetric design of H1 shown in figure 8.2. The proton direction is to the left. The instrumentation in this direction is more segmented and massive than in the backward direction.

As is described in section 3.1.1, a good identification and reconstruction of the scattered lepton is crucial for an accurate reconstruction of the kinematics in an event. It was therefore a major design goal to achieve good electron/pion separation as well as an accurate measurement of the electron energy.

8.2 Tracking

The H1 tracking system depicted in figure 8.3 serves to provide efficient track reconstruction and from the track bending radius in the magnetic field to measure the momenta of the

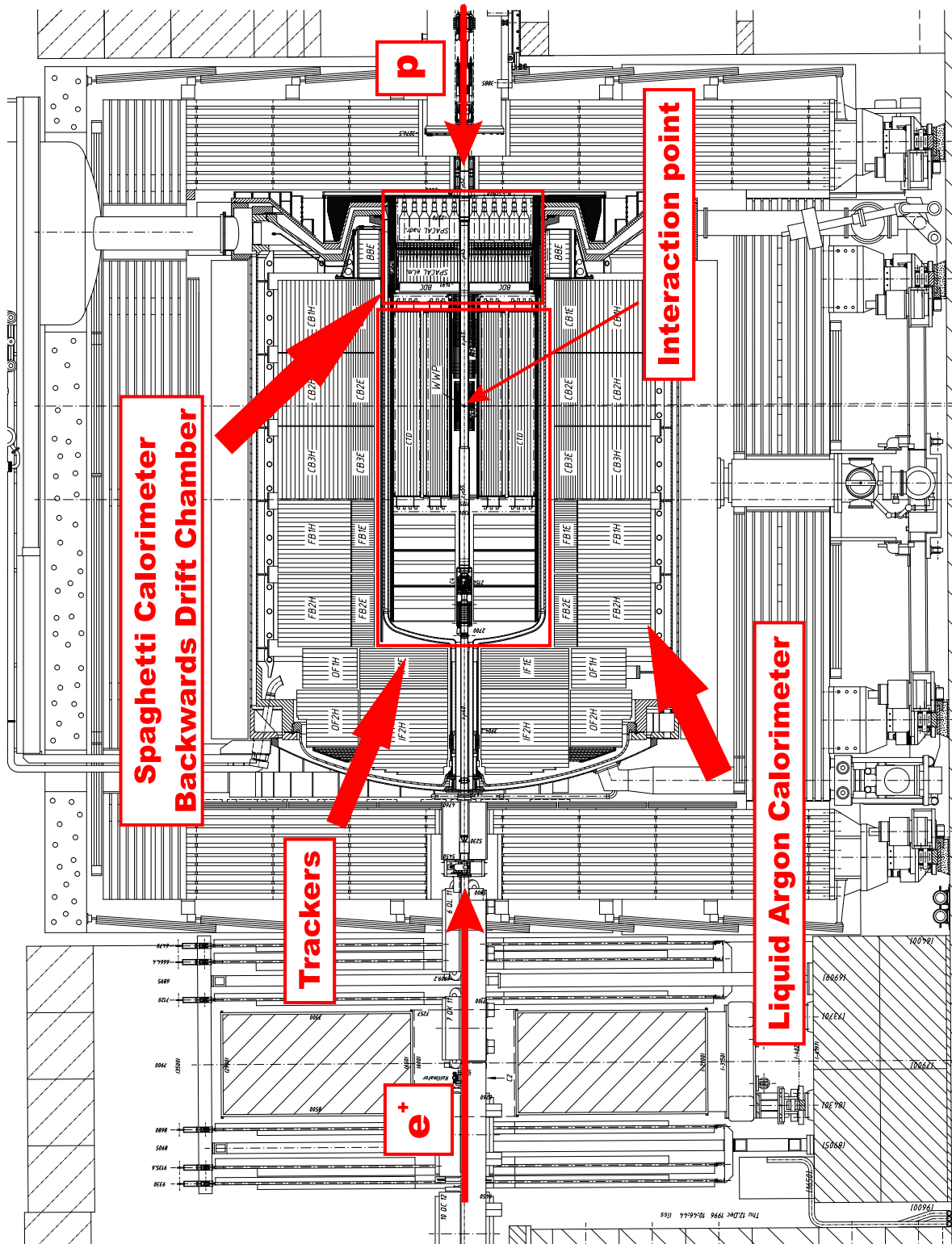


Figure 8.2: Longitudinal cut through the H1 detector parallel to the beam pipe

charged particles in an event. As the inner parts of the tracker are silicon-based and thus very fast, they are also used to make trigger decisions based on track abundance and directions. For analyses relying on very accurate vertex reconstruction (such as heavy flavour decays), the silicon trackers also provide a possibility to identify primary and secondary vertices to a precision of $37 \mu\text{m}$ [P⁺00].

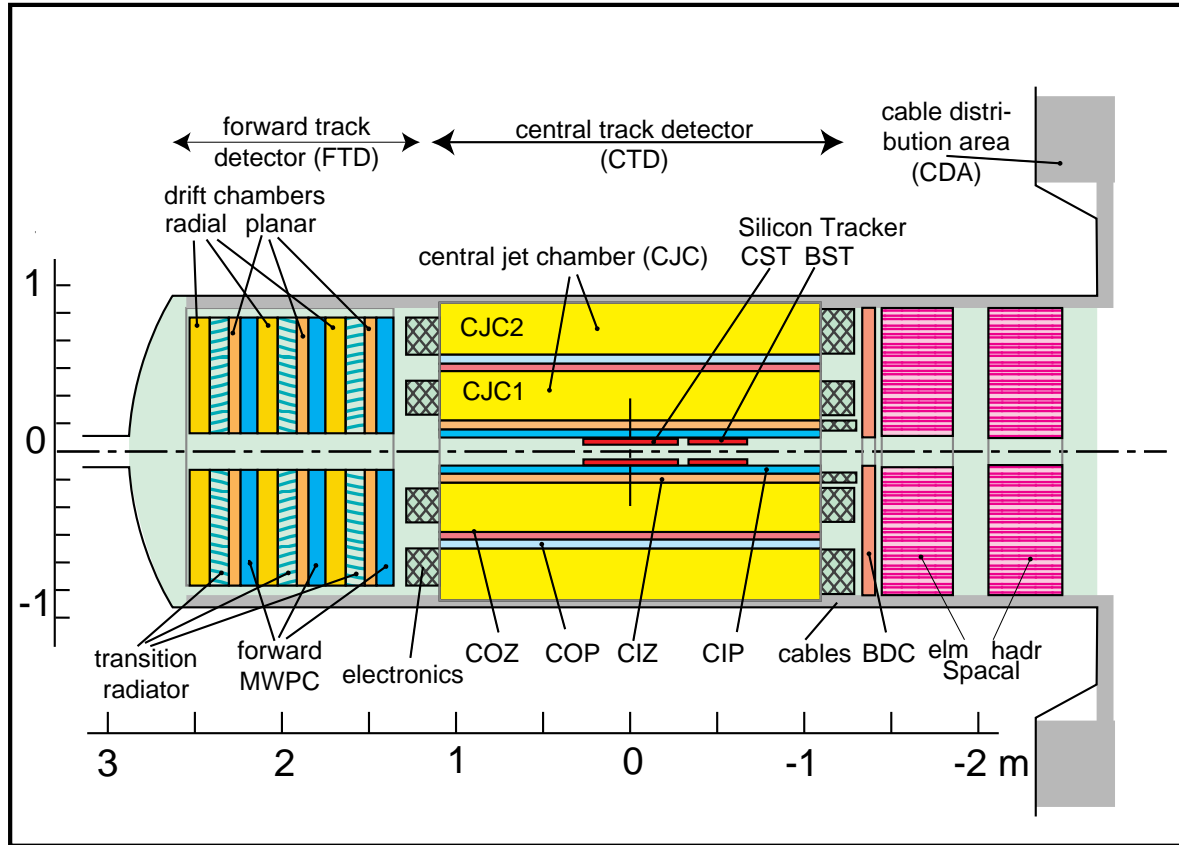


Figure 8.3: An overview of the H1 tracking system

8.2.1 The Central and Backward Silicon Trackers (CST & BST)

When charged particles pass through a semiconducting material, they produce electron-hole pairs. These can be collected using an n-p junction subjected to an electric field to provide accurate and very fast track information ([Leo] ch. 10).

The Central Silicon Tracker [P⁺00] of the H1 experiment consists of two concentric cylindrical layers of silicon sensors with two coordinate readout.

The silicon sensors are strip detectors with $r\phi$ -strips on the p-side, and z -strips on the n-side - a structure sometimes referred to as a “half-ladder”. The CST has a point resolution of $12 \mu\text{m}$ in the $r\phi$ -direction and $22 \mu\text{m}$ in the z -direction. This enables the CST to successfully identify secondary decay vertices from hadrons containing b -quarks.

The Backward Silicon Tracker [HL00] consisted in 1997 of 4 discs segmented in 16 sectors each. The layout of the BST itself and of a sector is shown in figure 8.5.

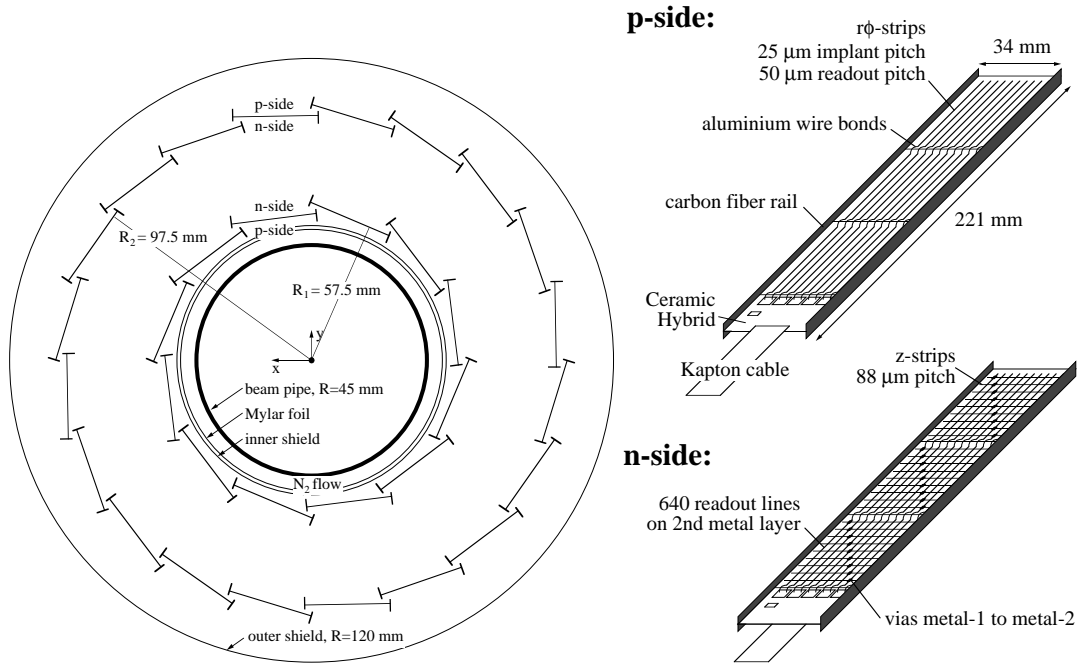


Figure 8.4: The layout of the Central Silicon Tracker (CST) with a sketch of a half-ladder.

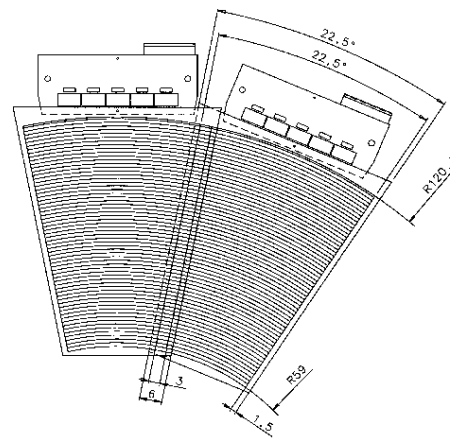
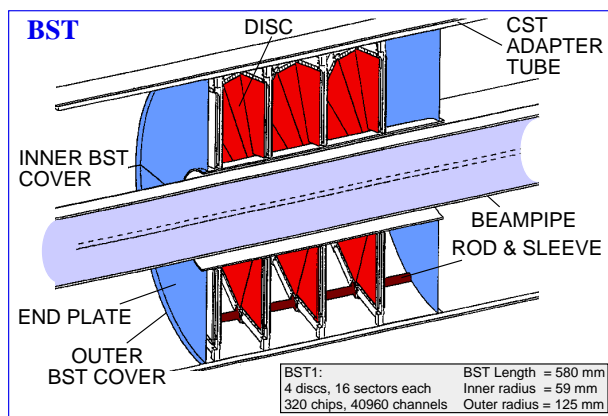


Figure 8.5: The BST

The BST has a radial resolution of $16 \mu\text{m}$ and an azimuthal resolution of $\frac{22^\circ}{\sqrt{12}}$. The bad ϕ -resolution stems from the fact that the primary task for the BST is to measure r and consequently θ .

8.2.2 The Central Jet Chambers (CJC 1 + 2)

The Central Jet Chambers CJC1 and CJC2 [B⁺89] are the largest tracking sub-detectors in the H1-experiment, and the ones primary responsible for reconstructing track information. They consist of two concentric drift chambers with an active length of 2200 mm. Sense wires are strung parallel to the beam axis, and the readout of each end of a wire provides a z -resolution of approximately 22 mm (1% of the wire length) by charge division. The combination of the wires provide an $r\phi$ -resolution of $170 \mu\text{m}$.

Each chamber is divided into drift cells. CJC1 consists of 30 cells with 24 anode wires each, whereas CJC2, due to its larger volume, is made up of 60 cells each with 32 wires.

The individual drift cell is tilted about 30° with respect to the radial direction as shown in figure 8.6.

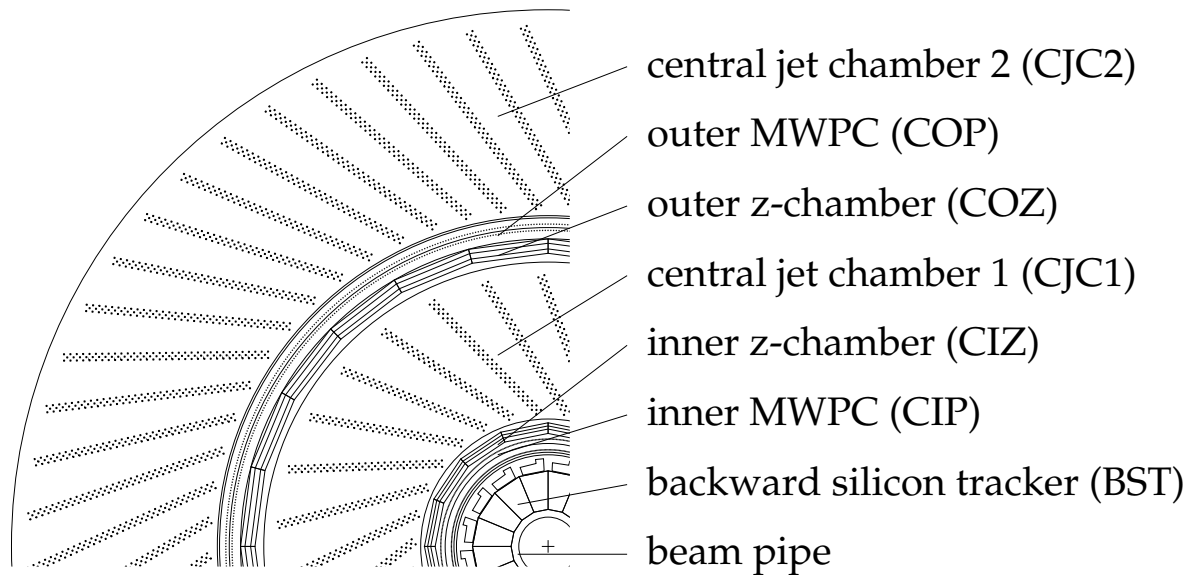


Figure 8.6: An end-on view of the tracking system. Note the angle of the CJC-cells with respect to the radial direction.

This orientation of the drift cells has several advantages. It provides the optimum track resolution in the $r - \phi$ -plane of $170 \mu\text{m}$. In addition, it improves the track reconstruction, as it is now possible to determine on which side of the wire, the particle passed through the cell. “Wrong mirror”-hit candidates do not match to form tracks, and the segments that are formed do not point to the vertex.

8.2.3 Z-Chambers (CIZ,COZ)

Immediately inside CJC1 and CJC2, respectively, the inner and the outer z -chambers (CIZ / COZ) are placed. This placement can be seen in figure 8.6, and in figure 8.3. They are thin drift chambers with sense wires perpendicular to and drift direction parallel with the beam axis. They complement the measurement of the charged track momenta by a z -coordinate measurement with a precision of typically $300 \mu\text{m}$.

8.2.4 The Backward Drift Chamber (BDC)

The Backward Drift Chamber [Sch96] is designed as a supplement to the Spaghetti Calorimeter (see section 8.3.2), to improve the measurement and identification of the scattered electron. It is installed in front of the SpaCal covering an angular range of $153^\circ < \theta < 177.5^\circ$.

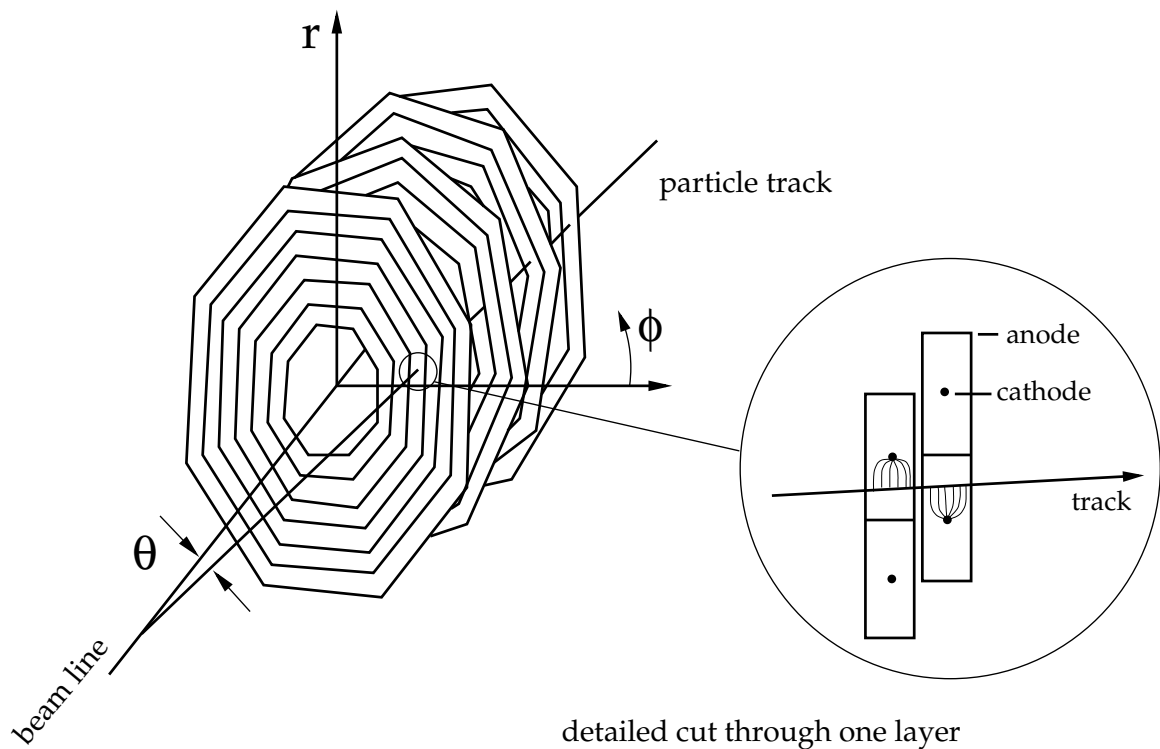


Figure 8.7: *The Backward Drift Chamber*

The chamber consists of four double layers divided into eight ϕ -sectors. Each of these sectors comprise 32 drift cells with sense wires.

Figure 8.7 shows a schematic view of the BDC wire orientation. As the figure shows, the wires are strung in the ϕ -direction. This is to optimise θ -resolution for reconstruction of kinematic variables (see section 3.1.1). The individual double layers are revolved 11.5° to allow for a coarse ϕ -measurement. The resolution in θ of the chamber is 0.57 mrad [K⁺98].

8.2.5 The Forward Tracking Detector (FTD)

The Forward Tracking Detector is a set of drift chambers designed to detect forward tracks in the angular region $5^\circ < \theta < 25^\circ$. The FTD comprises three identical super-modules. Each of these super-modules consists of three planar chambers, a multi-wire proportional chamber (MWPC, [Leo] ch. 6), a transition radiator and a radial cell.

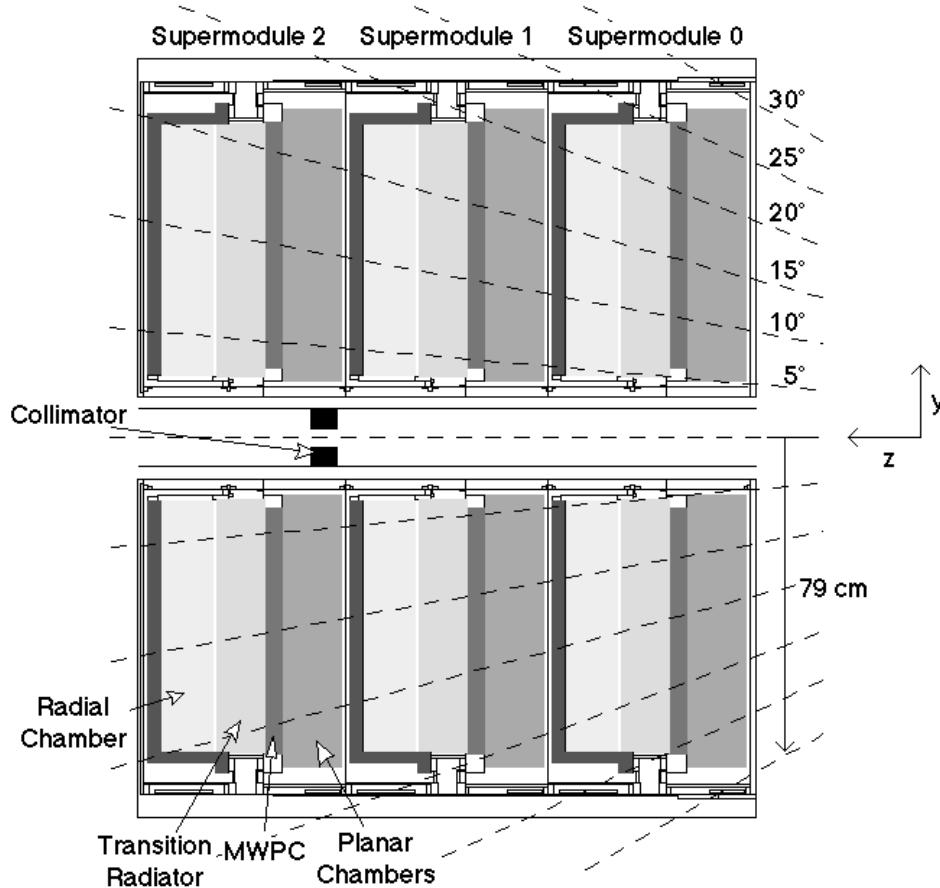


Figure 8.8: *The Forward Tracking Detector*

The planar chambers are oriented with $\phi = 0^\circ$, -60° or 60° , and are comprised of 32 rectangular cells, each with four wires. The radial chambers have 48 wedge-shaped cells with wires mounted radially from the beam axis.

Transition radiation is electromagnetic radiation in the X-ray region, which is emitted when an ultra-relativistic particle crosses a boundary between two media of different dielectric constant. The transition radiators are used for electron/pion-separation, as transition radiation rises strongly with the γ factor of the particle in question. Electrons therefore produce far more transition radiation than pions with similar energies. For more information on transition radiation, see [Ege].

The track momentum resolution is $\frac{\sigma_p}{p^2} < 0.003 \text{ GeV}^{-1}$, whereas the track angular resolution is $\sigma_{\theta,\phi} < 1 \text{ mrad}$.

8.3 Calorimetry

H1 is equipped with a number of calorimeters using a variety of technologies. These units are:

- The Liquid Argon Calorimeter (LAr)
- The Spaghetti Calorimeter (SpaCal)
- The forward calorimeter (Plug)
- The Tail Catcher (TC)

The individual calorimeters will be treated in detail below. For the present analysis, the LAr-calorimeter along with the SpaCal have been the most important calorimeters. The Plug calorimeter is situated in the very forward region of $3.5 < \eta < 5$, and the Tail Catcher is installed in the iron yoke of the magnet to measure leakage from the other calorimeters.

8.3.1 The Liquid Argon Calorimeter (LAr)

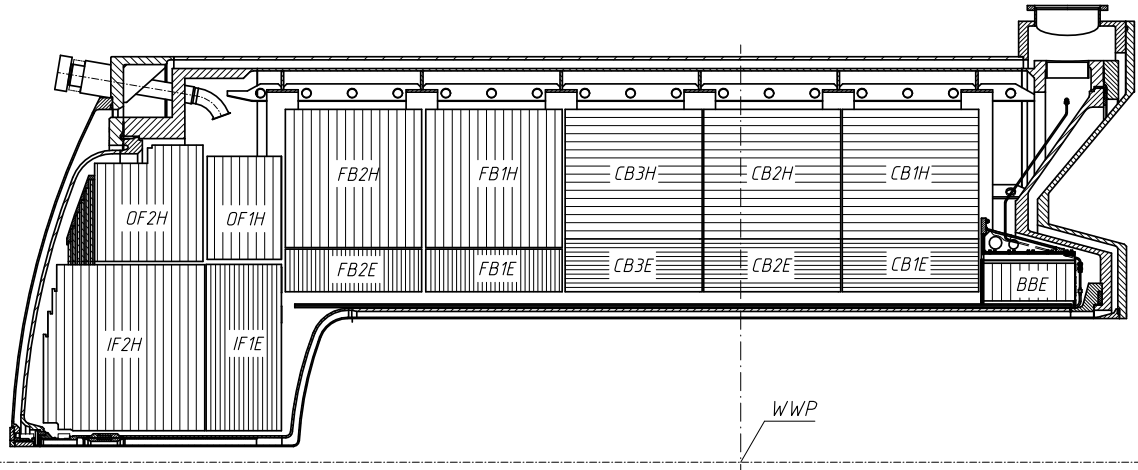


Figure 8.9: *The Liquid Argon calorimeter*

The Liquid Argon calorimeter [H1Cal93] is the largest single calorimeter of H1. It covers the angular range between 4° and 153° .

A liquid Argon calorimeter is essentially a stack of metal plates immersed in liquid Argon ([Leo] ch. 6). A voltage is applied between the plates. Incoming particles shower in the metal, whereupon the shower ionises the Argon, and the electrodes pick up the charge. Since the entire shower is collected, the energy of the shower is proportional to the ionisation collected.

The liquid Argon calorimeter of H1 is placed within the solenoid magnet to minimise the amount of dead material in front of it. It comprises an electromagnetic part and a hadronic part. The innermost cells which are seen in figure 8.9, comprise the electromagnetic part of the LAr. The outer cells make up the hadronic part. Showers in the electromagnetic

part result from the use of lead plates, whereas steel is used in the hadronic part. In the z -direction, the LAr is made up of 8 wheels, each consisting of 6-8 sections in ϕ .

The resolution of the LAr is comprised of several quantities:

- The electromagnetic energy resolution is $\frac{11\%}{\sqrt{E(\text{GeV})}} \oplus 2\%$
- The hadronic energy resolution is $\frac{50\%}{\sqrt{E(\text{GeV})}} \oplus 2\%$

The absolute energy scale is reconstructed up to an uncertainty of 4% and constitutes one of the main contributions to the systematic error in this analysis.

8.3.2 The Spaghetti Calorimeter (SpaCal)

For low values of momentum transfer, $Q^2 < 100 \text{ GeV}^2$, the deflection angle of the lepton is quite small. It traverses the backwards detectors and hits the Spaghetti Calorimeter. [H1SG96].

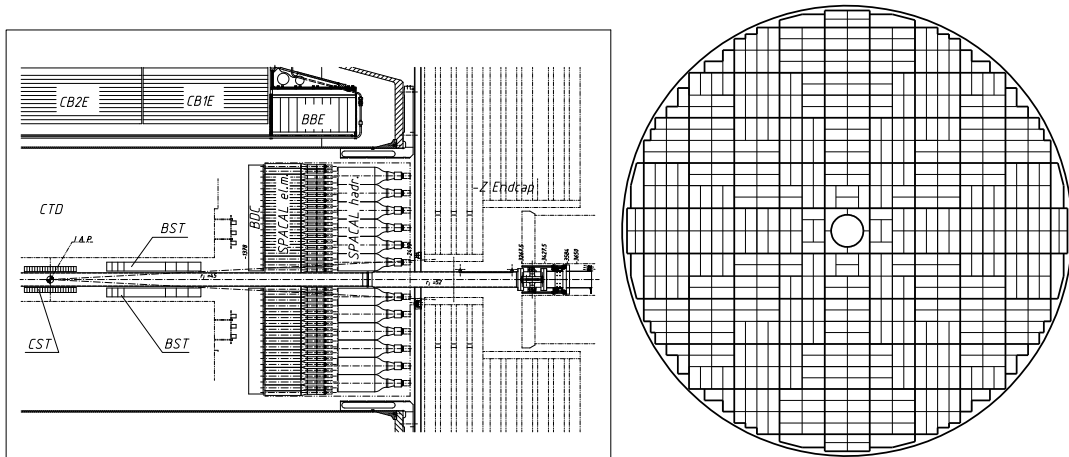


Figure 8.10: *The Layout and location of the SpaCal. The side view shows the placement of the SpaCal in the H1 detector. The electromagnetic and hadronic sections are visible. The end-on view only shows the electromagnetic part of the SpaCal.*

The SpaCal covers the angular region of $153^\circ < \theta < 177.5^\circ$, and is located behind the BDC. It consists of a hadronic and an electromagnetic section, as shown in figure 8.10.

Both the electromagnetic and the hadronic sections of the SpaCal consist of scintillating fibres embedded in a lead matrix. The diameters of the fibres are 0.5 mm and 1.0 mm, respectively. Incident particles shower in the lead, and the shower is detected by the scintillating fibres. The scintillations are now picked up by photo-multipliers and converted into electrical pulses.

The layout of the electromagnetic section of the SpaCal is also shown in figure 8.10. It is divided into 1192 cells, which allows for a good electron/hadron separation by measurement of transverse shower profiles. The depth of the Elm-SpaCal is 25 cm, which is sufficient for a 30 GeV electron to deposit all of its energy.

The angular resolution of the SpaCal is 2 mrad, whereas the energy resolution is $\frac{7\%}{\sqrt{E(\text{GeV})}}$, plus an uncertainty of 1% in the absolute energy scale.

As for the hadronic section of the SpaCal, it is somewhat coarser, consisting of only 136 cells of a depth of 25 cm. It is used mainly to distinguish between hadronic and e/γ showers based on penetration depth.

8.4 The Luminosity System

The luminosity measurement of H1 is based on the process $ep \rightarrow ep\gamma$. These events are referred to as *bremsstrahlung* events. The cross section for this type of event is calculable to a very high degree of precision within QED, and the signature is very distinct.

To measure these events, an Electron Tagger (ET) and a Photon Detector (PD) are installed very close to the beam pipe away from the detector. Their positions are $z_{ET} = -33.4$ m and $z_{PD} = -102.9$ m. In the on-line luminosity measurement, coincidental detection of a proton and a photon is used for simplicity, whereas the off-line method relies only on the detected photon. The uncertainty on the luminosity measurement is 1%.

8.5 The Time-of-Flight System (ToF)

A lot of background events are present under the running conditions of HERA. A central source of these events is collisions of the beam particles with the beam pipe or with residual gas atoms. To reject these events, a Time-of-Flight system is installed. The system consists essentially of a number of scintillator devices mounted perpendicularly to the beam pipe. Combining information from the SpaCal with the output of the scintillators, it is possible to determine whether the detected particles originate from a “real” event.

This decision is based on the definition of time windows given by the HERA clock. The HERA clock tells when bunch crossings occur. It is then a matter of simple geometry in combination with exact timing to determine whether an event be rejected on the basis of the ToF information.

8.6 The Trigger System

The bunch crossing frequency at HERA is approximately 10 MHz, and the number of read-out channels of the H1 detector is around 270,000. Not all of these channels are equally fast, and not all of the events taking place in the detector are equally important. In fact the typical background rate at the design luminosity of $\mathcal{L} = 1.5 \times 10^{31} \text{ cm}^{-2}\text{s}^{-1}$ is 50 kHz from beam-gas events alone, while the DIS rate is approximately 2.2 Hz, and W -events in contrast occur a couple of times a week [H197a]. These conditions dictate the need for a trigger system to determine when to read out the detector and which events to keep.

The trigger system is composed of four levels, denoted L1-4. The Level 1 (L1) trigger makes a selection for each bunch crossing. This selection is made based on track origin information and ToF information to cut down the beam-gas rate. The L1 trigger combines trigger elements

in up to 128 sub-triggers. The second- and third-level triggers were bypassed in the 1997 configuration. At the fourth level trigger (L4), all information is evaluated, and a limited reconstruction of the event takes place. At both trigger levels *pre-scaling* may occur. Pre-scaling by a factor n means that only every n th event is kept for a given sub-trigger condition, reducing the trigger rate and the need for storage by a factor n . A corresponding weight of n is then applied to the events kept.

After approval from the L4 trigger, the event is written to disk and kept. The output rate of the L4 trigger is typically around 10 Hz. In other words, only one event is kept for one million bunch crossings. A lot of these events are background events, though, as the trigger system is designed to make sure that no interesting events are rejected.

Part III

Forward Jet Analysis

In physics, you don't have to go around making trouble for yourself - nature does it for you.

[Frank Wilczek 1951 -]

Chapter 9

Event Selection and Corrections

Attempts to identify a BFKL-like behaviour in inclusive DIS have so far proved not to be successful. This is largely attributed to the fact that the phase space for DGLAP parton evolution is very large, and BFKL-effects tend to be “washed out”.

To counter this problem, it has been suggested ([Mue91b], [Mue91a], [BdRL92], [Tan92]) to look at *forward jets* in order to specifically target a phase space region in which DGLAP is suppressed. This improves the chance to disentangle possible effects from BFKL dynamics from the dominating DGLAP effects.

In the following chapters, a study of forward jets using 1997 data from the H1 experiment is presented. The study is based on an integrated luminosity of 13.72 pb^{-1} of runs passing the trigger selections. As the detector configuration and the triggers changed substantially after 1997, data from later years cannot be merged with the 1997 data without redoing the detector calibration and the trigger studies.

A cross section measurement is performed, and event variables are studied. The results are corrected to hadron level and compared to theoretical predictions by the Monte Carlo event generators. For comparison with DGLAP the Monte Carlo generator RAPGAP is used. As no BFKL Monte Carlo exists to describe DIS, the data have been compared to the CCFM generator CASCADE.

9.1 Forward Jets and Resummation Schemes

As described in section 4.1, a key signature of DGLAP is a strong ordering in the transverse momentum of the emitted partons in the cascade. To suppress this k_t -ordering and yet leaving room in the kinematics for parton evolution in x , events have been selected in which a forward jet is reconstructed carrying a significant fraction of the proton energy and with a transverse momentum of the same order of magnitude as Q^2 of the event.

This situation is depicted in figure 9.1. As is indicated by the diagram, a high energy parton emission having $k_t \sim Q^2$ will indeed suppress k_t -evolution. There is no “room” left for strong k_t -ordering.

Therefore, to directly suppress strong k_t -ordering, events are selected containing a jet in the

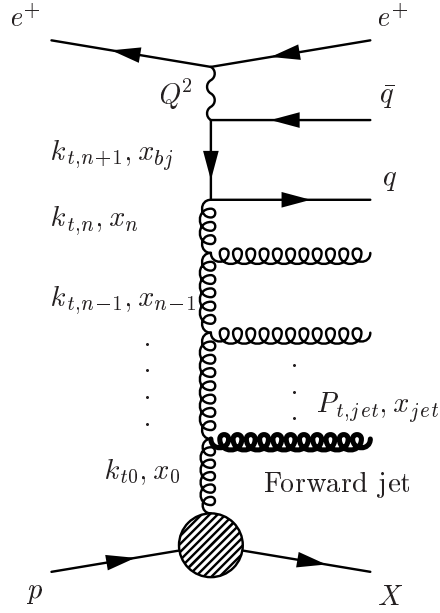


Figure 9.1: A generic forward jet diagram.

forward direction, the transverse momentum of which is required to be of the same order of magnitude as Q^2 through the requirement:

$$0.5 \leq \frac{P_{t,jet}^2}{Q^2} \leq 2 \quad (9.1)$$

To enhance BFKL-like dynamics through evolution in x , the energy of the jet is required to fulfil

$$x_{jet} \equiv \frac{E_{jet}}{E_p} \gg x_{bj}, \quad (9.2)$$

leaving room in the parton ladder for evolution in x .

9.2 The Need for an Event Selection

When performing a physics analysis, it is important to define the event selection in such a way as to clearly define the physics of interest, so that conclusions may be drawn. Different cuts are applied and activity is required (or disallowed) in different sub-detectors. This helps to ensure accurate reconstruction of the events while minimising corrections and suppressing background. The event selection for this analysis consists basically of three parts:

1. Selecting “clean” runs and events without disturbing noise.
2. Defining a kinematic region of the event, optimising the performance of the individual sub-detectors and possibly reducing the background.
3. Imposing the forward jet requirement to target the desired dynamics.

In the following sections, I will explain the event selection from run and trigger selection to the complete forward jet selection. The exact cuts chosen are very close to [Kar02] and to the ongoing H1 forward jet analysis, [H103b] for compatibility.

9.3 Run Selection and Triggers

The present analysis is based upon data taken during 1997. During this period of data taking an integrated luminosity of 21.57 pb^{-1} was collected. In the selection of runs, the basic requirement is that the high-voltage system of the H1-detector is turned on, and that the following detectors are operational (see chapter 8): The Liquid Argon calorimeter, the Spaghetti Calorimeter, the Backward Drift Chamber, the Central Jet Chambers, the Inner z -chamber, the Time-of-Flight scintillators and the luminosity system.

The number of runs fulfilling these requirements provide an integrated luminosity of 13.72 pb^{-1} .

As there is a bunch crossing every 96 ns in HERA, a lot of events need to be rejected already at the data acquisition stage. Other events represent physics classes which are irrelevant to this analysis such as charged current interactions and high Q^2 events.

The L1 trigger requirement made in this analysis is based on the S_0 trigger, which is defined by:

$$S_0 = (IET > 2) \wedge (TOF) \quad (9.3)$$

The two trigger elements are the SpaCal Inclusive Electron Trigger, IET ([H196],[Spi96]) and the backward Time of Flight trigger, TOF ([H197a]).

The IET -requirement of 2 corresponds to a positron energy threshold of 5.7 GeV. The TOF element is a composite trigger element ensuring that measured particles originate from near the nominal interaction point.

At the higher level triggers, event classes are defined based on different cuts in the event topology and activity in the different sub detectors [H1L]. It is in this analysis a requirement that the events be in the event classes *Jet* and *DIS*.

9.4 Detector Cuts

To correctly identify a DIS event, it is important to ensure a good quality of the event reconstruction. This is obtained by imposing cuts on the reconstructed positron as well as on the primary event vertex and a global event variable. These cuts will be treated in detail below.

9.4.1 Positron Cuts

A primary objective is to have an accurate reconstruction of kinematic quantities. The reconstruction rests upon a reliable and precise reconstruction of the scattered positron done by the SpaCal and the BDC.

To ensure that the positron is fully within the acceptance of the SpaCal, the following angular cut is imposed:

$$160^\circ \leq \theta_e \leq 172.5^\circ \quad (9.4)$$

A large contribution to the background is the so-called photo-production events, in which Q^2 is very small. In these events, the scattering angle of the positron is so small that it goes down the beam pipe. The measurement is therefore sensitive to hadrons being misidentified as the positron.

To counter this, a lower cut is imposed on the positron energy:

$$E_e \geq 11 \text{ GeV} \quad (9.5)$$

The cut has several justifications. It ensures a high efficiency of the S_0 -trigger. At the same time, it suppresses “fake” positron candidates stemming from hadrons or showering in the dead material in front of the SpaCal. It thus helps to suppress photo-production events.

As described in section 8.3.2, the SpaCal consists of a number of cells. SpaCal clusters are defined by summing up energy deposits in the individual cells. When selecting the positron among the possible candidate clusters, the fact is used that hadronic showers in general are broader than e/γ -showers. The centre-of-gravity of a SpaCal cluster r_c is defined:

$$r_c = \frac{\sum_{i=1}^n \sqrt{E_i} r_i}{\sum_{i=1}^n \sqrt{E_i}} \quad (9.6)$$

where r_i and E_i correspond to the centre and the energy of the i th SpaCal cell, respectively. The energy weighted cluster radius is then given by

$$R_c = \frac{1}{E_c} \sum_{i=1}^n E_i \times |r_i - r_c|, \quad (9.7)$$

where E_c refers to the combined cluster energy. To reduce background from hadronic showers, the cut on R_c is

$$R_c \leq 3.5 \text{ cm}. \quad (9.8)$$

However, the detector simulation of the H1 detector gives a different positron cluster radius than what is found in the data. To correct for this, a factor of 1.065 has been applied to the positron cluster radius in the Monte Carlo. Figure 9.2 shows the effect of this correction.

More background from hadronic interactions is removed by requiring very little activity in the hadronic part of the SpaCal which is placed behind the electron part (see section 8.3.2). It is required that $E_{Had} \leq 0.5 \text{ GeV}$, where E_{Had} is the sum of all energy deposits in the hadronic part of the SpaCal within a circle of radius 15 cm with respect to the position of the positron.

If the positron is found very close to the beam pipe, there is a significant risk that part of the energy is not contained in the SpaCal and “leaks” into the beam pipe. To reject events where this may be a problem, the SpaCal is equipped with four veto cells close to the beam pipe. If the combined energy in these cells E_{Veto} exceeds 1 GeV, the event is rejected.

Showers from photons are very much like positron showers. To discern between the two, information from the BDC is used to match the positron cluster with a track, utilising that

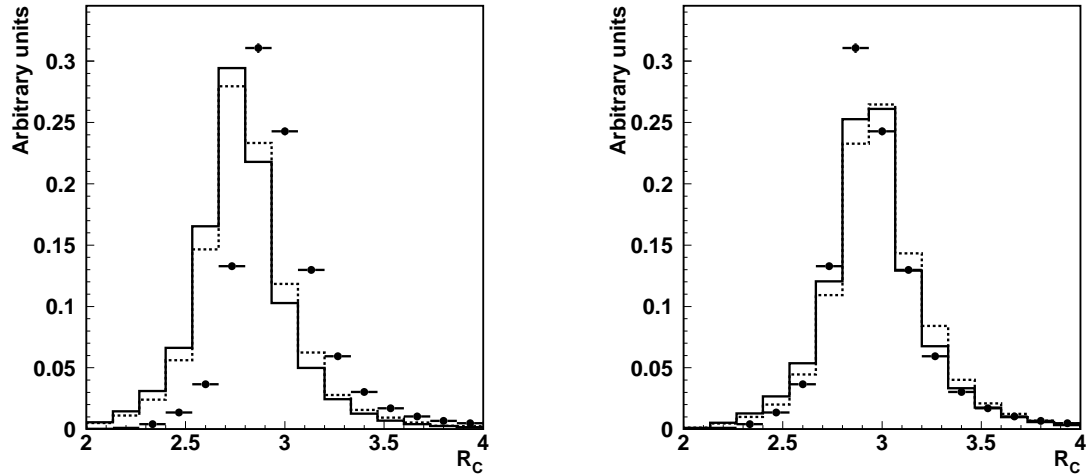


Figure 9.2: The R_C -distribution of data (points) compared to the Monte Carlo generators *ARIADNE* (solid line) and *RAPGAP* (dotted line). The left plot shows the uncorrected Monte Carlo distributions, and the right one shows the distributions after correction. The histograms have been normalised to one.

the positron is a charged particle. To this end, a cut on the distance between a reconstructed BDC track and the SpaCal cluster is imposed to be

$$\Delta R_{BDC} \leq 3 \text{ cm.} \quad (9.9)$$

During the 1997 data taking, certain regions of the SpaCal showed insensitivities, and they have been excluded. In coordinates (x_s, y_s) of the SpaCal, the excluded regions are:

$-16.2 < x_s < 8.1$	\wedge	$-8.1 < y_s < 16.2$
$-25.0 < x_s < -20.5$	\wedge	$37.5 < y_s < -33.0$
$-16.25 < x_s < 12.5$	\wedge	$-21.0 < y_s < -16.0$
$-31.5 < x_s < -25.5$	\wedge	$33.1 < y_s < 39.1$
$-48.0 < x_s < 46.1$	\wedge	$-28.0 < y_s < -25.0$

Table 9.1: Excluded SpaCal regions.

Events with a reconstructed positron inside the less sensitive regions are rejected.

9.4.2 Vertex Cut

A large contribution to the background is beam-gas interactions, in which a beam particle interacts with the remnant gas in the beam pipe. It may also occur that particles in the beam halo hit a bending magnet or a collimator, producing an “event” in which the primary vertex is offset from $z = 0$.

In figure 9.3 is shown a beam-gas interaction. To reject these events, a cut is imposed on the vertex position.

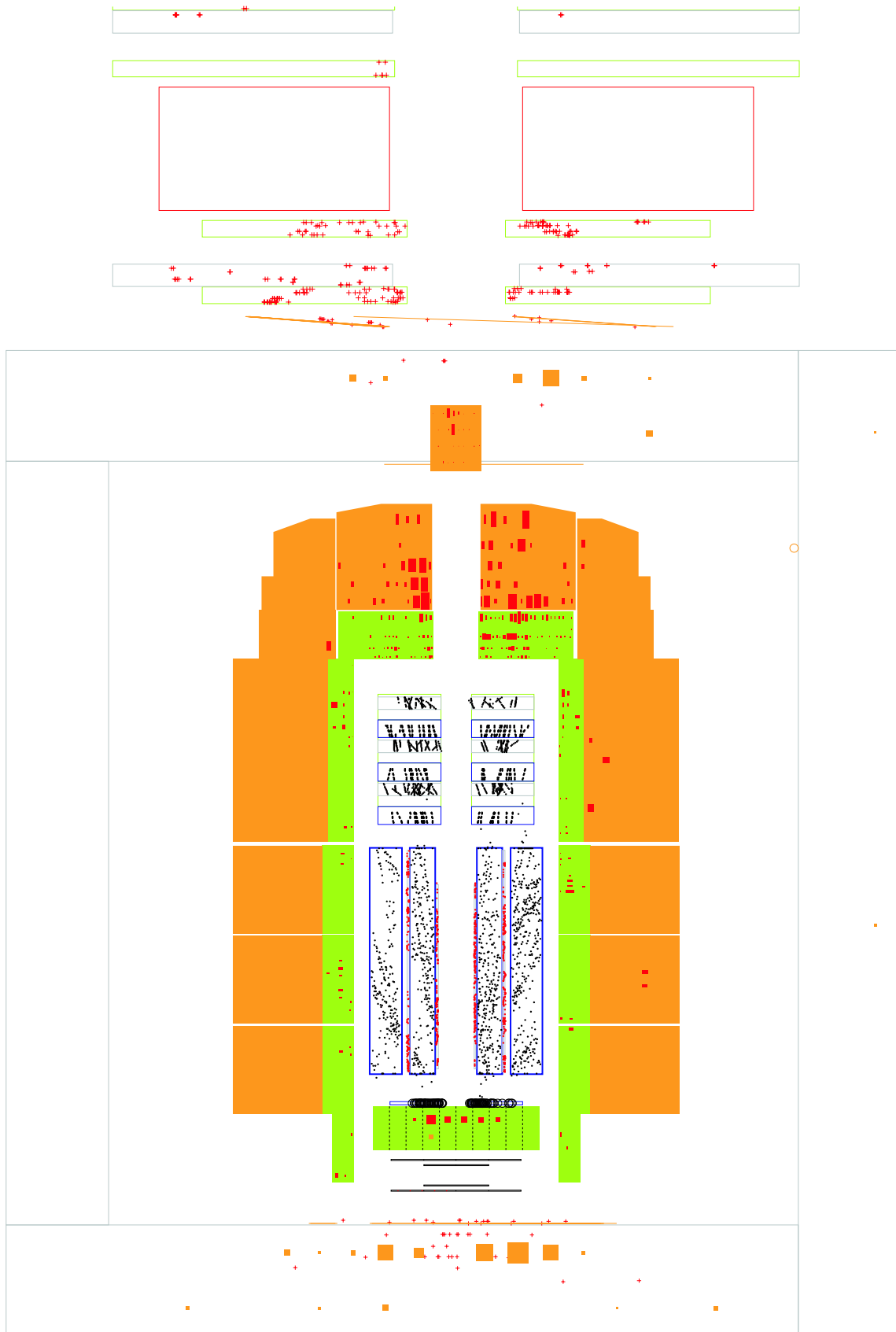


Figure 9.3: An H1 event display showing a beam-gas interaction. As is obvious from the figure, the primary vertex of the reaction is very much displaced from the nominal interaction point.

The length of a proton bunch is approximately 44 cm, and a positron bunch is 2.5 cm long. The distance between two bunches is a little less than 30 metres. Considering the finite time spread of the bunches, it is found that the interactions take place in an area of approximately 50 cm around the interaction point, giving rise to the cut

$$-25 \text{ cm} \leq z_{\text{vtx}} \leq 35 \text{ cm}. \quad (9.10)$$

The exact value of this cut stems from previous analyses (ex. [Dav01]).

9.4.3 Final State Object $\sum(E - p_z)$

Due to the inefficiencies of the detector, energy sometimes leaks undetected out of the detector. This happens, when a shower broadens enough, for the secondary particles to escape the instrumented material. Also it may happen that electronic noise is treated as a signal. In attempt to reject some of these events, the quantity $\sum_i(E_i - p_{z,i})$ can be used. i runs over all reconstructed objects in the final state. Considering the initial state of the positron and the proton, it is seen that

$$\begin{aligned} \sum_i(E_i - p_{z,i}) &= E_p - p_{z,p} + E_e - p_{z,e} \\ &\approx E_p - E_p + E_e - (-E_e) = 2E_e \\ &= 55 \text{ GeV}. \end{aligned} \quad (9.11)$$

By momentum conservation, this is also true after the collision. In the case of a perfect measurement, the sum of $E - p_z$ for all reconstructed particles (including the scattered positron) will be 55 GeV.

If, on the other hand, a hadron is misidentified as the scattered positron, the sum in equation (9.11) becomes smaller. Initial state radiation from the incoming positron as well as beam-gas or beam-wall can also distort this quantity. To suppress these events, a cut is imposed on the sum to be

$$35 \text{ GeV} \leq \sum_i(E_i - p_{z,i}) \leq 75 \text{ GeV}. \quad (9.12)$$

9.5 Kinematic DIS Selection

In the reconstruction of the kinematic variables of the event, the *electron method* is used. Detailed information on this method was given in section 3.1.1. The relevant variables are Bjorken- x (x_{bj}), the inelasticity (y) and the momentum transfer squared (Q^2).

The kinematic limits on Q^2 and y are set to

$$5 \text{ GeV}^2 \leq Q^2 \leq 75 \text{ GeV}^2 \quad (9.13)$$

$$0.1 \leq y \leq 0.7. \quad (9.14)$$

The Q^2 -cut makes sure that we are in fact selecting DIS-events (lower cut), while the upper cut ensures that it is feasible to find jets having $P_{t,jet}^2 \sim Q^2$.

The y -cut ensures a minimum inelasticity while at the same time making certain that the scattered positron is well within the SpaCal acceptance. The lower limit also cuts out the region of low resolution in x_{bj} (see equation (3.24)), while the upper limit corresponds loosely to the positron cuts in equations (9.4) and (9.5).

To create a well-defined region in Bjorken- x emphasising the low- x region, a cut in x_{bj} is imposed:

$$0.0001 \leq x_{bj} \leq 0.004 \quad (9.15)$$

Check-plots for the DIS-selection are shown in figure 9.4. As can be seen, the features of the data are quite accurately described by the ARIADNE, while RAPGAP does not provide the same level of accuracy.

9.6 Forward Jet Selection

We now consider events which have passed the DIS-selection, and which contain an energetic jet in the forward direction. Furthermore, we make a number of requirements on the properties of this forward jet.

Jets have been identified using the inclusive k_t -algorithm (see section 6.5). The algorithm has been run on objects, combining track information with energy deposits in calorimeter cells. These objects are referred to as Final State COMBined (FSCOMB) objects.

A forward jet must be found in the pseudorapidity interval:

$$1.735 \leq \eta_{jet} \leq 2.79 \quad (9.16)$$

This is a region in which the angular resolution is good enough to avoid mixing jets with the proton remnant. It corresponds to a θ -region of approximately $[7^\circ, 20^\circ]$.

To ensure good jet reconstruction while excluding noise and the proton remnant, a cut is made on the transverse momentum of the jet:

$$P_{t,jet} \geq 3.5 \text{ GeV} \quad (9.17)$$

To accomplish the suppression of DGLAP and thus to enhance sensitivity to BFKL-dynamics, a requirement is made that the transverse momentum of the jet be comparable in magnitude to Q^2 of the event:

$$0.5 \leq \frac{P_{t,jet}^2}{Q^2} \leq 2 \quad (9.18)$$

We now define x_{jet} as the energy fraction of the jet relative to the proton:

$$x_{jet} = \frac{E_{jet}}{E_p} \quad (9.19)$$

Additionally, we impose the following cut on x_{jet} :

$$x_{jet} \geq 0.035 \quad (9.20)$$

This combination of cuts ensures that the phase space for evolution in k_t is very small while at the same time demanding a larger space for evolution in x through the requirement $x_{jet} \gg x_{bj}$. Figure 9.5 shows a forward jet event. This is a very clean event. The jet is well-defined and there is little residual activity.

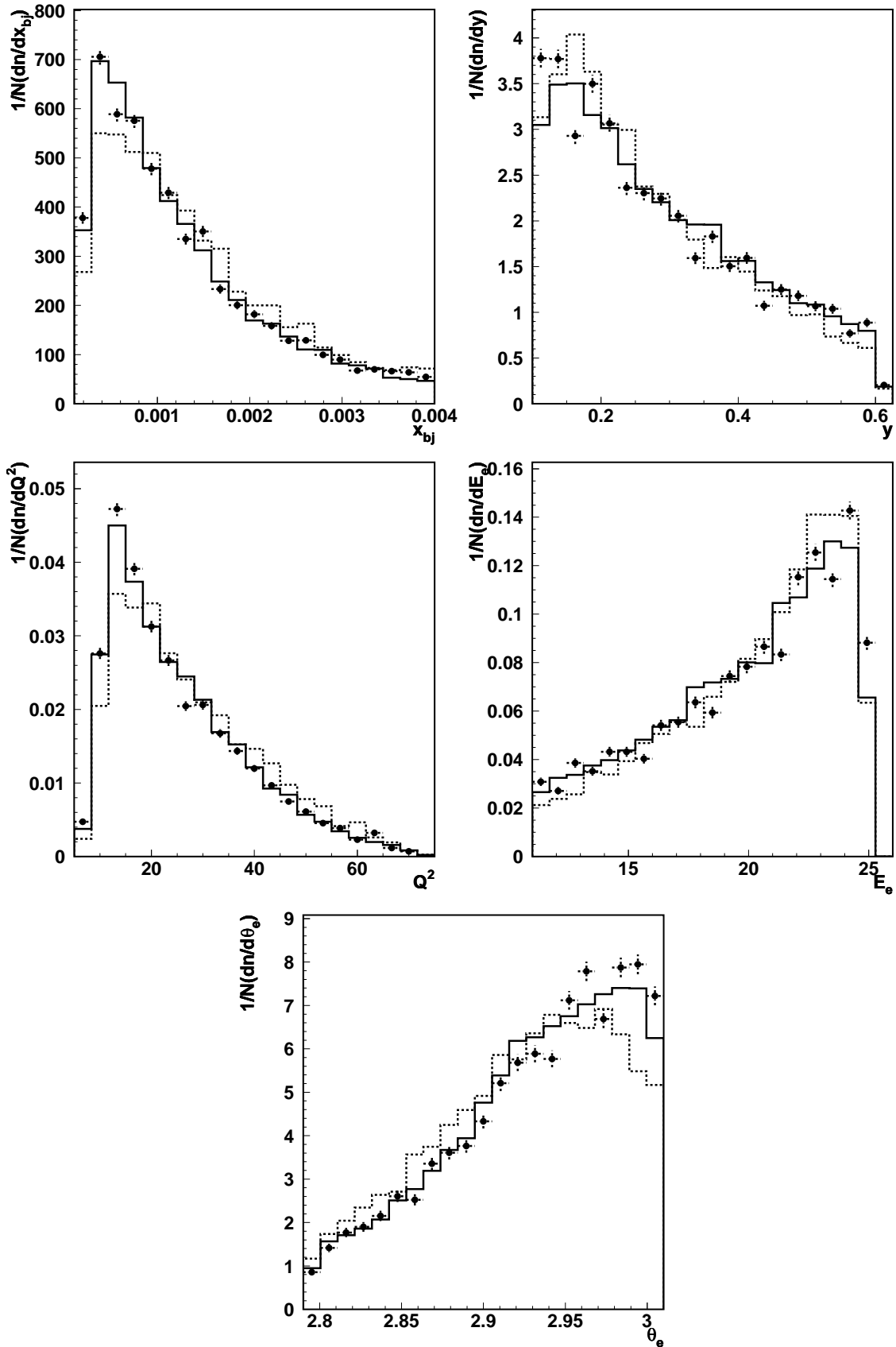


Figure 9.4: Check plots of kinematic quantities of the DIS-selection. Data points are compared to ARIADNE (solid line) and RAPGAP (dotted line).

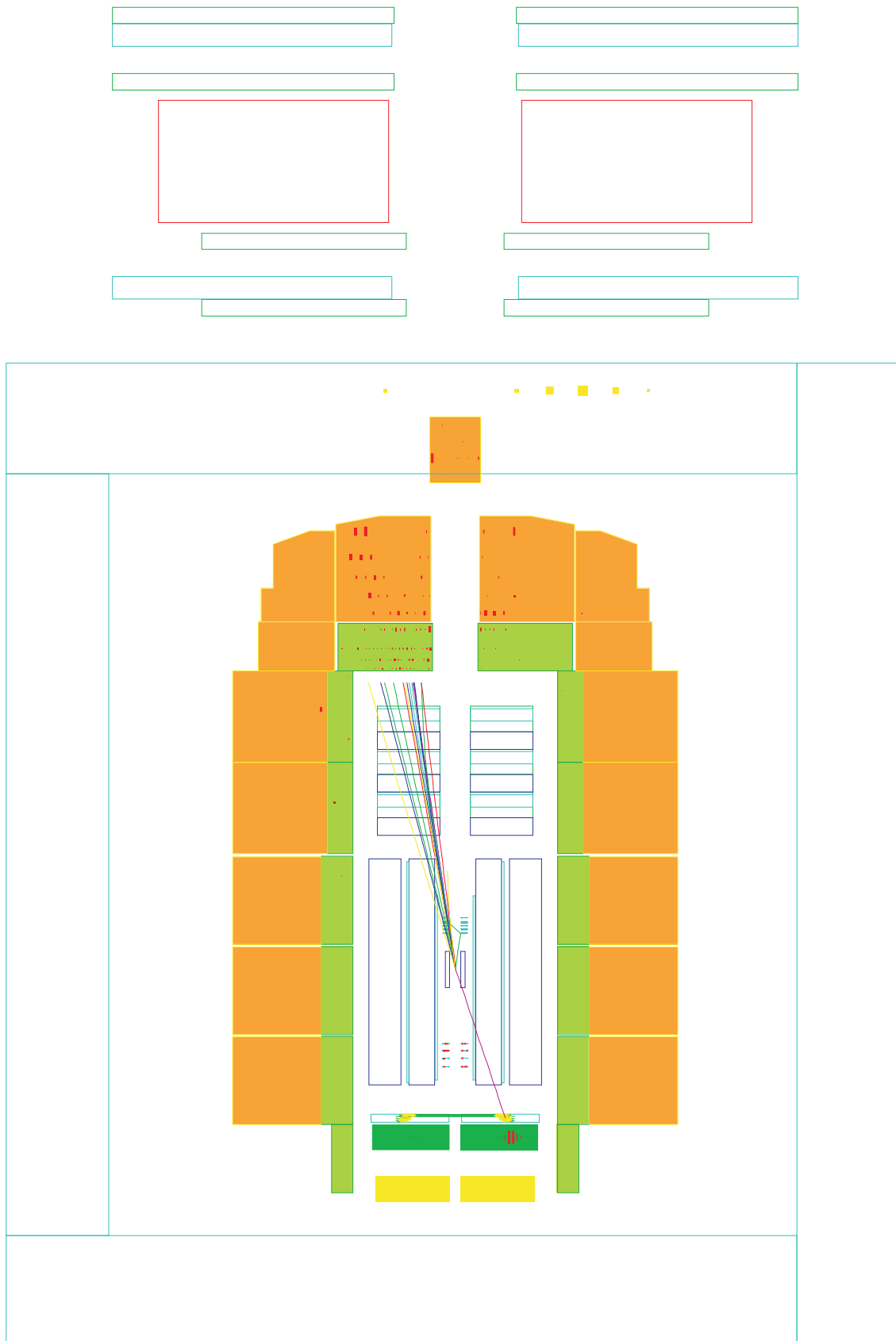


Figure 9.5: This event display shows an event which was selected by this analysis.

9.7 Evaluating the Forward Jet Event Selection

In order to understand the detector response, we need to perform the same event selection on a Monte Carlo sample, both for detector level and hadron level. We are then in a position to see, how much information “survives” the detector simulation, and to which extent the reconstructed sample is “polluted” with false events. The Monte Carlo sample used was a sample of ARIADNE Monte Carlo run through a full detector simulation [H1].

Furthermore, we need to establish the extent to which correctly reconstructed forward jet events have migrated from one bin to another in the variables that will be used in the cross section measurement.

We therefore define the following four quantities in each bin of the measurement:

- Purity:

$$P = \frac{N_{H \cap D}^{same}}{N_D}(H \cap D) \quad (9.21)$$

- Stability:

$$S = \frac{N_{H \cap D}^{same}}{N_H}(H \cap D) \quad (9.22)$$

- Background:

$$B = 1 - \frac{N_{H \cap D}}{N_D}(D) \quad (9.23)$$

- Acceptance:

$$A = \frac{N_{H \cap D}}{N_H}(H) \quad (9.24)$$

where N_D and N_H is the number of events found in a certain bin on detector level and on hadron level, respectively. $N_{H \cap D}$ is the number of events found on both hadron and detector level, and $N_{H \cap D}^{same}$ is the number of events found *in the same bin* on both detector and hadron level.

Purity and stability are calculated on an event-by-event basis from events passing both detector and hadron level selection. The background is calculated from events passing the detector level cuts, and the acceptance is calculated from events passing the hadron level cuts.

As can be seen from figures 9.6, 9.7 and 9.8, P and S are in general not below 0.6, except for the x_{jet} -plots, where they get as low as 0.5. This means that for those events that pass both selections, there is a good probability that the event is found in the same bin on both levels. This is an important point, as it will be established in section 9.8.3 that small bin migrations ensure that the bin-by-bin correction procedure works satisfactorily.

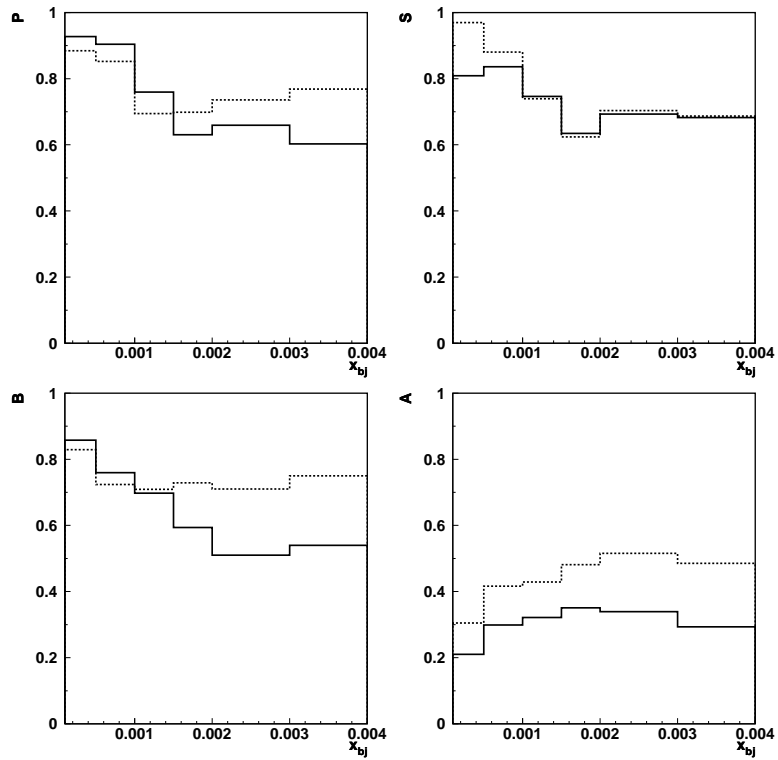


Figure 9.6: Purity, stability, background and acceptance in bins of x_{bj} .

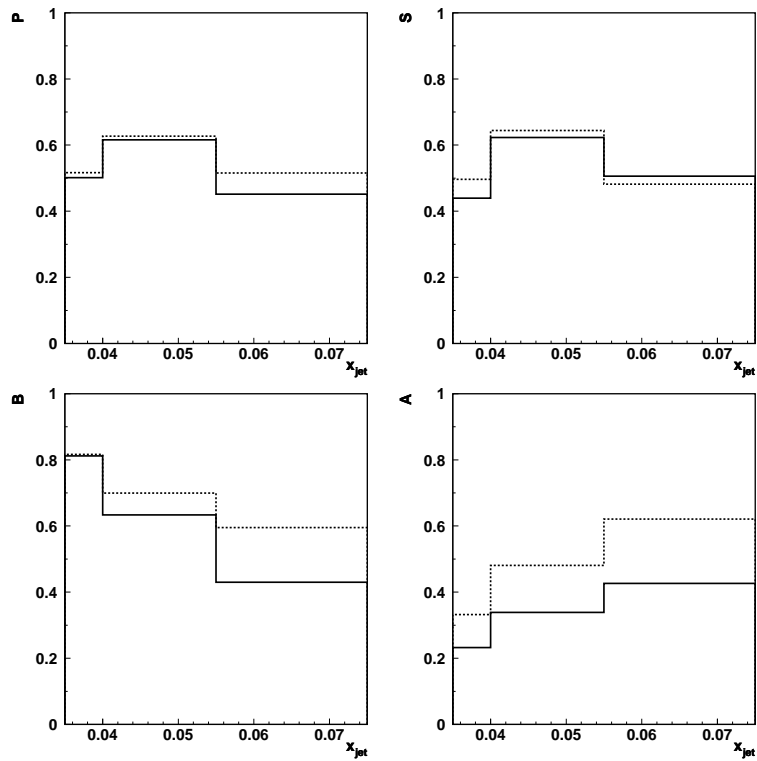


Figure 9.7: Purity, stability, background and acceptance in bins of x_{jet} .

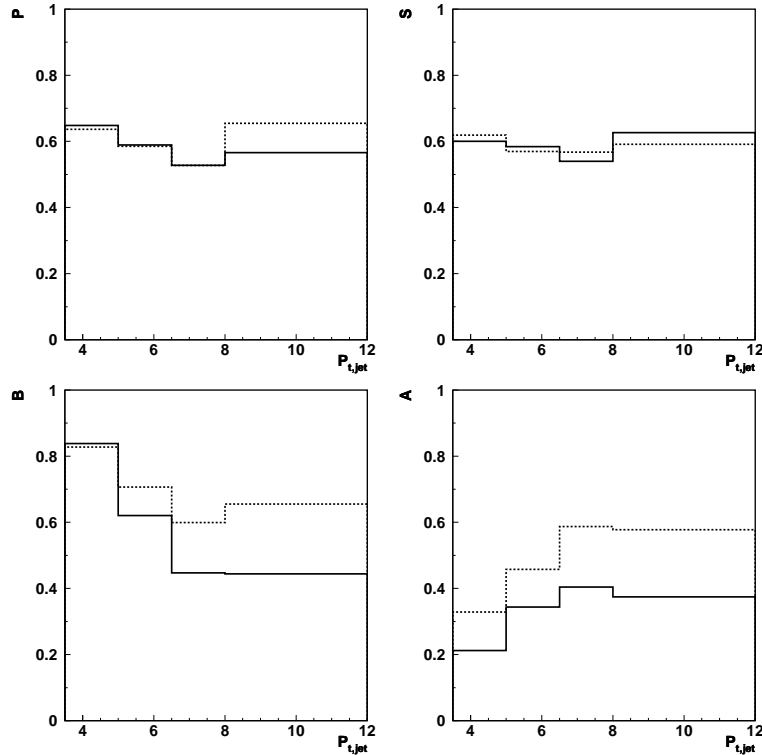


Figure 9.8: Purity, stability, background and acceptance in bins of $P_{t,jet}$.

To study in greater detail what actually happens in the bin migrations of the purity and stability, scatter-plots have been produced of x_{bj} , x_{jet} and $P_{t,jet}$ for events selected on both detector and hadron level. As can be seen in figure 9.9, x_{jet} and $P_{t,jet}$ are reconstructed quite consistently, although there is a certain spread. This is of course the reason for the coarse binning shown in the figure. Turning to x_{bj} one sees that the events split into two classes. There are those that are reconstructed with a quite high accuracy, and there are those which are reconstructed with too low a value. There is no evidence of a systematic error in the reconstruction, as that would appear as a “tilt” of the line away from the diagonal.

Remembering the definition of x_{bj} according to the electron method (equation (3.22) p. 18), it is seen that the x_{bj} -migrations translate directly into a study of Q^2 and y (we assume s to be known). Scatter-plots of Q^2 and y are seen in figure 9.10. As one can see, the resolution in Q^2 is excellent. The reconstruction of y , however, seems to bear the key to the x_{bj} -migrations. As equation (3.22) shows, too low a y -reconstruction will result in too high an x_{bj} , exactly as observed. We can therefore track the problem in the x_{bj} -reconstruction back to the reconstruction of y . This rests on the reconstruction of the scattered positron. In figure 9.11 plots are shown of E_e and θ_e . As can be seen, the angular resolution is excellent, whereas the energy is somehow reconstructed too high. It turns out that there is no correlation between badly reconstructed positron energy and the reconstructed angle. In other words *the correct positron candidate is selected*. However, the energy measurement is sometimes off. This could be due to photons or π^0 's hitting the same place as the positron, causing its energy to be incorrectly reconstructed.

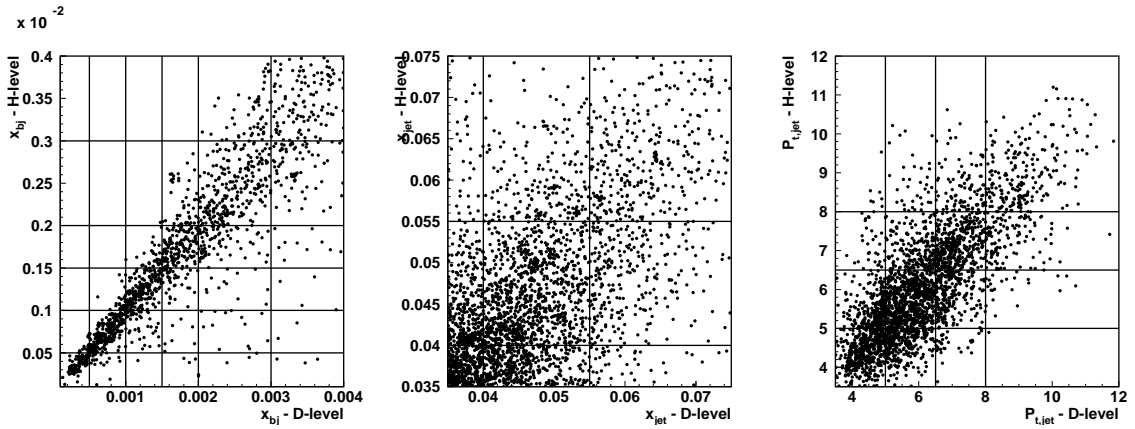


Figure 9.9: Scatter-plots of x_{bj} , x_{jet} and $P_{t,jet}$ (GeV) on hadron- vs. detector level. The x-axis is detector level, and the y-axis is hadron level. The grids in the plots indicate the binning that was chosen for the cross section measurement which is presented in the next chapter.

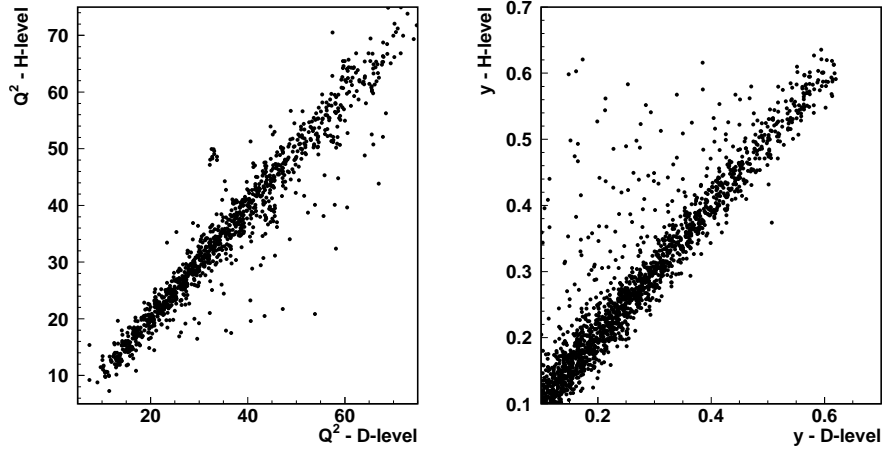


Figure 9.10: Scatter-plots of Q^2 (GeV^2) and y to study bin migrations.

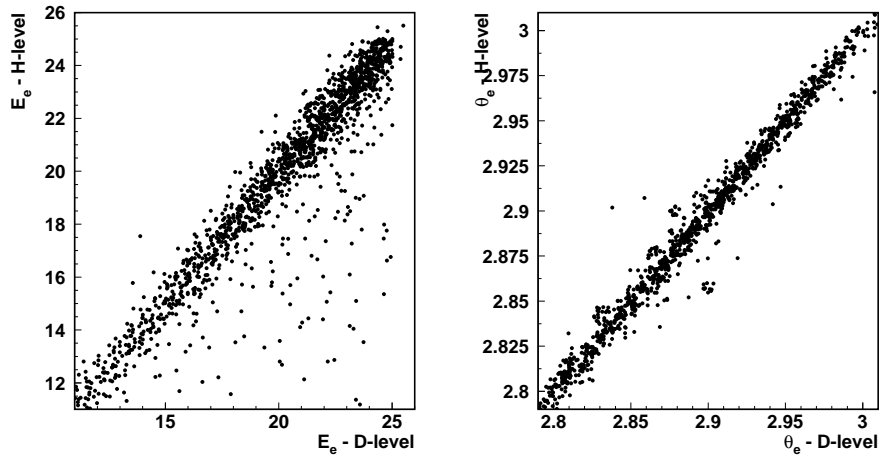


Figure 9.11: Scatter-plots of E_e (GeV) and θ_e (rad) to study bin migrations.

Turning to background and acceptance, the background is quite high. The interpretation of this is that a large fraction of the forward jet events found on detector level were not found on hadron level.

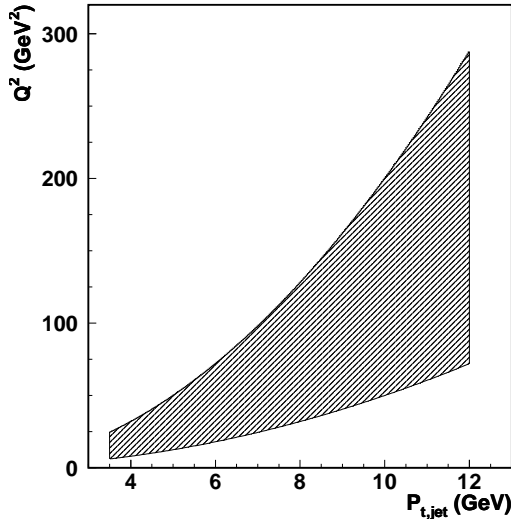


Figure 9.12: Q^2 -window as a function of reconstructed $P_{t,jet}$.

The acceptance is in many cases not very large. This has been observed in other analyses ([Lob97], [Kar02]). One possible explanation for this is the way that the $\frac{P_{t,jet}^2}{Q^2}$ -cut allows a smearing in $P_{t,jet}$ to affect the Q^2 -window. Figure 9.12 depicts the Q^2 -window as a function of the reconstructed $P_{t,jet}$. As can be seen, a finite $P_{t,jet}$ -resolution results in a quite drastic change in the allowed Q^2 -values. As figure 9.9 clearly shows, there is a very finite resolution in $P_{t,jet}$ which will certainly affect the available Q^2 -window.

9.8 Correcting for Detector Effects and QED Radiation

When performing a physics measurement in a detector, the result may be given as a distribution of one variable as a function of another. Looking strictly at the variables as a detector returns them, however, is not the best way to go about making predictions. What we are interested in is the underlying DIS event and the parton dynamics it expresses. What we see is an event smeared by finite detector resolution and inefficiencies. Also initial and final state interactions are of importance in DIS. These electroweak corrections will be treated in section 9.8.2

I will here present a method for unfolding detector level distributions to non-radiative hadron level. The procedure is referred to as the Bin-by-Bin correction method ([Wob00], [Kar02]). A more rigorous treatment may be found in [Cow].

9.8.1 Detector Corrections

No instrument possesses an infinite precision. This is true for a particle physics detector and so also for the H1 detector. An example of a measurement compared to the true value is shown in figure 9.13, which depicts the energy measurement of the scattered positron.

The left plot shows the energy distribution of the scattered positron with very loose cuts applied, whereas the right one shows only events that have passed the forward jet selection on both detector and hadron level.

As can be observed from the figure, the situation can be improved greatly through rejection of background by the appropriate event selection. An infinite precision is of course not possible, and the detector effects need to be corrected for when presenting a result.

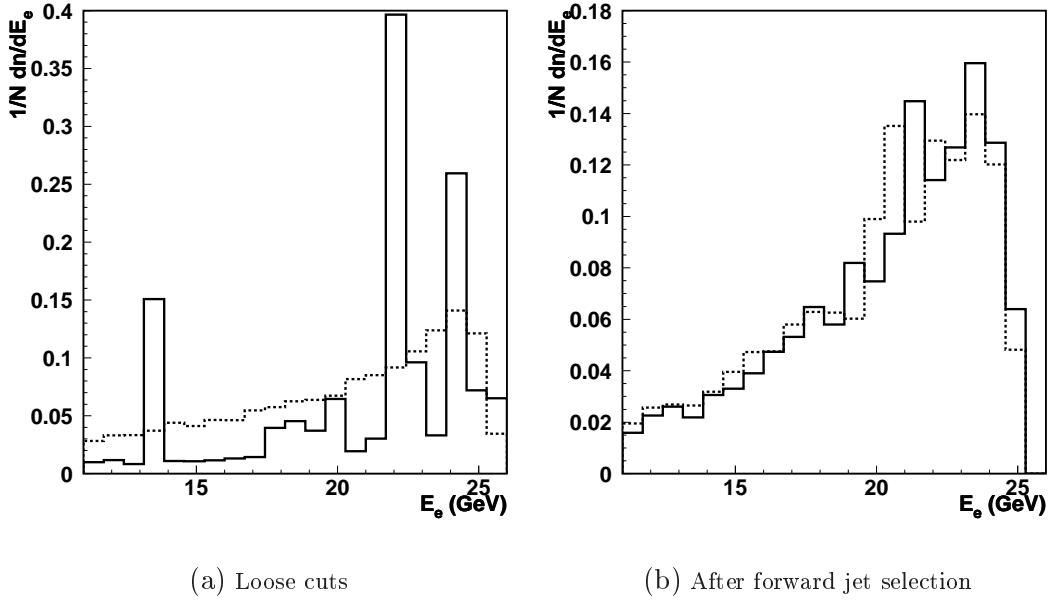


Figure 9.13: The energy distributions of the scattered positron are shown normalised to the number of events and to the bin-width. The solid line is detector level, and the dotted line is hadron level.

9.8.2 Radiative Corrections

A central part of analysing DIS events is an accurate knowledge of the various kinematic quantities. This is, however, complicated by higher order electroweak corrections.

These corrections divide into two groups:

- *Real corrections* where real photons are emitted by the incoming positron in either the initial or the final state. This is depicted in figure 9.14.

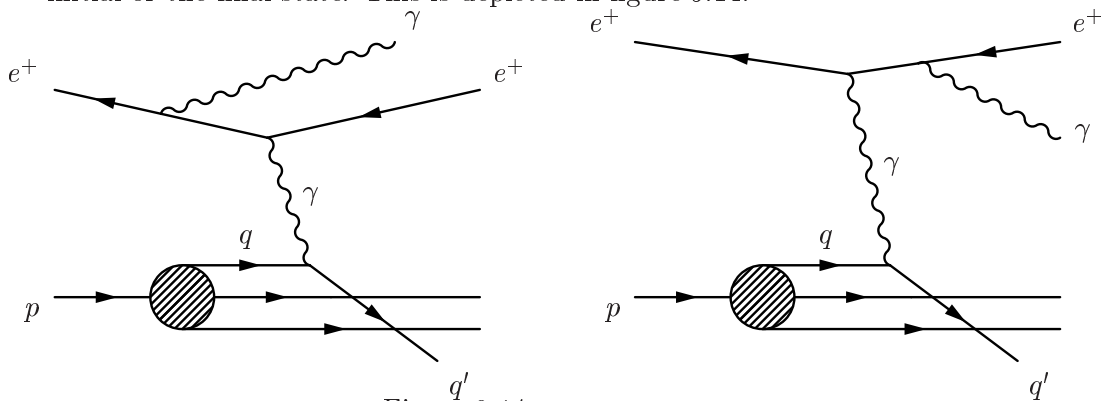


Figure 9.14: Real corrections.

- *Virtual corrections* in which electroweak loops occur. Examples of these are shown in figure 9.15.

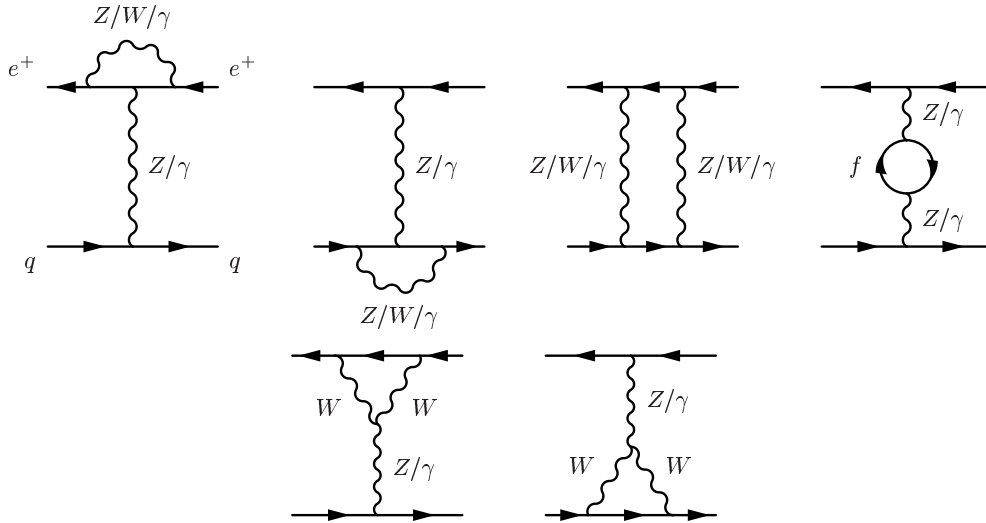


Figure 9.15: *Diagrams of virtual corrections. For brevity the diagrams have been divided into classes. Not all combinations of Z , W and γ are possible as suggested by some of the diagrams. The initial and final state limits which combinations are possible. The f represents any fermion loop.*

These corrections affect the measurement in several ways. First of all the cross sections change. The real corrections for example will quite clearly affect the reconstruction of the scattered positron and therefore change any cross sections measured in kinematic quantities measured therefrom. This is primarily relevant for initial state radiation. A photon emitted by the positron after the scattering will be close to collinear with the positron, and the two will still be reconstructed as one energy deposit.

Secondly, the event topology itself is altered, as for example collinearly emitted photons from the incoming positrons are lost in the beam pipe, changing the value of $\sum(E - p_z)$.

It can thus be concluded that for example photon bremsstrahlung cannot be accounted for using non-radiative Monte Carlo events. The simulated event *must* take the radiative corrections into account for a consistent correction.

9.8.3 Unfolding the Corrections

We now turn to the general problem of measuring a binned distribution x_i . We let \hat{x}_i denote the true value in the i th bin of the distribution.

The measured value of x_i is connected to \hat{x}_i through the *detector response function*:

$$x_i = \sum_j \mathcal{D}_{ij} \hat{x}_j \quad (9.25)$$

A complete unfolding of the distribution is connected to the inversion of the \mathcal{D} -matrix. This can rarely be done analytically. One may of course use a detector simulation to observe the effect of the detector response function on individual events and thus determine the \mathcal{D} -matrix itself. Inverting this matrix, however, can lead to unstable and oscillating solutions with large errors [Cow]. For this reason (and for simplicity) corrections are instead performed bin by bin in the present analysis.

If the bins of the distribution are chosen so that migrations are small between the bins, the detector response matrix can be approximated by a diagonal matrix. Having a diagonal response matrix, we can obtain the true distribution as

$$\hat{x}_i = x_i \mathcal{C}_{i,detector} \quad (9.26)$$

where the *correction factor* $\mathcal{C}_{i,detector}$ is obtained using generated events run through a detector simulation. It is given by the ratio between the generated value $y_{i,gen}$ and the reconstructed value $y_{i,rec}$:

$$\mathcal{C}_{i,detector} = \frac{y_{i,gen}}{y_{i,rec}} \quad (9.27)$$

Equation (9.26) corresponds to the x -distribution corrected for detector effects and acceptance.

Treating radiative corrections, we may go through a similar argument to conclude that we may correspondingly define

$$\mathcal{C}_{i,rad} = \frac{y_{i,no\ rad.\ cor.}}{y_{i,incl.\ rad.\ cor.}} \quad (9.28)$$

where both nominator and denominator represent generated quantities with and without radiative corrections, respectively.

The total correction factor is therefore defined:

$$\mathcal{C}_{i,total} = \mathcal{C}_{i,detector} \mathcal{C}_{i,rad} \quad (9.29)$$

Keeping in mind that detector corrections must be performed using Monte Carlo implementing radiative corrections, it is realised that $y_{i,gen} = y_{i,incl.\ rad.\ cor.}$. Consequently, the correction can be performed directly from detector level to non-radiative hadron level using the prescription:

$$\hat{x}_i = x_i \frac{y_{i,no\ rad.\ cor.}}{y_{i,rec}} \quad (9.30)$$

This is the method that has been used in this analysis.

The Bin-by-Bin correction method is not only applicable in the case where bin migrations are small. However, the price to pay for using the method in case of large migrations is the introduction of a bias, “pulling” the corrected value towards the Monte Carlo value [Cow].

It is seen that (at least) one of two requirements should hold true:

- Migrations between bins are small
- All aspects of the data are described by the reconstructed Monte Carlo sample

An estimate on the introduced bias (and hence on the model dependence of the correction) may be gained by comparing the corrected quantities by those obtained using a different Monte Carlo model. This estimate may then be considered a contribution to the systematic error.

Chapter 10

The Forward Jet Cross Section Measurement

In the following, a cross section measurement is presented on the basis of the described event selection. The forward jet cross section is measured as a function of x_{bj} , $P_{t,jet}$ and x_{jet} .

I will start with considering the detector level distributions. I will then address the problem of corrections for detector effects and radiative corrections. After this, the systematic error on the measurement will be estimated, whereupon the measurement will be presented.

10.1 Detector Level Distributions

The forward jet selection has been performed as described in section 9.6, using 13.72 pb^{-1} of data. Using the binning indicated in figure 9.9, the distributions shown in figure 10.1 were obtained.

The data were compared to two Monte Carlo samples, namely ARIADNE and RAPGAP DIR. Both samples have been run through a full detector simulation, whereupon the forward jet selection has been performed.

Only the pure DGLAP point-like photon has been included in the RAPGAP-prediction, and comparison with data shows, that it fails in describing the data. ARIADNE, on the other hand, does a fairly decent job of describing the features of the data distributions.

The failure of RAPGAP DIR to describe the forward jet distributions is an initial confirmation that DGLAP dynamics *have* indeed been suppressed due to the forward jet selection.

As these plots are on detector level, they are highly coupled to the H1-detector and the H1-toolkits. To compare with physics models in general, detector effects must be unfolded along with radiative corrections, so that all predictions are given on non-radiative hadron level. This will be done in section 10.2.

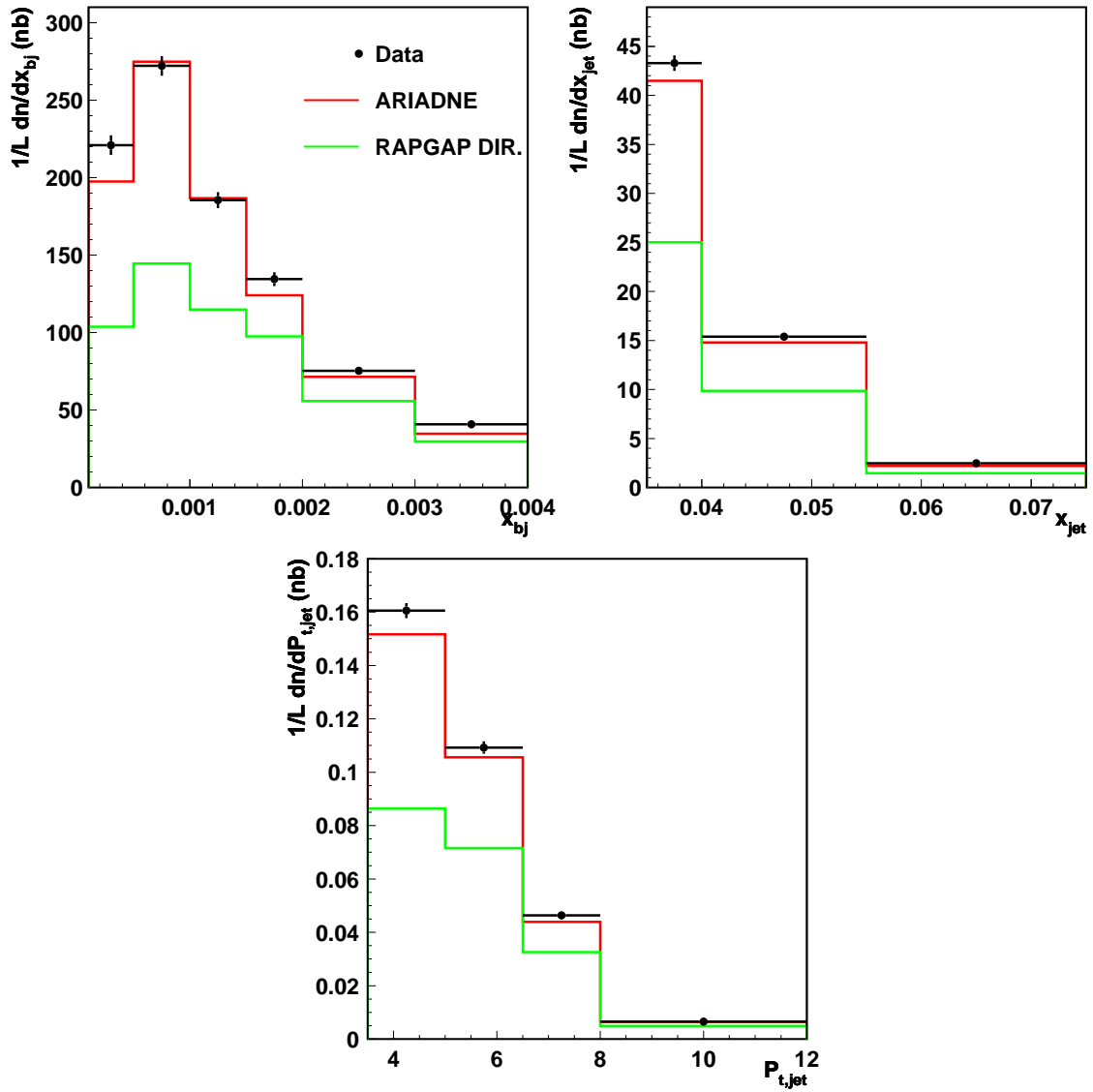


Figure 10.1: Detector level distributions of forward jet events in x_{bj} , x_{jet} and $P_{t,jet}$. The distributions have been normalised to the Luminosity and the bin-width.

10.2 Detector Corrections

The data are corrected to non-radiative hadron level using the Bin-by-Bin correction method as described in section 9.8.3.

As was seen in section 9.7, the migrations between the chosen bins are quite small. Furthermore, it is seen that events generated with ARIADNE and passed through the full detector simulation, describes the data quite satisfactorily. The corrections were therefore carried out using two samples of ARIADNE Monte Carlo, namely a non-radiative hadron level sample (corresponding to $y_{i,no\ rad.\ cor.}$ in equation (9.30)) and a reconstructed radiative sample ($y_{i,rec}$). The correction factors are shown in figure 10.2. Shown here are also the correc-

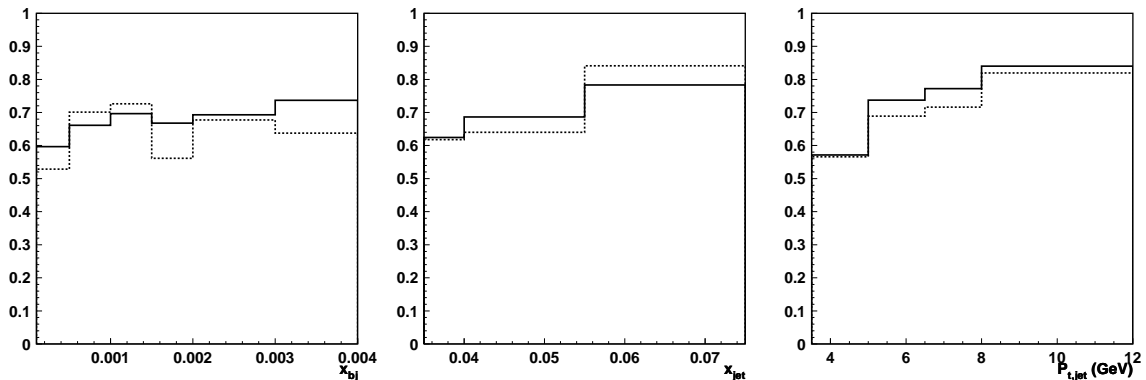


Figure 10.2: The correction factors for the cross section measurement. The solid line represents ARIADNE, whereas the dotted line represents RAPGAP DIR.

tion factors obtained using RAPGAP DIR. The RAPGAP sample was used to estimate the systematic error induced by the correction as discussed in section 9.8.3.

10.3 Treatment of Systematic Errors

Systematic errors from a variety of sources have been estimated. In several situations, this has given rise to errors that vary from bin to bin and errors that are asymmetric. The individual systematic errors have been added in quadrature on the assumption that they are independent.

I will here present the investigated contributions to the systematic error.

The energy scale of the LAr calorimeter: The energy scale of the LAr calorimeter is known to within $\pm 4\%$ (see section 8.3.1). To check the consequences of this on the forward jet measurement, the analysis was run on Monte Carlo with a shift of $\pm 4\%$ in the scale of the LAr calorimeter. The change in the correction factor was then applied as a percentual systematic error. The average value of the systematic error induced was $+8\%/-3\%$.

Model dependence of correction procedure: As can be seen in figure 10.2, the correction factors will change if the correction is applied using the RAPGAP Monte Carlo sample.

As discussed in section 9.8.3 a comparison between the two sets of correction factors will give an estimate of the induced bias and thus the systematic error from the correction. The changes in correction factors and thus the systematic errors were on average $+5\%/-4\%$, but in certain bins of the distributions, the systematic error from model dependence reached as much as 10%.

The energy scale of the SpaCal: Varying the energy scale of the SpaCal within the limits of $\pm 1\%$ (the uncertainty in energy scale, see section 8.3.2) and running the analysis on Monte Carlo, the average contributions to the systematic error obtained were $+3\%/-1\%$.

The angular resolution of the reconstructed positron: As the angle of the reconstructed positron is known to within ± 2 mrad (section 8.3.2), the analysis was run on Monte Carlo varying the angle with that amount. This resulted in an average systematic error of $+2\%/-1\%$.

The luminosity uncertainty: The luminosity is known to 1% accuracy (section 8.4). This translates directly into a 1% uncertainty on the differential cross section.

10.4 The Corrected Differential Cross Section

After the correction of the data from detector level to non-radiative hadron level, the final hadron level cross sections are plotted in figure 10.3. Shown in the plots are the statistical errors with tick marks on the error bars. The full error bar represents the statistical error added to the systematic error in quadrature. The individual contributions to the systematic error were added in quadrature. This procedure relies upon the assumption that the individual contributions are uncorrelated.

Looking at the comparisons to the different Monte Carlo predictions, ARIADNE continues to describe the data well. Correspondingly, RAPGAP DIR continues to fail in its description.

Turning to RAPGAP DIR+RES, it is seen that the DGLAP approach of RAPGAP may in fact be brought to excellent agreement with the data by including a resolved photon component. The resulting “double DGLAP” evolution is therefore a contender in the description of the forward jet cross section.

In the plots, comparison is also made to CASCADE using two different calculations of the unintegrated gluon density. What is seen is that there is a very significant difference between the two sets. This can not be attributed to the difference in the soft regions alone, but must also in part be due to the inclusion of the full gluon splitting function in Set 2 (see section 5.2). CASCADE Set 1 consistently overshoots the data, which was a behaviour also observed for earlier calculations of the unintegrated gluon density [Kar02], although it is here significantly reduced. CASCADE Set 2 seems to underestimate the cross section in the soft region, while there is better agreement with the data for harder jets and larger values of x_{bj} .

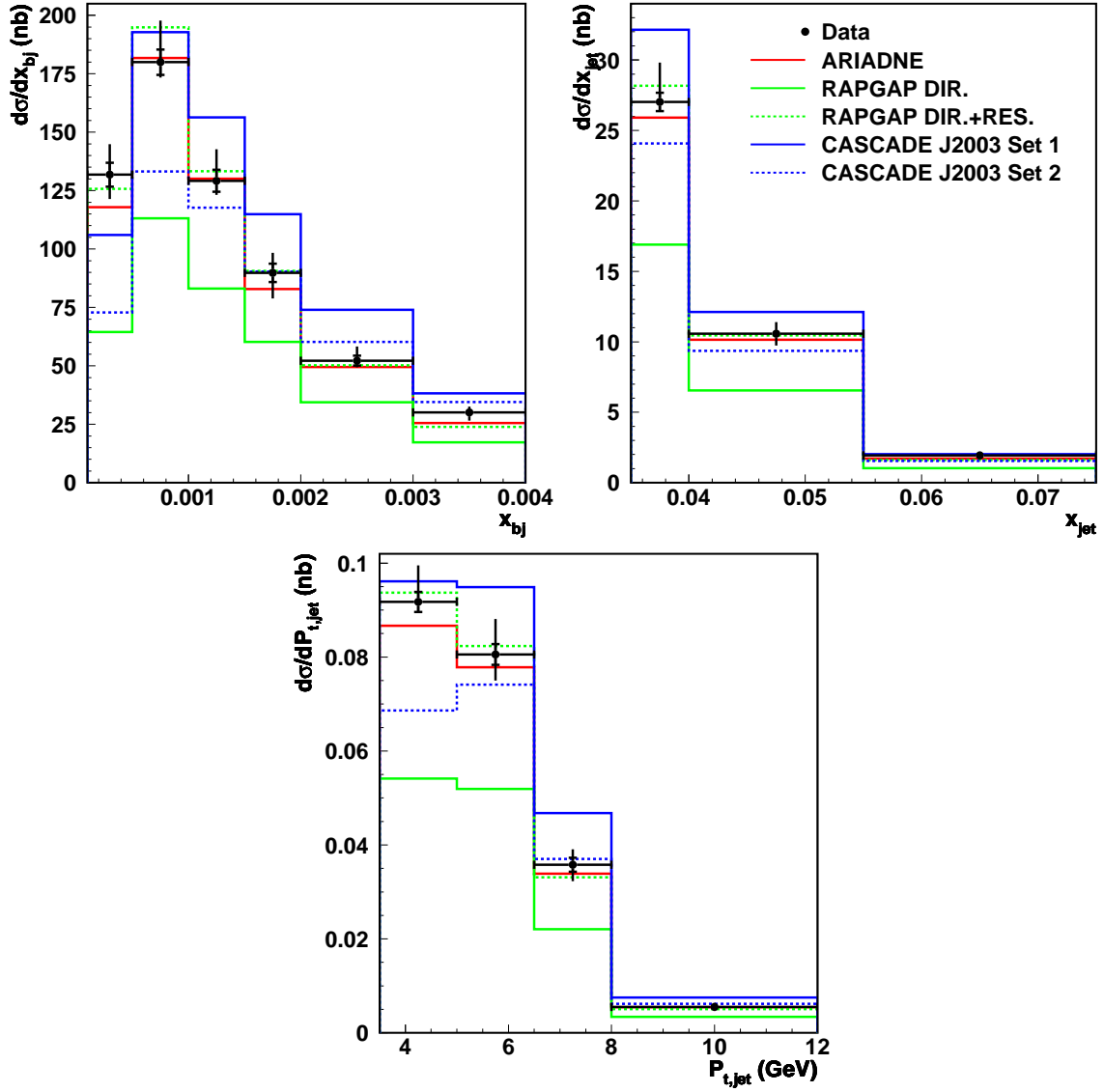


Figure 10.3: Shown here are the differential cross sections in x_{bj} , x_{jet} and $P_{t,jet}$ corrected to non-radiative hadron level. The data are compared to ARIADNE, RAPGAP DIR, RAPGAP DIR+RES and CASCADE using two different sets of unintegrated gluon densities (see chapter 5 for details on this).

Chapter 11

Discerning Models Through Event Variables

Having selected the forward jet events and drawn some preliminary conclusions from the cross section measurement, it is of interest to look at the individual selected forward jet events and try to discern between the different models on the basis of event variables and per-event distributions.

The following variables and distributions have been considered:

Transverse energy flow: In an H1 study [H103a], forward π^0 -production was studied with cuts similar to the forward jet cuts applied here. The major difference was the absence of a “ $p_t \sim Q^2$ ”-cut.

In this study the transverse energy flow around the π^0 was measured with the conclusion that DGLAP failed to describe the pedestal of the π^0 -peak, whereas the resolved photon approach and CCFM tended to give a better description.

The transverse energy flow is exactly a way to investigate in detail the dynamics of the parton cascade, where the k_t -dynamics is a central difference between the different models.

Jet profiles: In 1998, it was observed in a ZEUS study [ZE99] that when looking at the forward jet profiles in bins of the forward jet pseudorapidity there was a significant broadening of the forward jet as a function of η . It has therefore been investigated whether a similar broadening can be observed here.

p_t -spectrum: To get a clearer idea of which model does the better job of describing the parton cascade of the events, a p_t -spectrum has been calculated of the selected events and compared to models.

The different variables have been measured at detector level and corrected to non-radiative hadron level using the same ARIADNE sample that was used to correct the cross section measurement. The systematics on the final corrected quantities were estimated and added using the same prescriptions as in 10.3 and 10.4.

11.1 Transverse Energy Flow

As the forward jet carries a significant amount of the energy in the selected events, the transverse energy flow around the jet has been investigated in detail.

Bin 1	$1.735 < \eta_{\text{forward jet}} < 2.50$
Bin 2	$2.50 < \eta_{\text{forward jet}} < 2.65$
Bin 3	$2.65 < \eta_{\text{forward jet}} < 2.79$

Table 11.1: Definition of the bins in forward jet pseudorapidity, η .

The events were first sorted in three bins of forward jet pseudorapidity, as seen in table 11.1. The bins were chosen to have approximately the same statistics. Figure 11.1 shows, that the resolution in $\eta_{\text{forward jet}}$ is good enough for this binning to make sense. The figure shows, that migrations between bins from hadron level to detector level are within reasonable limits.

For each event, the transverse energy flow was then calculated as a function of the pseudorapidity of each particle and the distance to the forward jet axis in units of pseudorapidity.

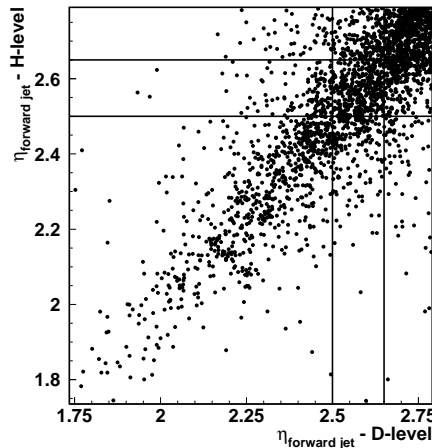


Figure 11.1: Scatter-plot showing $\eta_{\text{forward jet}}$ at detector vs. hadron level

11.1.1 Detector Level

At detector level, FSCOMB objects were used, as these were also the detector level objects used in the jet-finding.

In figure 11.2, the detector level distributions of the transverse energy flow is shown. The distributions have been normalised to the number of events in each $\eta_{\text{forward jet}}$ -bin and to the bin width.

The forward jet pseudorapidity increases from left to right. The top plots show the E_t -flow as a function of $\Delta\eta$, whereas the bottom plots show it as a function of η in the lab-frame. Note that the calorimeter edge is clearly marked by the sharp drop in the last bin of the top right plot.

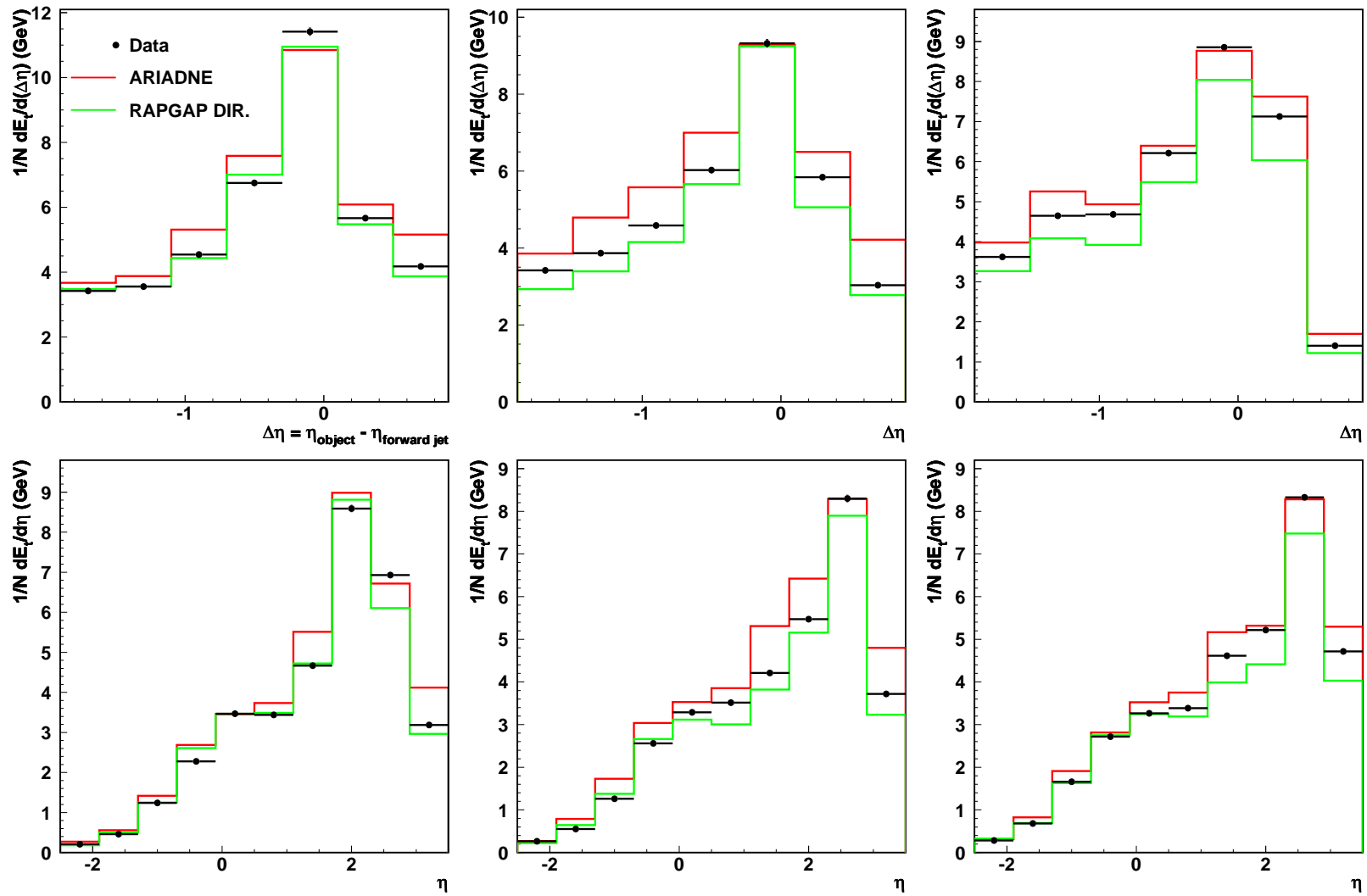


Figure 11.2: Detector level distributions of transverse energy flow. Data are compared to reconstructed ARIADNE and RAPGAP DIR. The plots are organised with ascending $\eta_{\text{forward jet}}$ to the right.

11.1.2 Corrections

The correction follows the same procedure as was used for the cross section measurement. As ARIADNE was used to correct the cross section measurement it was also used here. Of course it is harder to define “bin migrations” exactly, and we expect a larger smearing on a distribution of this level of complexity anyway. As neither ARIADNE nor RAPGAP DIR do a perfect job in describing the data, we must expect larger systematic errors on the corrected distributions as a result.

I will not be showing all the correction factors, but merely a small sample. In figure 11.3, the correction factors are shown for Bin 2 in forward jet pseudorapidity.

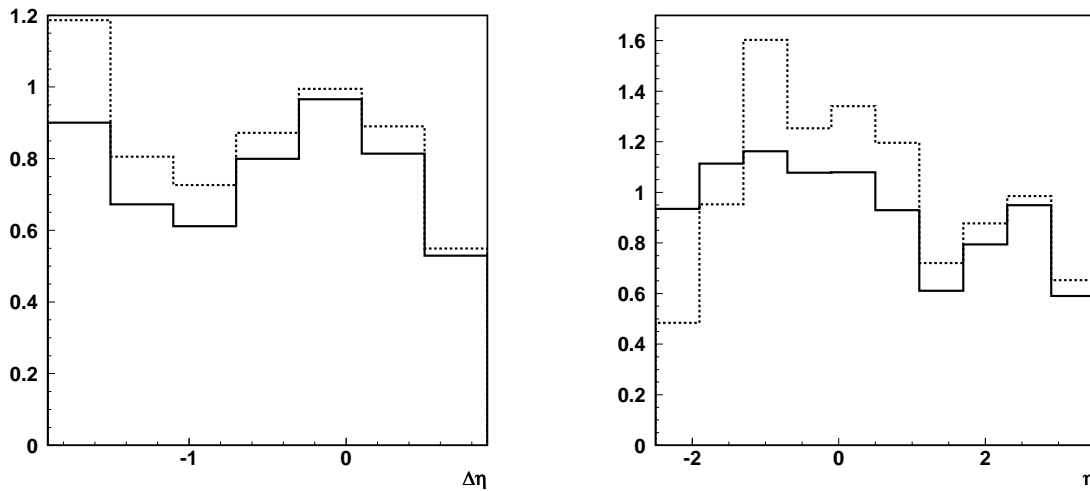


Figure 11.3: *Correction factors for the E_t -flow. The solid line represents ARIADNE, whereas the dotted line represents RAPGAP DIR.*

As can be seen from the figure, the correction factors in some bins are as much as 60% from unity. As the two generators also disagree heavily in many bins, this points to large systematic errors.

11.1.3 Systematics

The same contributions to the systematic error were considered, as was done in section 10.3. The luminosity, though, has of course been disregarded (The E_t -flow is a per-event quantity). As it turns out, there are quite large contributions to the systematic error. These contributions stem mainly from the model dependence, as indicated in figure 11.3.

The problem seems generally to be due to the fact that neither of the two generators describe the data accurately. This is especially true for the central η -range around $\eta = 0$. One might argue that RAPGAP DIR should be preferred over ARIADNE on the basis that it actually is better than ARIADNE in many regards when considering the detector level distributions. I decided against this on the basis that consistency in the correction procedure is desirable. Furthermore, the difference between the models would be the same, resulting in the same systematic error.

11.1.4 Results

Figure 11.4 shows the corrected transverse energy flow in coordinates of $\Delta\eta$. In figure 11.5 is correspondingly shown the E_t -flow as a function of η . The measurements are compared to the same five Monte Carlos as was done for the cross section. The χ^2 -values for the different Monte Carlo generators relative to the data are listed in table 11.2.

For $\frac{dE_t}{d\Delta\eta}$ (7 bins) the three central bins have been defined as the *jet region* (bins 4-6). The rest is defined as *pedestal*. For $\frac{dE_t}{d\eta}$ (10 bins), bins 8-9 define the jet, and the rest is attributed to the pedestal. The χ^2 -values have not been divided by the number of bins. Instead the number of bins (Degrees Of Freedom) is indicated at the bottom. The maximum sensitivity is hinted by the χ^2 -values, as they would look in the absence of systematic errors.

$\frac{dE_t}{d\Delta\eta}$	Pedestal	Jet	Total	$\frac{dE_t}{d\eta}$	Pedestal	Jet	Total
<hr/>							
1.735 < η_{jet} < 2.5							
ARIADNE	5.15	3.30	8.45		6.84	1.08	7.92
RG-DIR	2.50	3.18	5.68		5.00	1.11	6.11
CASCADE Set 1	1.39	0.96	2.36		3.05	2.92	5.97
CASCADE Set 2	7.33	1.75	9.68		7.09	2.71	9.80
<hr/>							
2.5 < η_{jet} < 2.65							
ARIADNE	7.46	2.40	9.87		6.56	1.53	8.08
RG-DIR	1.28	0.55	1.83		4.34	0.58	4.92
CASCADE Set 1	3.84	0.83	4.67		3.21	0.97	4.18
CASCADE Set 2	0.29	2.02	2.32		2.93	0.81	3.74
<hr/>							
2.65 < η_{jet} < 2.79							
ARIADNE	2.33	0.58	2.91		3.02	0.06	3.08
RG-DIR	1.51	3.50	5.01		2.96	2.77	5.74
CASCADE Set 1	3.73	6.26	9.99		3.85	2.87	6.72
CASCADE Set 2	5.84	10.80	16.64		3.76	9.04	12.80
<hr/>							
No Systematics							
ARIADNE	10.02	6.96	16.98		16.79	1.47	18.26
RG-DIR	8.47	6.13	14.61		27.19	1.89	29.08
CASCADE Set 1	3.11	1.90	5.01		7.90	5.53	13.43
CASCADE Set 2	9.12	3.15	12.27		12.53	6.16	18.68
<hr/>							
2.5 < η_{jet} < 2.65							
ARIADNE	18.47	8.18	26.65		27.76	6.71	34.46
RG-DIR	6.23	1.59	7.82		32.49	2.17	34.66
CASCADE Set 1	17.99	1.51	19.51		17.00	2.25	19.25
CASCADE Set 2	0.40	2.91	3.31		6.75	1.35	8.11
<hr/>							
2.65 < η_{jet} < 2.79							
ARIADNE	5.13	1.74	6.86		11.00	0.11	11.11
RG-DIR	1.79	5.21	7.00		18.32	4.42	22.74
CASCADE Set 1	12.30	9.91	22.21		17.52	6.36	23.87
CASCADE Set 2	6.69	16.13	22.82		4.85	14.71	19.56
<hr/>							
DOF	4	3	7		8	2	10

Table 11.2: χ^2 for the different Monte Carlos relative to the data. The upper half of the tabular includes the full treatment of systematics, whereas the bottom half only includes the statistical error. Entries marked with red have a probability of compatibility with the data of less than 5%.

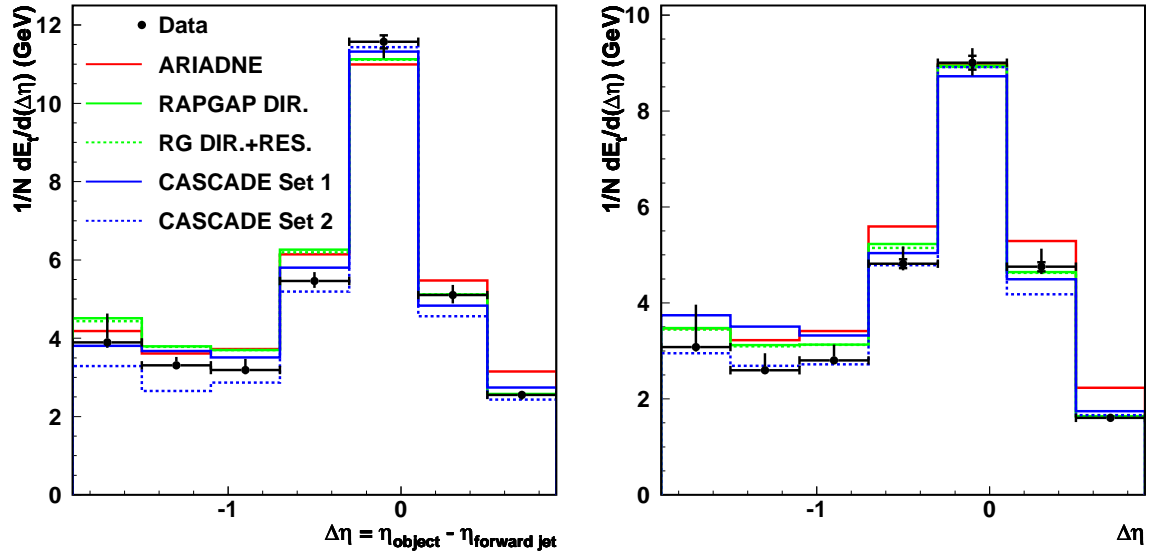
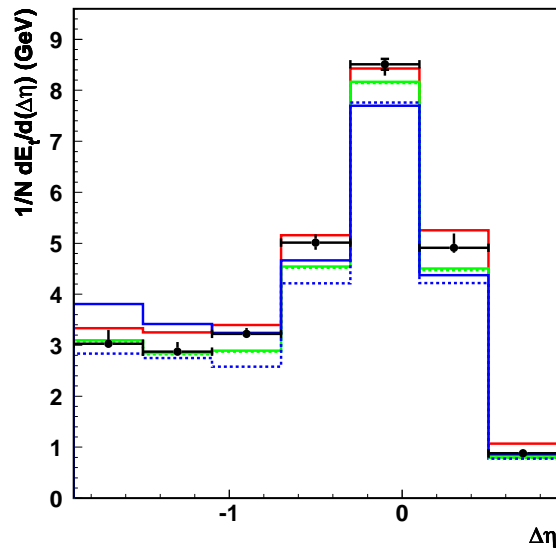
(a) $1.735 < \eta_{\text{forward jet}} < 2.5$ (b) $2.5 < \eta_{\text{forward jet}} < 2.65$ (c) $2.65 < \eta_{\text{forward jet}} < 2.79$

Figure 11.4: Transverse energy flow relative to the forward jet. The data are compared to ARIADNE, RAPGAP DIR, RAPGAP DIR+RES and CASCADE, using two different sets of unintegrated gluon densities (see chapter 5 for details on this).

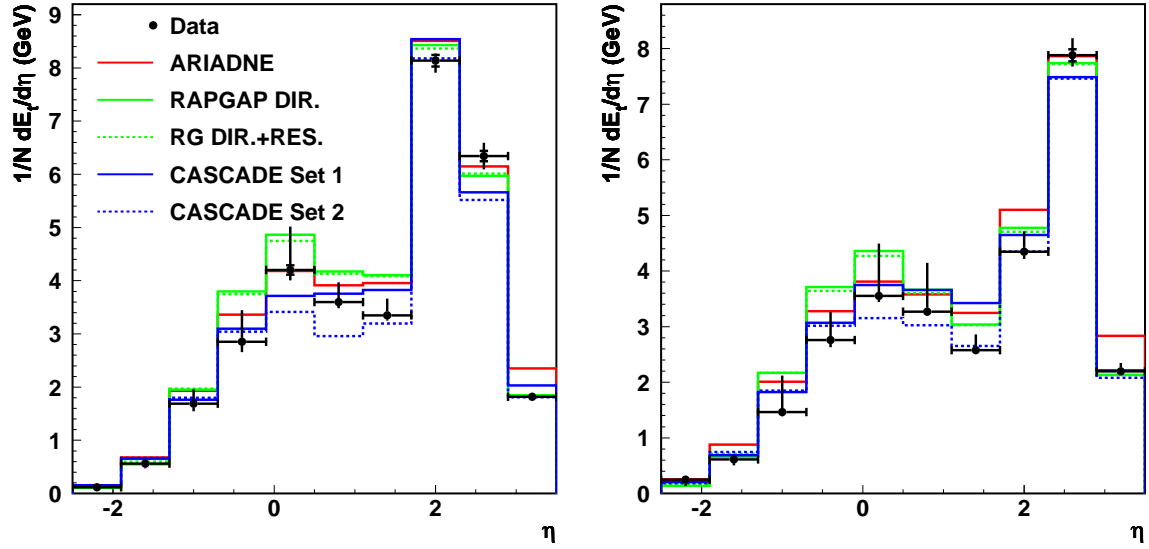
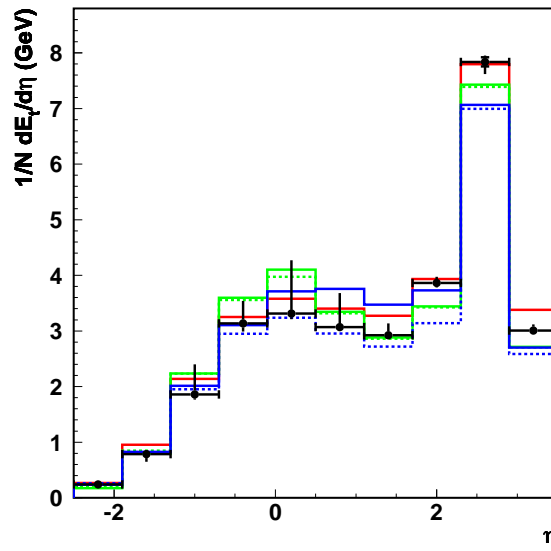
(a) $1.735 < \eta_{\text{forward jet}} < 2.5$ (b) $2.5 < \eta_{\text{forward jet}} < 2.65$ (c) $2.65 < \eta_{\text{forward jet}} < 2.79$

Figure 11.5: Transverse energy flow in absolute η -coordinates. The same data Monte Carlo comparisons are carried out as in figure 11.4.

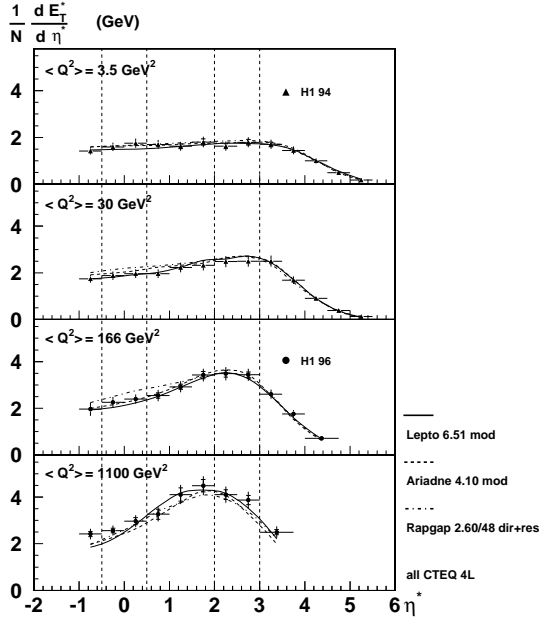


Figure 11.6: Transverse energy flow in inclusive DIS [H100].

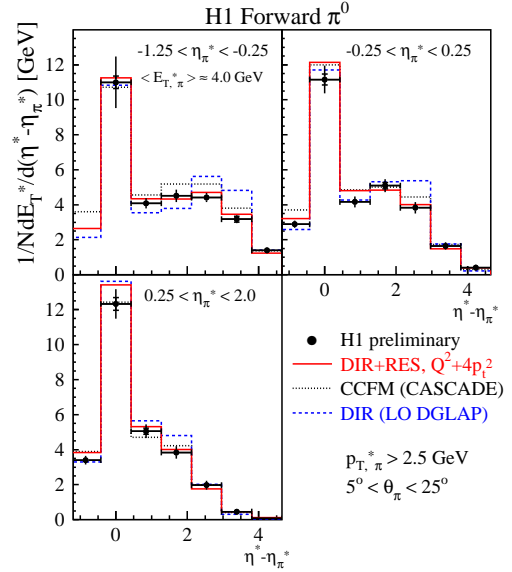


Figure 11.7: Transverse energy flow around a forward π^0 , [H103a]. Data (points) are compared to RAPGAP DIR. (blue), RAPGAP DIR + RES (red) and CASCADE (black).

A comparison can be made between these plots and the corresponding plots for inclusive DIS made by H1 for example in [H100]. I have included a figure from that paper as figure 11.6, comparing it to figure 11.5. Note that the energy flow is here measured in the hadronic centre-of-mass frame (see section 3.1.2). A direct shape comparison therefore does not make sense. One observation, however, is that the pedestal away from the jet turns out to be significantly higher in the forward jet sample than in the inclusive DIS sample considered in [H100].

I have also included the plot corresponding to figure 11.4 from the forward π^0 -study of H1 [H103a] in figure 11.7. Again it should be noted that a direct shape comparison between the forward jet plots and the pion plots is not possible, due to the fact that the pion plots are in the hadronic centre-of-mass frame. The only thing that may be directly inferred is that the pedestal of transverse energy in the immediate vicinity of the forward π^0 tends to be a bit higher than the corresponding pedestal for the forward jet. This might simply be a consequence of the π^0 reconstruction. To successfully reconstruct a π^0 , there must necessarily be an *isolated* electromagnetic shower in the calorimeter. The isolation requirement is not present in the jet-analysis, and the π^0 -selection thus contains an inherent bias towards lower transverse energy flows.

Turning to direct model comparison, I will now treat the generators individually.

ARIADNE: When looking at the E_t -flow, it seems that ARIADNE provides an approximate description of the data at low and high values of $\eta_{\text{forward jet}}$ (figure 11.4(a), 11.4(c)). However, in the intermediate $\eta_{\text{forward jet}}$ -range (figure 11.4(b)), the description of the pedestal

on both sides of the forward jet tends to deteriorate. This was also the case for the detector level distributions (figure 11.2). The observation is supported by table 11.2, although it is seen that the variations are diminished by the large systematics.

In all cases ARIADNE seems to predict a broader jet than do the other models. Also, it has a tendency to overshoot the data.

RAPGAP: There is surprisingly little difference between the standard DGLAP approach and DGLAP with the resolved photon included. This is in contrast with the forward pion study in figure 11.7, where a difference is visible. The two RAPGAP samples will here not be treated independently.

Generally speaking, it seems that RAPGAP has a problem with describing the central parts of the detector. This leads to an overestimation of the jet pedestal in figures 11.4(a) - 11.4(b). Note that the dip at $1.5 < \eta < 2$ is also badly described here (figures 11.5(a), 11.5(b)).

At higher forward jet pseudorapidities, the description improves somewhat in the pedestal. However, smaller errors leaves the pedestal χ^2 essentially unchanged. Also the energy flow of the jet itself is a bit underestimated (figures 11.4(c), 11.5(c)). This again was not observed in the forward pion study, where RAPGAP had a tendency to overshoot the central peak.

CASCADE: The striking feature of the two CASCADE samples is again the apparently large sensitivity to the unintegrated gluon density. They give approximately the same values in the jet itself, where both samples predict a lower value of the transverse energy flow than is seen in the data. The pedestal however, which corresponds to the softer emissions, is very different.

Away from the jet, it is seen that Set 1 stays nicely on the data points apart from the dip at $1.5 < \eta < 2$, which in figure 11.4(b) is smeared into a general overestimate of the E_t -flow.

Looking at Set 2, it is seen that it is capable of describing features of the data that none of the other generators can. While it is still too low in the jet itself, it provides a good description of the pedestal (especially in figures 11.5(b) and 11.5(c)). Table 11.2 shows that all pedestal predictions are compatible with the data, even when disregarding the systematic error. The dip in the data at $1.5 < \eta < 2$ is also very well reproduced.

In the π^0 -plots in figure 11.7, the CASCADE description improved, looking at pions closer to the beam pipe. This behaviour is not as clearly observed with the forward jets. Quite to the contrary the lower half of table 11.2 argues that the CASCADE description of the data is better for low values of $\eta_{\text{forward jet}}$.

11.2 Jet-Profiles

Jet profiles are typically used as a cross-check that jets are correctly identified and reconstructed. The ϕ -profiles give an understanding of the p_t -compensation of the jet, and the η -profiles describe the jet relative to the rest of the average event topology.

The jet-profiles as they are defined here state that a ϕ -profile is simply the E_t -flow as a function of $\Delta\phi$ relative to the forward jet. Only particles within the η -slice, $|\Delta\eta| \leq 1$ are

counted to enhance the immediate features of the jet itself. Correspondingly, an η -profile is defined as the E_t -flow as a function of $\Delta\eta$ within a ϕ -slice, $|\Delta\phi| \leq 1$.

A study done by ZEUS [ZE99] using Cone jets showed a broadening of the forward jet close to the beam pipe as well as a contamination of the jet by the proton remnant. This was used to argue that forward jet pseudo rapidities over 2.6 should be disregarded. I have therefore divided the data into six bins of $\eta_{\text{forward jet}}$, to try to establish whether this is also the case in the data presented here.

The bins are shown in table 11.3.

Bin 1	$1.735 < \eta_{\text{forward jet}} < 2.30$
Bin 2	$2.30 < \eta_{\text{forward jet}} < 2.50$
Bin 3	$2.50 < \eta_{\text{forward jet}} < 2.60$
Bin 4	$2.60 < \eta_{\text{forward jet}} < 2.65$
Bin 5	$2.65 < \eta_{\text{forward jet}} < 2.72$
Bin 6	$2.72 < \eta_{\text{forward jet}} < 2.79$

Table 11.3: Bins of $\eta_{\text{forward jet}}$ for jet-profile study.

11.2.1 Detector Level Jet-Profiles

First, the p_t -compensation is considered by looking at the ϕ -profile of all selected forward jet events. No binning is performed in $\eta_{\text{forward jet}}$ at this point. Looking at figure 11.8 where the detector level jet-profiles are shown, it is observed that ARIADNE tends to describe the p_t -compensation a little better than RAPGAP DIR. This is based upon the observation that the data points rise a bit as the $\Delta\phi$ -values go towards $\pm\pi$, indicating that a measurable fraction of the p_t -compensation takes place within the $\Delta\eta$ -slice of $|\Delta\eta| \leq 1$. This behaviour is not at all described by RAPGAP DIR, while ARIADNE does show a small rise at the edges.

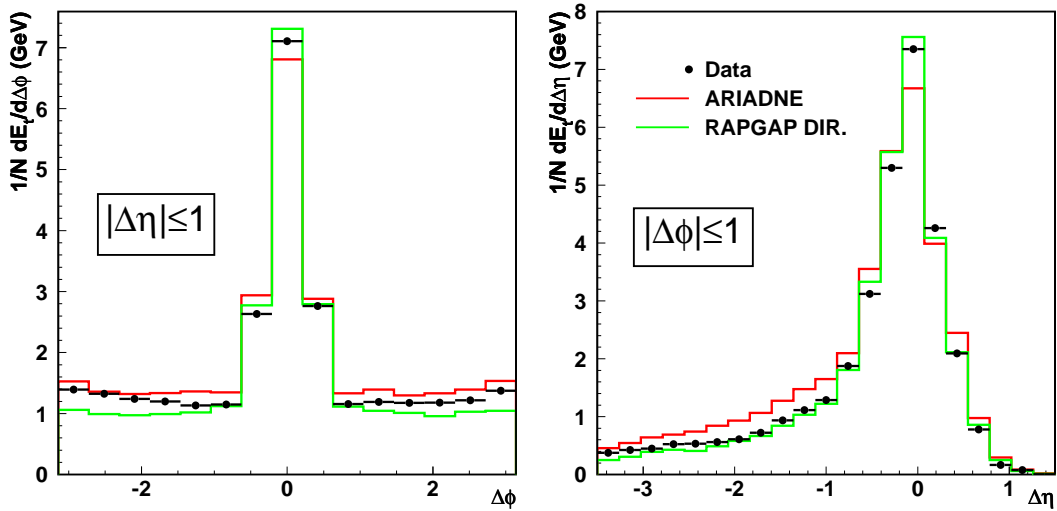


Figure 11.8: Detector level jet-profiles. Data (points) is compared to ARIADNE (red) and RAPGAP DIR. (green).

Turning to the η -profile, however, the picture seems to be that the softer emissions away from the jet are described a lot better by RAPGAP DIR than by ARIADNE.

Then the broadening is considered. Figure 11.9 shows the jet-profiles for the six $\eta_{\text{forward jet}}$ -bins. The ϕ -profiles at this point show no indication of the behaviour observed by ZEUS. Looking at the η -profiles, it is seen that the tail in the central part of the detector becomes larger, whereas the jet itself remains essentially unchanged.

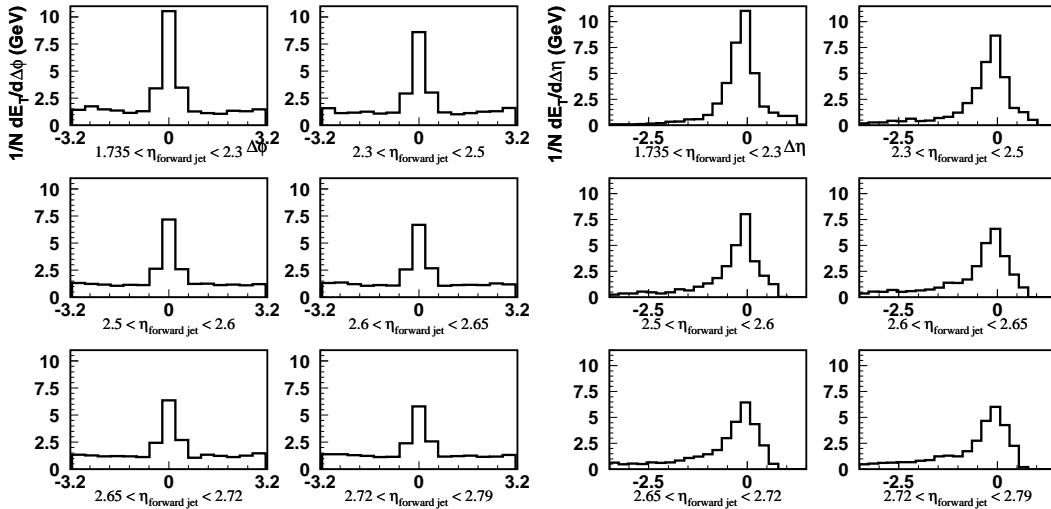


Figure 11.9: Jet-profiles in bins of $\eta_{\text{forward jet}}$.

There is at this point no indication that the jet should be contaminated by the proton remnant or broadened as suggested by ZEUS, as that would appear in the ϕ -profiles.

11.2.2 Corrections

To perform a detailed comparison of the data to the different Monte Carlo generators, the jet-profiles need to be corrected to non-radiative hadron level. The bin-by-bin procedure is employed again, using the same ARIADNE samples.

The correction factors obtained for the correction of figure 11.8 to non-radiative hadron level are shown in figure 11.10. To understand the apparent structure of these correction factors the detector level distributions have been plotted together with the non-radiative hadron level distributions in figure 11.11. As can be seen, there is a smearing, leading to transverse energy from the jets to be reconstructed in the pedestal. The correction for this effect is precisely what is depicted in figure 11.10.

11.2.3 Treatment of Systematics

The same contributions to the systematic error have been considered as in 10.3, and 11.1.3. Once again, the model dependence gives sizable contributions, just as the energy scale is also a major contributor.

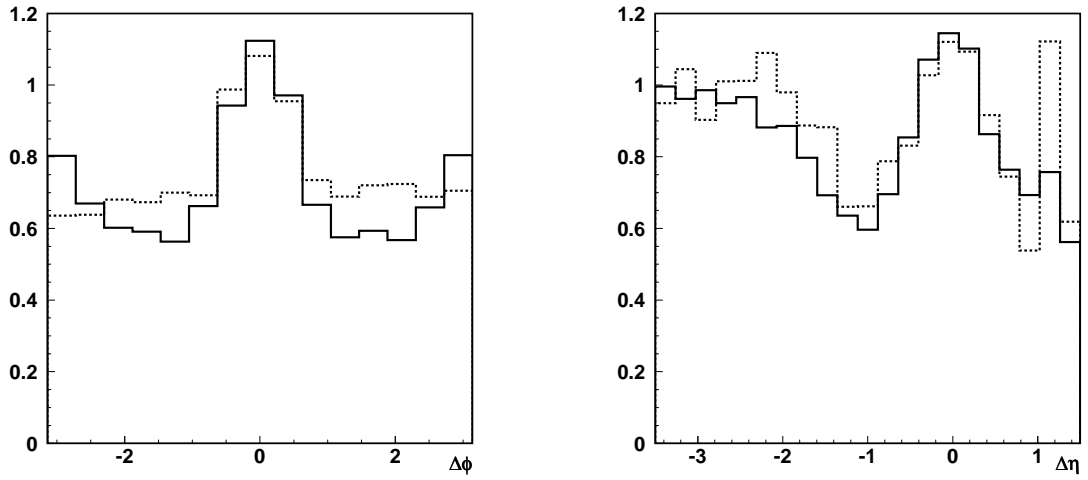
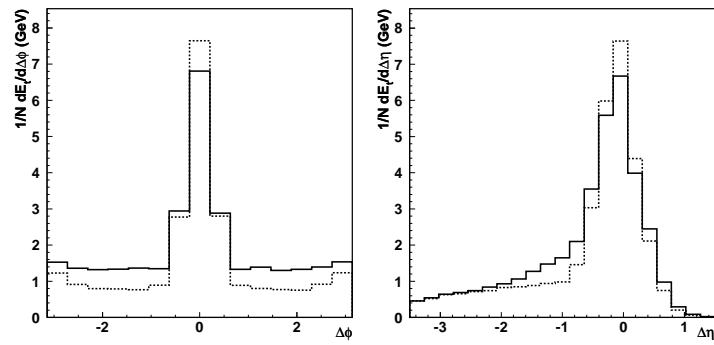
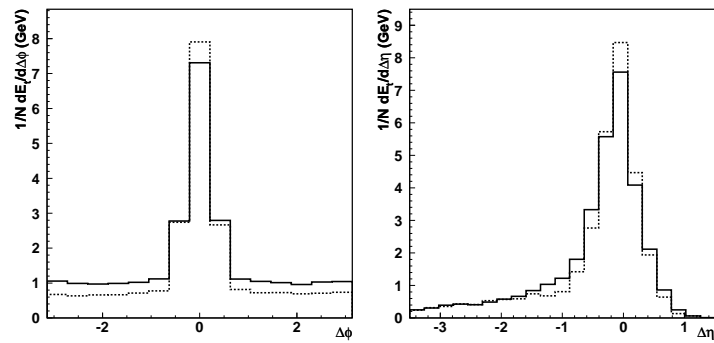


Figure 11.10: Correction factors for the jet-profiles. The correction factors from ARIADNE (solid line) and RAPGAP DIR (dotted line) are shown.



(a) ARIADNE



(b) RAPGAP DIR

Figure 11.11: Detector vs. non-radiative hadron level. The solid lines are reconstructed detector level, and the dotted lines are non-radiative hadron level.

11.2.4 Comparison to Monte Carlo

The corrected jet-profiles are shown in figure 11.12. As there was very little difference between the different versions of RAPGAP and CASCADE, only one of each has been included.

Consider the ϕ -profile first. The particles are all emitted in the forward direction, as they must be within $|\Delta\eta| \leq 1$ to be included. It seems that there is little difference in the way these forward emissions are handled, although there is a slight tendency of ARIADNE to describe the p_t -compensation best.

Turning to the η -profile, where the entire η -range of the detector is taken into account, there is a clear tendency of ARIADNE to overshoot the data in the tail. This is in agreement with what was observed in 11.1.4, although it has been greatly enhanced by the $|\Delta\phi| \leq 1$ -cut.

For completeness the jet-profiles have also been corrected to non-radiative hadron level in the six bins of $\eta_{\text{forward jet}}$ defined in table 11.3. This is in contrast to the measurement in [ZE99], where only detector level distributions were considered. The corrected distributions are shown in figure 11.13. Note how the forward jet remains clearly defined also in these plots. There are no indications of contamination by the proton remnant.

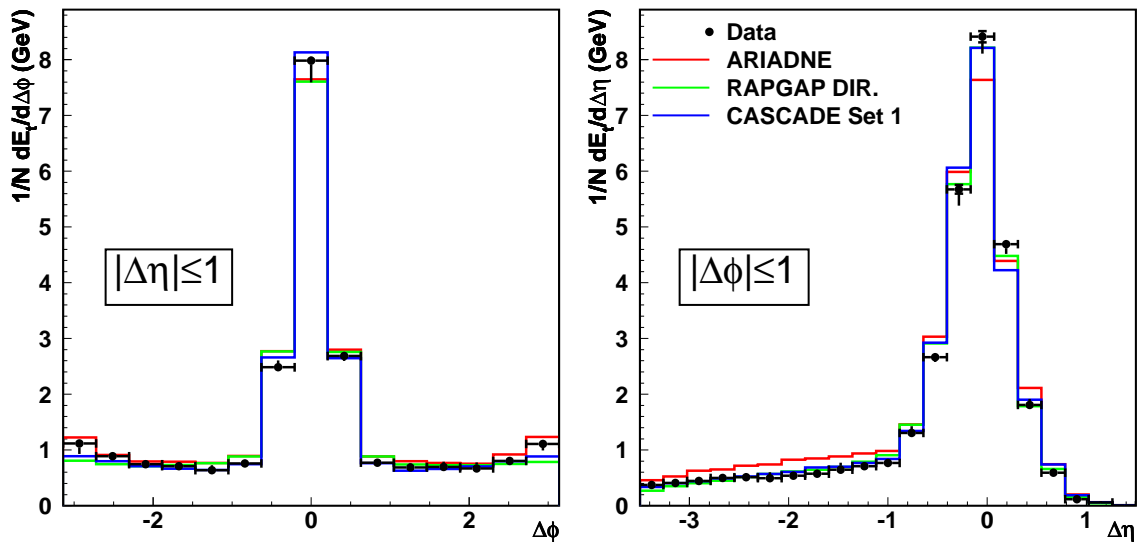
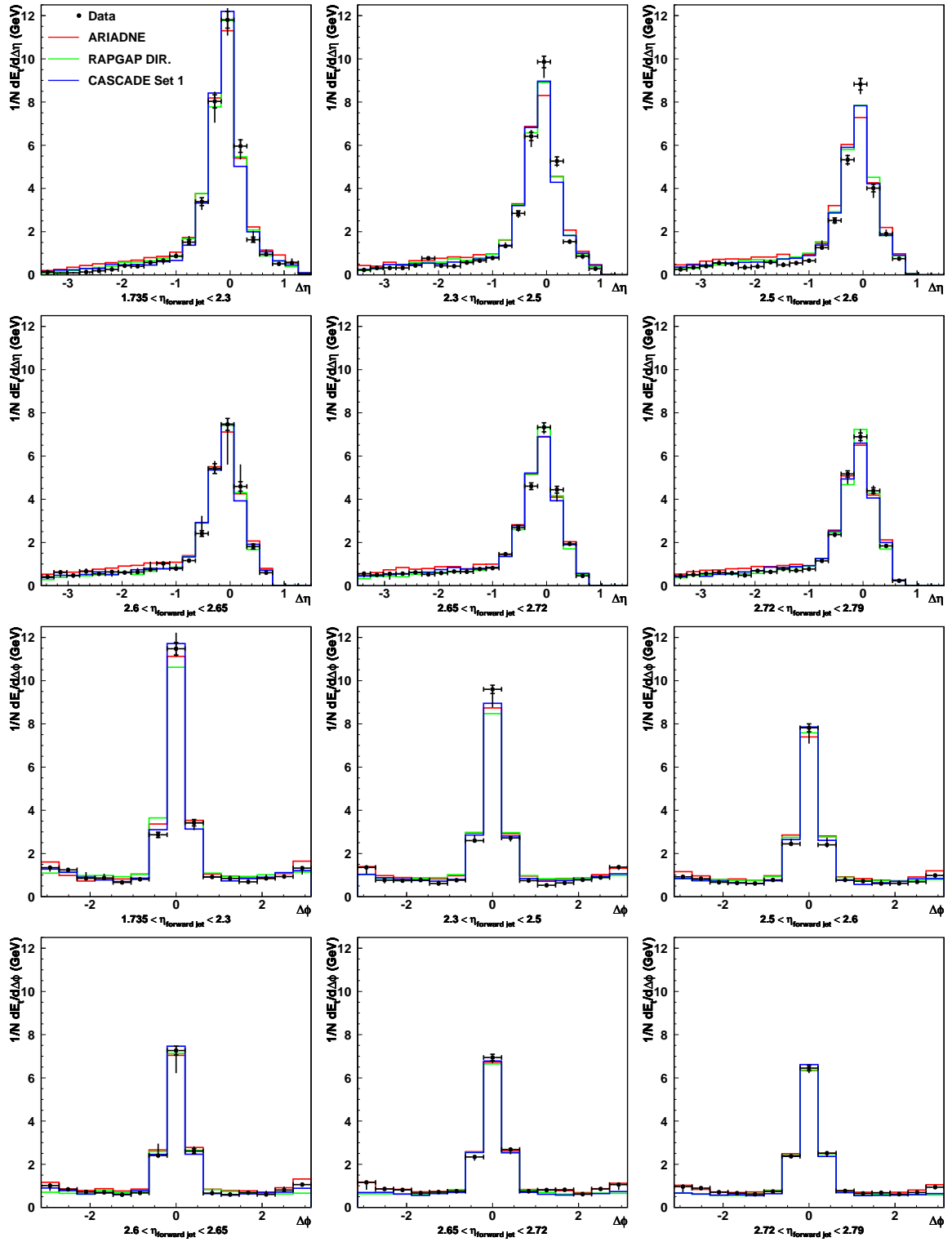


Figure 11.12: *The corrected jet-profiles. The data are compared to ARIADNE, RAPGAP DIR and CASCADE, using two different sets of unintegrated gluon densities.*

Figure 11.13: Corrected jet-profiles in bins of $\eta_{\text{forward jet}}$.

11.3 The p_t -Spectrum

The treatment of soft emissions seems to be a central parameter in discerning between the different Monte Carlo models. A p_t -spectrum was therefore made of the particles in all the selected forward jet events in an attempt to see, if there was a significant difference between the models.

11.3.1 Detector Level Spectrum

The detector level p_t -spectra of FSCOMB objects are shown in figure 11.14. The spectra have been divided into bins of $\eta_{\text{forward jet}}$ as originally defined in table 11.1.

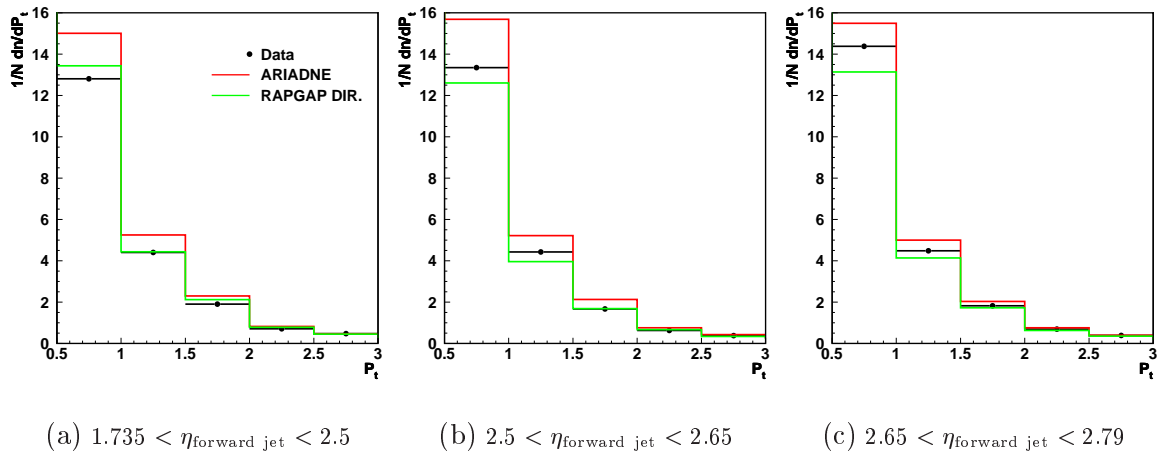


Figure 11.14: Detector level p_t -spectra of forward jet events. The plots are organised with ascending $\eta_{\text{forward jet}}$ from left to right in accordance with table 11.1.

The spectrum stops at $p_t=3$ GeV, because the statistical error increases dramatically as the average occupancy in each bin decreases below 1. Also, a noise cut is made at $p_t=0.5$ GeV.

What can be seen in these plots is that both models tend to give an adequate qualitative description, while RAPGAP DIR seems to give the better description for the lowest values of $\eta_{\text{forward jet}}$.

11.3.2 Corrections

Figure 11.15 shows the correction factors calculated from ARIADNE over a large p_t -range of [0 GeV, 10 GeV]. $\eta_{\text{forward jet}}$ is in the range [1.735, 2.30]. It makes good sense to make a noise cut for $p_t < 0.5$ GeV, which has been done. Also, it can be readily seen that the description is best in the region $p_t \in [0.5 \text{ GeV}, 2 \text{ GeV}]$, while the statistical error rapidly deteriorates beyond this point.

The correction factors from the selected p_t -range are plotted in figure 11.16. It is worth noting that the two generators agree only to within 10-15% even in the first three bins. This means that the systematic error from model dependence becomes very large.

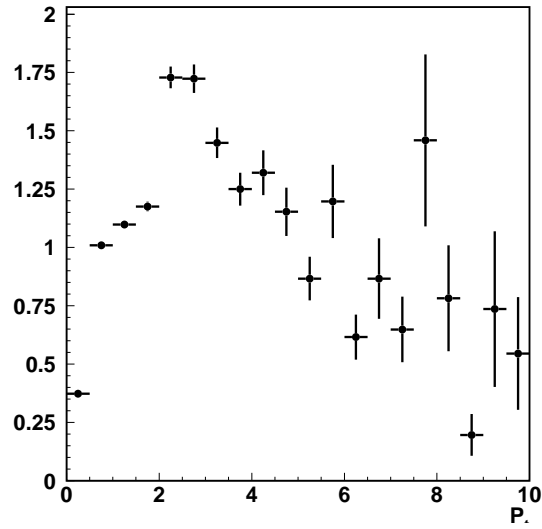
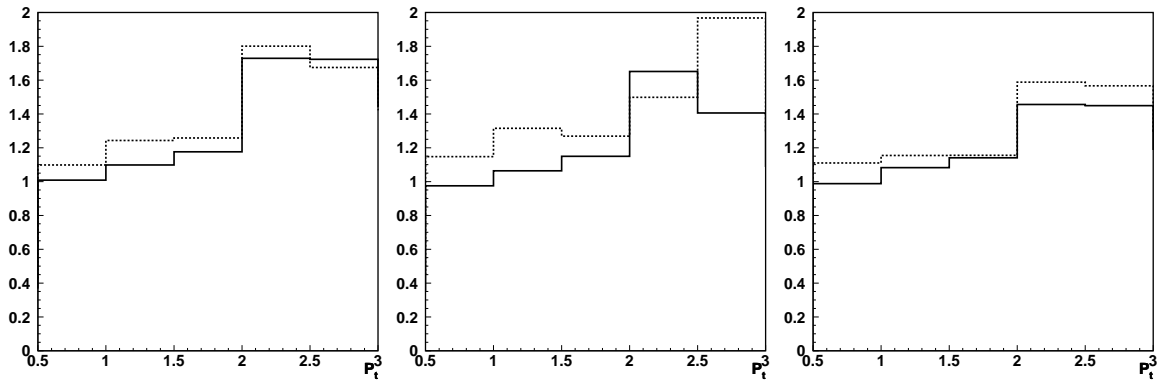


Figure 11.15: Correction factors in the full p_t -range.



(a) $1.735 < \eta_{\text{forward jet}} < 2.5$

(b) $2.5 < \eta_{\text{forward jet}} < 2.65$

(c) $2.65 < \eta_{\text{forward jet}} < 2.79$

Figure 11.16: Correction factors for the p_t -spectra. The correction factors from ARIADNE (solid line) and RAPGAP DIR (dotted line) are shown.

11.3.3 Systematics

Contributions to the systematic error have been investigated as in section 10.3 and 11.1.3. The model dependence has proved to be the dominant contribution by far. As discussed in the previous sections the error stemming from the comparison with RAPGAP DIR is of the order 10-15%, sometimes more. None of the other contributions exceed a few percent.

11.3.4 Results

The corrected spectra are shown in figure 11.17. As expected, the systematic errors are completely dominating the total error.

It turns out that there is practically no change in the p_t -spectrum as the result of the inclusion of a resolved photon component in RAPGAP. The two lines are practically on top of each other.

Due to the large systematic error, it is hard to draw conclusions, but the tendency seems to be that CASCADE provides a very good description of the p_t -spectrum, where both ARIADNE and RAPGAP have problems in the soft regions. As for the unintegrated gluon densities, it seems that Set 2 provides the best description for low forward jet pseudorapidities, whereas Set 1 is the best at high values of $\eta_{\text{forward jet}}$.

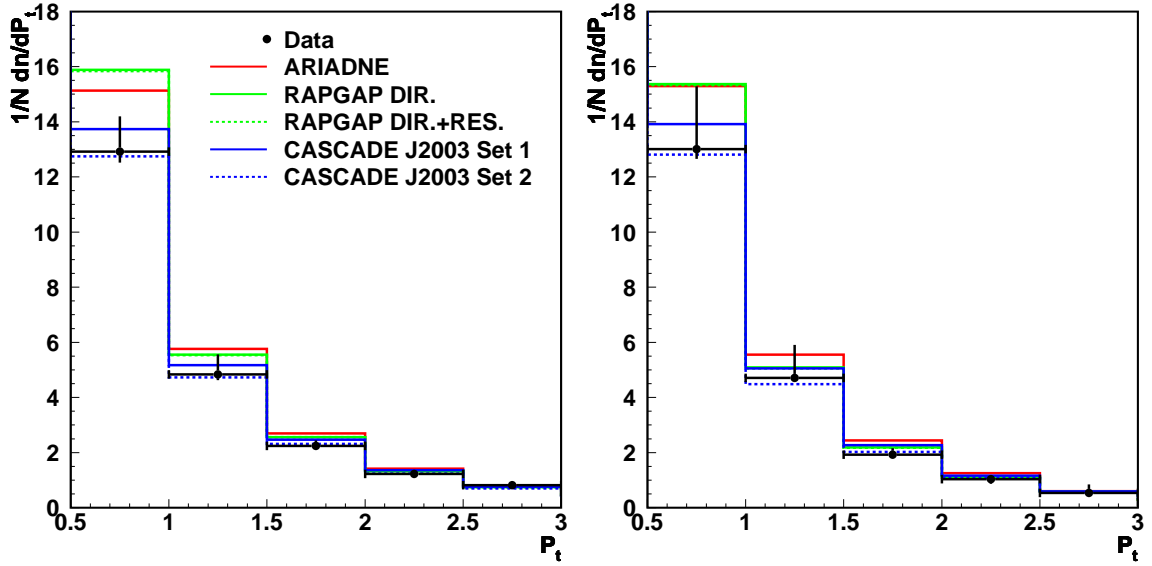
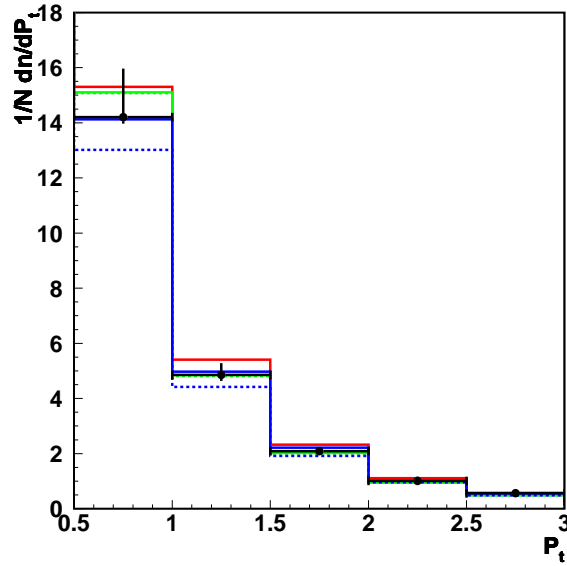
(a) $1.735 < \eta_{\text{forward jet}} < 2.5$ (b) $2.5 < \eta_{\text{forward jet}} < 2.65$ (c) $2.65 < \eta_{\text{forward jet}} < 2.79$

Figure 11.17: The corrected p_t -spectra. The data are compared to ARIADNE, RAPGAP DIR, RAPGAP DIR+RES and CASCADE, using two different sets of unintegrated gluon densities.

Chapter 12

Conclusions and Outlook

A measurement of the forward jet cross section has been presented as a function of Bjorken- x , the forward jet transverse momentum $P_{t,jet}$ and the fraction of the proton momentum carried by the jet x_{jet} . The measurement is based upon an integrated luminosity of 13.72 pb^{-1} collected by the H1 collaboration during 1997. Through a correction to hadron level, a comparison has been made to different QCD models through the corresponding Monte Carlo generators. The measurement agrees with previous analyses [Kar02]. Also event variables have been studied, focusing on transverse dynamics to make an attempt to discern between different models of QCD.

12.1 Observations

It is seen that normal DGLAP evolution embodied in RAPGAP DIR fails completely in describing the forward jet event cross section. Inclusion of a resolved photon component, however, improves the situation dramatically. The event variables show very little dependence on the resolved photon component. Here, DGLAP evolution gives a description that is compatible to the data. Especially the hard emissions in the jet itself is well described, while the softer emissions, as they are seen for example in the E_t -flow pedestals of figures 11.4 - 11.5 are less convincingly described.

Along with RAPGAP DIR+RES, the Colour Dipole Model embodied in ARIADNE provides a very good description of the forward jet cross section. However, in the measurements of the event variables, ARIADNE shows a clear tendency to overshoot the measured transverse energy flow. This is especially seen when considering the jet-profiles in terms of pseudorapidity. The ϕ -description of the jet-profiles is very good, however. Another note on ARIADNE is that it does not give a good description of the p_t -spectra.

The prediction of CASCADE, and consequently CCFM, turns out to be extremely sensitive to the non-singular terms in the gluon splitting function and the corresponding calculation of the unintegrated gluon density (section 5.2). The cross section shows a very strong difference between the two calculations used. Set 1 seems to overshoot the cross section quite consistently (apart from the lowest x_{bj} -bin). None of the two CASCADE samples reproduce the cross section in the softest bins, while agreement is better with the data for harder jets and larger values of x_{bj} . The event variables, however, all seem to be quite well described by CCFM.

Especially CASCADE Set 2, which includes the full gluon splitting function, does a good job. Specifically the soft emissions of the E_t -flow pedestals in figures 11.4 - 11.5, as well as the p_t -spectra in figure 11.17, are very well described.

12.2 What Was Learned

It has been demonstrated that CCFM is better suited than DGLAP in describing forward jet events, both with regards to the cross section and the event topology. Also it has been shown, how the “double DGLAP” approach of the resolved photon model brings the DGLAP prediction for the cross section in perfect agreement with the data, while having little effect on the event topology. This, however, is at the expense of introducing extra variables.

The forward jets in the selected events are well defined and well described by most models. There are no indications of contamination by the proton remnant as a function of pseudorapidity as described by ZEUS. It remains to be clarified, whether this difference is induced by the choice of jet algorithm, or if the ZEUS observation was simply a resolution effect in the calorimeters. The present analysis goes further than the ZEUS measurement by correcting the jet profiles to non-radiative hadron level and doing detailed comparison to Monte Carlo predictions.

No hard conclusions regarding parton dynamics can be drawn from the E_t -flow measurement or the p_t -spectra. There are indications that DGLAP evolution is not sufficient to describe soft emissions, even when including the resolved photon, but there is no basis for concluding that this should be interpreted as the onset of BFKL-like dynamics. So there is as yet no basis to *disregard* any model. It is interesting, though, that the CCFM prediction depending only on three parameters provides a highly competitive description of the event topology.

12.3 Outlook

A central problem of this analysis has been the very large systematic error induced by the model dependence of the detector corrections. As radiative corrections should not give deviations of this size between the models, this is probably a problem in the detector simulation. To try and solve this, a path could be chosen to perform the corrections in two steps. This would mean simulating flat distributions in all variables, and running them through fragmentation (JETSET) and the detector simulation to obtain separate correction factors for the detector effects and for the radiative corrections.

Other problems in this analysis were the high values for the background and the low acceptance, which were discussed in section 9.7. Recent studies done by the Lund group indicate that this situation may be improved by loosening the upper limit of the $\frac{p_t^2}{Q^2}$ -cut for the forward jet. However, nothing is final on this.

In the years 1998-2000, HERA collected a total integrated luminosity of around 100 pb^{-1} . Due to the increase in proton energy from 820 GeV to 920 GeV , lower regions in Bjorken- x have been made available. Analysis of this data would therefore mean not only an increase in statistics of the forward jet event sample, but also a probable increase in the ability to discern between the models at low- x_{bj} .

During the 1990's, DIS was the best testing ground for parton dynamics, and DGLAP as well as the possible transition into BFKL dynamics have been studied intensively. In 2007, the Large Hadron Collider (LHC) is expected to start operations at CERN, Geneva. When that happens, a whole new area of opportunities to see BFKL-like dynamics will arise. The first suggestion [MN87] for a BFKL signature at LHC was to study di-jet production at large rapidity separation. This, however, has been disfavoured by later studies [ADDF⁺01], showing that the BFKL parton dynamics convoluted with parton density functions would be nearly invisible. Other channels remain promising, though. These are associated mini-jet multiplicities in Higgs production [EOSW00] and $W + 2\text{jet}$ production [And02].

There is thus plenty of work to be done in QCD for the years to come.

Chapter 13

Acknowledgements

In the process of writing this thesis, many things would have been a great deal harder, had it not been for a great many people. First of all I wish to thank my supervisors. John Renner Hansen for always asking just the wrong questions in just the right way. Leif Jönsson for providing friendly and thorough advice at all stages of the project. Hannes Jung for always being ready and able to help with the details and make suggestions for things to investigate. Secondly I wish to thank the people of the Lund group for their friendliness and hospitality. Thank you for allowing me, to work with you. Specifically I wish to thank Martin & Albert for helping out with many practical details.

In the writing phase many people have contributed greatly. In that context I wish to thank Thomas Ziegler for his overwhelmingly thorough comments to the final drafts. Thanks to Jakob “Brombø” Nielsen for advice and comments on the theory chapters. Thanks to Nick Weppenaar for undertaking the Herculean, task of; correcting my - English grammar. Thanks to Peter Zeiler Skands and Torbjörn Sjöstrand for friendly advice (and coffee).

Many other persons have contributed in easing this task in the daily life. Most notably of course my love, Louise, for understanding that I could not always come home at 5pm. Also I wish to thank the other students in the group. It was nice hangin’ with you. Thanks also go out to friends and family, for not writing me off completely for doing crazy and incomprehensible stuff.

I also wish to thank the HEP group at the Niels Bohr Institute. I have only received the best of treatment while studying here. Every door has always been open, and every question has always been met with interest.

Finally I wish to thank the Lørup Fund for financial support.

Bibliography

- [AC99] H. Abramowicz and A. Caldwell, *HERA collider physics*, Rev. Mod. Phys. **71**, 1275–1410 (1999), hep-ex/9903037.
- [ADDF⁺01] J. R. Andersen, V. Del Duca, S. Frixione, C. R. Schmidt and W. J. Stirling, *Mueller-Navelet jets at hadron colliders*, JHEP **02**, 007 (2001), hep-ph/0101180.
- [Na] (ALEPH Collaboration), *A study of the string effect in $Z \rightarrow 3\text{jets}$* , Prepared for International Europhysics Conference on High-energy Physics (HEP 95), Brussels, Belgium, 27 Jul - 2 Aug 1995.
- [Nb] M. Mermikides (ALEPH Collaboration), *THE ALEPH DETECTOR*, IN *CORFU 1985, PROCEEDINGS, ELEMENTARY PARTICLE PHYSICS* 191-206.
- [And97] B. Andersson, *The Lund model*, Cambridge Monogr. Part. Phys. Nucl. Phys. Cosmol. **7**, 1–471 (1997).
- [And02] J. R. Andersen, *Forward jets and BFKL at hadron colliders*, Acta Phys. Polon. **B33**, 3001–3006 (2002), hep-ph/0207019.
- [AP77] G. Altarelli and G. Parisi, *ASYMPTOTIC FREEDOM IN PARTON LANGUAGE*, Nucl. Phys. **B126**, 298 (1977).
- [AP99] J. Ambjørn and J. L. Petersen, *Quantum Field Theory*, University of Copenhagen, The Niels Bohr Institute, 1999.
- [B⁺] J. Bromley et al., *HZTOOL: A package for Monte Carlo-data comparison at HERA (version 1.0)*, Prepared for Workshop on Future Physics at HERA (Preceded by meetings 25-26 Sep 1995 and 7-9 Feb 1996 at DESY), Hamburg, Germany, 30-31 May 1996.
- [B⁺89] J. Burger et al., *The Central jet chamber of the H1 experiment*, Nucl. Instrum. Meth. **A279**, 217–222 (1989).
- [BdRL92] J. Bartels, A. de Roeck and M. Loewe, *Measurement of hot spots inside the proton at HERA and LEP/LHC*, Z. Phys. **C54**, 635–642 (1992).
- [BJ] W. E. Burcham and M. Jobes, *Nuclear and particle physics*, Harlow, UK: Longman (1995) 752 p.

- [BL78] I. I. Balitsky and L. N. Lipatov, *THE POMERANCHUK SINGULARITY IN QUANTUM CHROMODYNAMICS*, Sov. J. Nucl. Phys. **28**, 822–829 (1978).
- [BMSS98] G. Bottazzi, G. Marchesini, G. P. Salam and M. Scorletti, *Small-x one-particle-inclusive quantities in the CCFM approach*, JHEP **12**, 011 (1998), hep-ph/9810546.
- [CCH91] S. Catani, M. Ciafaloni and F. Hautmann, *High-energy factorization and small x heavy flavor production*, Nucl. Phys. **B366**, 135–188 (1991).
- [CDSW93] S. Catani, Y. L. Dokshitzer, M. H. Seymour and B. R. Webber, *Longitudinally invariant $K(t)$ clustering algorithms for hadron hadron collisions*, Nucl. Phys. **B406**, 187–224 (1993).
- [CES92] J.-g. Chay, S. D. Ellis and W. J. Stirling, *Azimuthal asymmetry in lepton - photon scattering at high- energies*, Phys. Rev. **D45**, 46–54 (1992).
- [CFM90a] S. Catani, F. Fiorani and G. Marchesini, *QCD COHERENCE IN INITIAL STATE RADIATION*, Phys. Lett. **B234**, 339 (1990).
- [CFM90b] S. Catani, F. Fiorani and G. Marchesini, *SMALL x BEHAVIOR OF INITIAL STATE RADIATION IN PERTURBATIVE QCD*, Nucl. Phys. **B336**, 18 (1990).
- [Cia88] M. Ciafaloni, *COHERENCE EFFECTS IN INITIAL JETS AT SMALL Q^{*2}/s* , Nucl. Phys. **B296**, 49 (1988).
- [Cow] G. Cowan, *Statistical data analysis*, Oxford, UK: Clarendon (1998) 197 p.
- [Dav01] M. Davidsson, *Jet Production and Parton Dynamics in Deep Inelastic Scattering*, PhD thesis, Lund University, 2001.
- [DES] DESY Website, <http://www.desy.de/>.
- [Dok77] Y. L. Dokshitzer, *CALCULATION OF THE STRUCTURE FUNCTIONS FOR DEEP INELASTIC SCATTERING AND $E^+ E^-$ ANNIHILATION BY PERTURBATION THEORY IN QUANTUM CHROMODYNAMICS. (IN RUSSIAN)*, Sov. Phys. JETP **46**, 641–653 (1977).
- [Ege] U. Egede, *The search for a Standard Model Higgs at the LHC and electron identification using transition radiation in the ATLAS tracker*, CERN-THESIS-98-001.
- [EOSW00] C. Ewerz, L. H. Orr, W. J. Stirling and B. R. Webber, *BFKL dynamics at hadron colliders*, J. Phys. **G26**, 696–701 (2000), hep-ph/9912469.
- [ES93] S. D. Ellis and D. E. Soper, *Successive combination jet algorithm for hadron collisions*, Phys. Rev. **D48**, 3160–3166 (1993), hep-ph/9305266.
- [ESW96] R. K. Ellis, W. J. Stirling and B. R. Webber, *QCD and collider physics*, Cambridge Monogr. Part. Phys. Nucl. Phys. Cosmol. **8**, 1–435 (1996).

- [Fey] R. P. Feynman, *Partons*, Prepared for Symposium on the Past Decade in Particle Theory, Austin, Tex., 14-17 Apr 1970.
- [Fey72] R. P. Feynman, *Photon - Hadron Interactions*, Frontiers in Physics, W. A. Benjamin, Inc. , 1-282 (1972).
- [FSV98] J. R. Forshaw and A. Sabio Vera, *QCD coherence and jet rates in small x deep inelastic scattering*, Phys. Lett. **B440**, 141-150 (1998), hep-ph/9806394.
- [GL72] V. N. Gribov and L. N. Lipatov, *e+ e- pair annihilation and deep inelastic e p scattering in perturbation theory*, Yad. Fiz. **15**, 1218-1237 (1972).
- [GM64] M. Gell-Mann, *A Schematic model of baryons and mesons*, Phys. Lett. **8**, 214-215 (1964).
- [GP74] H. Georgi and H. D. Politzer, *Electroproduction scaling in an asymptotically free theory of strong interactions*, Phys. Rev. **D9**, 416-420 (1974).
- [GP88] G. Gustafson and U. Pettersson, *DIPOLE FORMULATION OF QCD CASCADES*, Nucl. Phys. **B306**, 746 (1988).
- [Gus86] G. Gustafson, *DUAL DESCRIPTION OF A CONFINED COLOR FIELD*, Phys. Lett. **B175**, 453 (1986).
- [GW74] D. J. Gross and F. Wilczek, *ASYMPTOTICALLY FREE GAUGE THEORIES. 2*, Phys. Rev. **D9**, 980-993 (1974).
- [H⁺] E. Hartouni et al., *HERA-B: An experiment to study CP violation in the B system using an internal target at the HERA proton ring. Design report*, DESY-PRC-95-01.
- [H1] (H1 Collaboration), *Guide to Simulation program H1SIM*, The H1SIM guide resides at DESY in the CVS repository under /h1sim/manual.
- [H194] I. Abt et al. (H1 Collaboration), *Scaling violations of the proton structure function f2 at small x*, Phys. Lett. **B321**, 161-167 (1994).
- [H196] J. Ban et al. (H1 BEMC Group Collaboration), *The H1 backward calorimeter BEMC and its inclusive electron trigger*, Nucl. Instrum. Meth. **A372**, 399-414 (1996).
- [H197a] I. Abt et al. (H1 Collaboration), *The H1 detector at HERA*, Nucl. Instrum. Meth. **A386**, 310-347 (1997).
- [H197b] I. Abt et al. (H1 Collaboration), *The Tracking, calorimeter and muon detectors of the H1 experiment at HERA*, Nucl. Instrum. Meth. **A386**, 348-396 (1997).
- [H100] C. Adloff et al. (H1 Collaboration), *Measurements of transverse energy flow in deep inelastic- scattering at HERA*, Eur. Phys. J. **C12**, 595-607 (2000), hep-ex/9907027.
- [H103a] L. Goerlich (H1 Collaboration), *Forward π^0 production in DIS at HERA*, (2003).

- [H103b] M. Karlsson, H. Jung and L. Jonsson (H1 Collaboration), *Forward Jet Production at HERA*, (2003).
- [H1Cal93] B. Andrieu et al. (H1 Calorimeter Group Collaboration), *The H1 liquid argon calorimeter system*, Nucl. Instrum. Meth. **A336**, 460–498 (1993).
- [H1L] H1 Level 4 Filter Home Page, <http://www-h1.desy.de/ittrigger/L4Farm/>.
- [H1SG96] T. Nicholls et al. (H1 SPACAL Group Collaboration), *Performance of an electromagnetic lead / scintillating fiber calorimeter for the H1 detector*, Nucl. Instrum. Meth. **A374**, 149–156 (1996).
- [HJ03] M. Hansson and H. Jung, *Status of CCFM: Un-integrated gluon densities*, (2003), hep-ph/0309009.
- [HL00] H. Henschel and R. Lahmann, *The backward silicon tracker of the H1 experiment at HERA*, Nucl. Instrum. Meth. **A453**, 93–97 (2000).
- [HM] F. Halzen and A. D. Martin, *QUARKS AND LEPTONS: AN INTRODUCTORY COURSE IN MODERN PARTICLE PHYSICS*, New York, Usa: Wiley (1984) 396p.
- [JA81] W. Bartel et al. (JADE Collaboration), *EXPERIMENTAL STUDY OF JETS IN ELECTRON-POSITRON ANNIHILATION*, Phys. Lett. **B101**, 129 (1981).
- [JA83] W. Bartel et al. (JADE Collaboration), *PARTICLE DISTRIBUTION IN THREE JET EVENTS PRODUCED BY e^+e^- ANNIHILATION*, Z. Phys. **C21**, 37 (1983).
- [Jac94] C. Jacobsson, *Jet Azimuthal Angle Asymmetries in Deep Inelastic Scattering as a test of QCD*, PhD thesis, Lund University, 1994.
- [JJK98] H. Jung, L. Jonsson and H. Kuster, *Resolved photon processes in DIS and small x dynamics*, (1998), hep-ph/9805396.
- [JS01] H. Jung and G. P. Salam, *Hadronic final state predictions from CCFM: The hadron-level Monte Carlo generator CASCADE*, Eur. Phys. J. **C19**, 351–360 (2001), hep-ph/0012143.
- [Jun95] H. Jung, *Hard diffractive scattering in high-energy $e p$ collisions and the Monte Carlo generation RAPGAP*, Comp. Phys. Commun. **86**, 147–161 (1995).
- [Jun02a] H. Jung, *The CCFM Monte Carlo generator CASCADE*, Comput. Phys. Commun. **143**, 100–111 (2002), hep-ph/0109102.
- [Jun02b] H. Jung, *Unintegrated parton densities applied to heavy quark production in the CCFM approach*, J. Phys. **G28**, 971–982 (2002), hep-ph/0109146.
- [K⁺98] N. Keller et al., *Status of the BDC Analysis*, H1 internal note 550, 1998.
- [Kar02] M. Karlsson, *A study of Parton Dynamics from Deep Inelastic Scattering Events Containing a Jet in the Forward Direction*, PhD thesis, Lund University, 2002.

- [KLF76] E. A. Kuraev, L. N. Lipatov and V. S. Fadin, *MULTI - REGGEON PROCESSES IN THE YANG-MILLS THEORY*, Sov. Phys. JETP **44**, 443–450 (1976).
- [KLF77] E. A. Kuraev, L. N. Lipatov and V. S. Fadin, *THE POMERANCHUK SINGULARITY IN NONABELIAN GAUGE THEORIES*, Sov. Phys. JETP **45**, 199–204 (1977).
- [KMS95] J. Kwiecinski, A. D. Martin and P. J. Sutton, *The gluon distribution at small x obtained from a unified evolution equation*, Phys. Rev. **D52**, 1445–1458 (1995), hep-ph/9503266.
- [Kup98] A. Kupco, *Cluster hadronization in HERWIG 5.9*, (1998), hep-ph/9906412.
- [Leo] W. R. Leo, *TECHNIQUES FOR NUCLEAR AND PARTICLE PHYSICS EXPERIMENTS: A HOW TO APPROACH*, Berlin, Germany: Springer (1987) 368 p.
- [Lip75] L. N. Lipatov, *The parton model and perturbation theory*, Sov. J. Nucl. Phys. **20**, 94–102 (1975).
- [Lob97] E. M. Lobodzinska, *Measurement of the forward jet cross-section in the low-x(B) region at HERA as a signature of BFKL dynamics*, PhD thesis (1997).
- [Lon92] L. Lonnblad, *ARIADNE version 4: A Program for simulation of QCD cascades implementing the color dipole model*, Comput. Phys. Commun. **71**, 15–31 (1992).
- [Lon99] L. Lonnblad, *The colour-dipole model and the ARIADNE program at high Q**2*, (1999), hep-ph/9908368.
- [Mar95] G. Marchesini, *QCD coherence in the structure function and associated distributions at small x*, Nucl. Phys. **B445**, 49–80 (1995), hep-ph/9412327.
- [Mil97] R. G. Milner, *The HERMES experiment*, Nucl. Phys. **A622**, 16c–30c (1997).
- [MN87] A. H. Mueller and H. Navelet, *AN INCLUSIVE MINIJET CROSS-SECTION AND THE BARE POMERON IN QCD*, Nucl. Phys. **B282**, 727 (1987).
- [Mue91a] A. Mueller, *JETS AT LEP AND HERA*, J. Phys. G **17**, 1443 (1991).
- [Mue91b] A. H. Mueller, *Parton distributions at very small x values*, Nucl. Phys. Proc. Suppl. **18C**, 125–132 (1991).
- [MW91] G. Marchesini and B. R. Webber, *Simulation of QCD initial state radiation at small x*, Nucl. Phys. **B349**, 617–634 (1991).
- [MW92] G. Marchesini and B. R. Webber, *Final states in heavy quark lepton production at small x*, Nucl. Phys. **B386**, 215–235 (1992).
- [P⁺00] D. Pitzl et al., *The H1 silicon vertex detector*, Nucl. Instrum. Meth. **A454**, 334–349 (2000), hep-ex/0002044.

- [PDG98] C. Caso et al. (Particle Data Group Collaboration), *Review of particle physics*, Eur. Phys. J. **C3**, 1–794 (1998).
- [Pet94] J. Petersen, *Elementarpartikelfysik*, NBI-tryk (1994), Lecture notes 3. rev. edition.
- [PS] M. E. Peskin and D. V. Schroeder, *An Introduction to quantum field theory*, Reading, USA: Addison-Wesley (1995) 842 p.
- [Sal99] G. P. Salam, *Soft emissions and the equivalence of BFKL and CCFM final states*, JHEP **03**, 009 (1999), hep-ph/9902324.
- [SB87] T. Sjostrand and M. Bengtsson, *THE LUND MONTE CARLO FOR JET FRAGMENTATION AND $e+e-$ PHYSICS: JETSET VERSION 6.3: AN UPDATE*, Comput. Phys. Commun. **43**, 367 (1987).
- [Sch96] B. Schwab, *Das Rückwärtsdriftkammersystem des H1-Experiments*, PhD thesis, Ruprech - Karls Universität, Heidelberg, 1996.
- [Sjo86] T. Sjostrand, *THE LUND MONTE CARLO FOR JET FRAGMENTATION AND $e+e-$ PHYSICS: JETSET VERSION 6.2*, Comput. Phys. Commun. **39**, 347–407 (1986).
- [Sjo94] T. Sjostrand, *High-energy physics event generation with PYTHIA 5.7 and JETSET 7.4*, Comput. Phys. Commun. **82**, 74–90 (1994).
- [Spi96] S. Spielmann, *The fast triggering electronics of the lead/scintillating-fibre SpaCal calorimeter of the H1 experiment at HERA: installation, CERN beam test results and first results at HERA*, PhD thesis, Ecole Polytechnique, 1996.
- [SS96] G. A. Schuler and T. Sjostrand, *Parton Distributions of the Virtual Photon*, Phys. Lett. **B376**, 193–200 (1996), hep-ph/9601282.
- [Tan92] W.-K. Tang, *The Structure function $\nu W(2)$ of hot spots at HERA*, Phys. Lett. **B278**, 363–366 (1992).
- [Web98] B. R. Webber, *Jet rates in deep inelastic scattering at small x*, Phys. Lett. **B444**, 81–85 (1998), hep-ph/9810286.
- [Wob00] M. Wobisch, *Measurement and QCD Analysis of Jet Cross Sections in Deep-Inelastic Positron-Proton Collisions at $\sqrt{s} = 300$ GeV*, (2000).
- [ZE] G. Wolf et al. (ZEUS Collaboration), *THE ZEUS DETECTOR: TECHNICAL PROPOSAL*, DESY-HERA-ZEUS-1.
- [ZE99] J. Breitweg et al. (ZEUS Collaboration), *Forward jet production in deep inelastic scattering at HERA*, Eur. Phys. J. **C6**, 239–252 (1999), hep-ex/9805016.
- [Zwe] G. Zweig, *AN $SU(3)$ MODEL FOR STRONG INTERACTION SYMMETRY AND ITS BREAKING. 2*, CERN-TH-412.

Appendix A

Some Notes on Representations and Structure Coefficients

In chapter 2, references are made to the *fundamental* and the *adjoint* representations of the Lie algebra of $SU(3)$. To understand what these representations are, it is instructive to consider elements of the theory of compact, simple Lie-groups.

I will here assume the reader to be familiar with the concepts of groups and compactness. The presentation follows that given in [Pet94], to which I refer for omitted proofs.

A.1 Fundamental Concepts

A Lie group is a topological group that can be equipped with a set of local coordinates after which differentiation can be performed. If the group considered as a topological space is compact, we refer to the group as a *compact Lie group*.

The archtypical example of a compact Lie group is the unitary group in one dimension:

$$\mathcal{U}(1) = \{e^{i\chi} | \chi \in \mathbb{R}\} \tag{A.1}$$

Its elements can be mapped to the unit circle, which is compact.

A.2 Lie Algebras

Considering a compact Lie group \mathcal{U} of dimension d , we may write the group elements in the area around the unit element $\mathbf{1}$ as:

$$\mathcal{U}(\vec{\epsilon}) = \mathbf{1} + i\vec{\epsilon} \cdot \vec{\mathcal{T}} \tag{A.2}$$

where $\vec{\epsilon} = (\epsilon_1, \dots, \epsilon_d)$ is an infinitesimal vector of dimension d , and where $\vec{\mathcal{T}} = (\mathcal{T}_1, \dots, \mathcal{T}_d)$ are the d so-called *generators of the Lie algebra*.

The Lie algebra is the set of all linear combinations of the \mathcal{T}_i 's. It is consequently the *tangent space of \mathcal{U} at $\mathbf{1}$* , and $\{\mathcal{T}_i\}$ is the basis of the Lie algebra.

By multiplying elements of the form (A.2), it may be shown, that

$$\exp\{i\vec{\theta} \cdot \vec{\mathcal{T}}\} \in \mathcal{U} \quad (\text{A.3})$$

also for the case when $\vec{\theta}$ is a finite vector.

Now consider two group elements in the neighbourhood of $\mathbf{1}$:

$$\mathcal{U}_1 = e^{i\epsilon\mathcal{T}} \quad \mathcal{U}_2 = e^{i\mu\mathcal{S}} \quad (\text{A.4})$$

where ϵ, μ are real and infinitesimal, and \mathcal{T}, \mathcal{S} are elements of the Lie algebra. We then know that

$$\mathcal{U}_1^{-1}\mathcal{U}_2^{-1}\mathcal{U}_1\mathcal{U}_2 \in \mathcal{U} \quad (\text{A.5})$$

To first order, this expression is just $\mathbf{1}$. To second order, however, we see that the expression evaluates to

$$\mathbf{1} + it[\mathcal{T}, \mathcal{S}] \quad (\text{A.6})$$

where t depends on ϵ, μ .

This shows us that if \mathcal{T} and \mathcal{S} are elements of the Lie algebra, then also $i[\mathcal{T}, \mathcal{S}]$ is in the Lie algebra. We may thus write:

$$[\mathcal{T}_i, \mathcal{S}_j] = iC_{ij}^k \mathcal{T}_k \quad (\text{A.7})$$

where summation over k is implied.

The set $\{C_{ij}^k\}$ is denoted the set of *structure coefficients* of the algebra. They are clearly antisymmetric in i, j , and the \mathcal{T}_k may be chosen so that the structure coefficients become antisymmetric in all indices. In this case, we write:

$$[\mathcal{T}_i, \mathcal{S}_j] = if_{ijk} \mathcal{T}_k \quad (\text{A.8})$$

For unitary matrices, the generators will be hermitean, and the f_{ijk} real.

A *matrix representation* of the Lie algebra is a set of d matrices \mathbf{T}_i that fulfil the relation

$$[\mathbf{T}_i, \mathbf{S}_j] = if_{ijk} \mathbf{T}_k \quad (\text{A.9})$$

These in turn generate a matrix representation of the group elements according to equation (A.3).

A.3 Representations of $SU(N)$

The group $SU(N)$ is the group of unitary $N \times N$ -matrices with determinant 1. These matrices themselves form a representation of $SU(N)$. This representation is known as the *fundamental representation*.

How do the generators look in this representation?

If we consider an $N \times N$ matrix \mathbf{U} in the neighbourhood of $\mathbf{1}$, we may write it

$$\mathbf{U} = \mathbf{1} + i\epsilon\mathbf{T} \quad (\text{A.10})$$

where \mathbf{T} is the hermitean matrix generator, and ϵ is infinitesimal. The determinant of \mathbf{U} is now

$$\det(\mathbf{1} + i\epsilon\mathbf{T}) = 1 + i\epsilon \sum_i T_{ii} + \mathcal{O}(\epsilon^2) \quad (\text{A.11})$$

from which it is seen that the generators of the fundamental representation of $SU(N)$ are traceless.

We can now restrict the generators by the following consideration. The general $N \times N$ matrix has $2N^2$ real parameters. A Hermitean matrix has a real diagonal, and hermiticity requires that it has only $\frac{1}{2} \times 2 \times (N^2 - N) + N = N^2$ real parameters. Imposing finally the requirement of a vanishing trace, it is seen that $N^2 - 1$ free parameters remain.

If the \mathbf{T} -matrices have $N^2 - 1$ free parameters, this means that there are $N^2 - 1$ generators of the Lie algebra of $SU(N)$. Of these $N - 1$ may be chosen to be diagonal. In other words $N - 1$ generators of $SU(N)$ commute.

Another representation of the Lie algebra of $SU(N)$, called the *adjoint representation* may be constructed directly from the structure coefficients.

We define $d(= N^2 - 1)$ $d \times d$ matrices θ_i by defining:

$$(\theta_a)_{bc} = -if_{abc} \quad (\text{A.12})$$

These matrices may be shown to fulfill the relation of the Lie algebra:

$$[\theta_a, \theta_b] = if_{abc}\theta_c \quad (\text{A.13})$$

A.4 $SU(3)$

Turning specifically to $SU(3)$, we note that we have $3^2 - 1 = 8$ generators of the fundamental representation. Two of these can be diagonal.

Using the so-called *Gell-Mann notation*, we may define:

$$\begin{aligned} \lambda_1 &= \begin{pmatrix} 0 & 1 & 0 \\ 1 & 0 & 0 \\ 0 & 0 & 0 \end{pmatrix} & \lambda_2 &= \begin{pmatrix} 0 & -i & 0 \\ -i & 0 & 0 \\ 0 & 0 & 0 \end{pmatrix} & \lambda_3 &= \begin{pmatrix} 1 & 0 & 0 \\ 0 & -1 & 0 \\ 0 & 0 & 0 \end{pmatrix} \\ \lambda_4 &= \begin{pmatrix} 0 & 0 & 1 \\ 0 & 0 & 0 \\ 1 & 0 & 0 \end{pmatrix} & \lambda_5 &= \begin{pmatrix} 0 & 0 & -i \\ 0 & 0 & 0 \\ i & 0 & 0 \end{pmatrix} & \lambda_6 &= \begin{pmatrix} 0 & 0 & 0 \\ 0 & 0 & 1 \\ 0 & 1 & 0 \end{pmatrix} \\ \lambda_7 &= \begin{pmatrix} 0 & 0 & 0 \\ 0 & 0 & -i \\ 0 & i & 0 \end{pmatrix} & \lambda_8 &= \frac{1}{\sqrt{3}} \begin{pmatrix} 1 & 0 & 0 \\ 0 & 1 & 0 \\ 0 & 0 & -2 \end{pmatrix} \end{aligned} \quad (\text{A.14})$$

and find that the λ -matrices obey the relation:

$$\left[\frac{\lambda_a}{2}, \frac{\lambda_b}{2} \right] = if_{abc} \frac{\lambda_c}{2} \quad (\text{A.15})$$

This gives us $8^3 = 512$ structure coefficients of which most are zero. The remaining ones are written out as:

$$f_{123} = 1 \tag{A.16}$$

$$f_{458} = f_{678} = \frac{\sqrt{3}}{2} \tag{A.17}$$

$$f_{147} = -f_{156} = f_{246} = f_{257} = f_{345} = -f_{367} = \frac{1}{2} \tag{A.18}$$